Leveraging Polarization in the Era of Submillimeter VLBI

by

Chunchong Ni

A thesis
presented to the University of Waterloo
in fulfillment of the
thesis requirement for the degree of
Doctor of Philosophy
in
Physics

Waterloo, Ontario, Canada, 2024

Examining Committee Membership

The following served on the Examining Committee for this thesis. The decision of the Examining Committee is by majority vote.

External Examiner:	Maxim Lyutikov Professor, Dept. of Physics and Astronomy, Purdue University
Supervisor:	Avery Broderick Associate Professor, Dept. of Physics and Astronomy, University of Waterloo; Research Associate Faculty, Perimeter Institute for Theoretical Physics
Internal Member:	Niayesh Afshordi Professor, Dept. of Physics and Astronomy, University of Waterloo; Research Associate Faculty, Perimeter Institute for Theoretical Physics
Internal Member:	Kendrick Smith The Daniel Family James Peebles Chair in Theoretical Physics, Perimeter Institute for Theoretical Physics
Internal-External Member:	Achim Kempf Professor and Canada Research Chair in the Physics of Information, Dept. of Applied Mathematics, University of Waterloo

Author's Declaration

This thesis consists of material all of which I authored or co-authored: see Statement of Contributions included in the thesis. This is a true copy of the thesis, including any required final revisions, as accepted by my examiners.

I understand that my thesis may be made electronically available to the public.

Statement of Contributions

This is primarily the combined result of one paper published and one paper in preparation:

- Chapter 2 is based on Ni, C., Broderick, A. E., Wielgus, M. & Janssen, M., et al. in prep., Structure and Polarization of Centaurus A on Milliarcsecond scales. A paper that is currently in preparation.
- Chapter 3 is based on Ni, C., Broderick, A. E. & Gold, R., 2022, Probing Accretion Turbulence in the Galactic Center with EHT Polarimetry, The Astrophysical Journal, 940, 149. http://10.3847/1538-4357/ac9b47

In addition, Vedant Dhruv and many others from the University of Illinois at Urbana-Champaign provided us with the GRMHD simulation in Section 3.4.1. Richard Qiu and Angelo Ricarte and many others provided us with the GRMHD simulation in Section 3.4.4. Maciek Wielgus calibrated all the EHT data used in Section 2.4 and Section 2.5, and Michael Janssen provided us with the synthetic data used in Section 2.4.2 and Section 2.5.1. Avery Broderick originally wrote the text in Section 2.6.4.

For these publications, I am the primary author, who analyze and write the majority of the work. Co-authors provided constructive suggestions and provided datasets and simulations.

Abstract

With the advancement of technology, global very long baseline interferometry (VLBI) observations at millimeter wavelengths become possible. The Event Horizon Telescope (EHT) is the first such experiment, which makes observing accretion disk and jet launching regions near supermassive black holes and active galactic nuclei (AGN) possible, including polarimetry observations.

Centaurus A (Cen A) is a nearby radio-loud AGN, with large jet structures of angular size measured in degrees. It was observed by the EHT, whose first total intensity image shows a fork-shaped edge brightening jet structure. Chapter 2 applies Bayesian imaging method to the Cen A data. We first construct the total intensity image of Cen A, which we directly compare with the previous publication. Second, the Bayesian method produces the first polarization studies of Cen A jet. Both the total intensity imaging and the polarization mapping feature a full image posteriors with access to the image uncertainty. This proves to be essential in the case of Cen A, where the data is very challenging for various reasons. With polarization image posterior of Cen A, we are able to study different regions of the jet separately, eventually producing a robust estimate of a collection of important physics quantities, including magnetic field strength, the electron number density and the jet velocity.

In Chapter 3, we explore the origin and influence of the interstellar scattering on observations of Sgr A*, and propose a novel method to mitigate this scattering via EHT and next-generation EHT (ngEHT) polarimetry in the future. In EHT and other radio astronomical observations of Sgr A*, scattering contaminates the image with external small-scale structures, essentially preventing further studies of the turbulence in the accretion disk. However, for credible interstellar magnetic field strengths, the scattering is proved to be insensitive to polarization. Therefore, it is possible to distinguish intrinsic and scattered structures via the image power spectra constructed in different polarization components. Via numerical experiments, we demonstrate a method for reconstructing intrinsic structural information from the scattered power spectrum. We demonstrate that this is feasible through a series of numerical experiments with general relativistic magnetohydrodynamic (GRMHD) simulation images. Specifically, we show that the ratio of the power spectra, obtained independently for different polarization components, is independent of the scattering screen. Therefore, these power spectra ratios provide a window directly into the MHD turbulence believed to drive accretion onto black holes.

Acknowledgments

I would like to thank all the people who have supported me throughout the PhD journey. Without them, this thesis would not be possible. Among many, Avery Broderick, my supervisor, deserves the highest praise, who has guided me through the highs and lows during the Ph.D. Always enthusiastic about science and always understanding towards me, Avery has inspired me not only to be a scientist but also to be a better human.

I would also like to thank my fellow Ph.D students postdocs, especially Boris Georgiev, with whom I almost shared my entire Ph.D. Boris is always willing to provide help with other people's projects, including mine. I would also like to thank Britton Jeter, Paul Tiede, Roman Gold and Hung-Yi Pu. Together we survived the daily doubles to make the first image of black hole possible.

Also, I value the help and friendship from the Event Horizon Telescope Collaboration. Making images of black holes together will be a great memory in my life.

Finally, a deepest gratitude towards Yiyi Liu, and Charlie. Your support is what drives me forwards.

Dedication

Dedicated to the important people in my life, my father, mother, and Yiyi, who have supported me throughout my PhD journey.

Table of Contents

List of Figures

List of Tables

Chapter 1

Introduction

1.1 Black hole and AGNs

1.1.1 Black holes

Black holes are cosmic objects with gravitational fields so intense that nothing, not even light, can escape once it crosses the boundary surrounding a black hole. This boundary, the event horizon, is the most prominent feature that distinguishes itself from other celestial objects, inside which the escape velocity is larger than the speed of light.

The first solution to the Einstein equation (Einstein, 1916) is the Schwarzschild metric, which describes the spacetime about a non-rotational black hole:

$$ds^2 = -\left(1 - \frac{r_s}{r}\right) c^2 dt^2 + \left(1 - \frac{r_s}{r}\right)^{-1} dr^2 + r^2 \left(d\theta^2 + \sin^2\theta d\phi^2\right), \tag{1.1}$$

where c is the speed of light, G is the gravitational constant, M is the black hole mass, r, θ and ϕ are the coordinates in the spherical coordinate system. This spacetime has a event horizon, a surface which event light cannot escape from. This surface has a radius, r_s, known as the Schwarzschild radius,

$$r_s = \frac{2GM}{c^2}. \tag{1.2}$$

Characterized by their masses, there are different types of black holes, which range from stellar mass black holes to intermediate black holes to supermassive black holes [1]:

[1] There is another type of hypothetical black holes: primordial black holes, which is theorized to exist

- Stellar mass black holes form from the gravitational collapse of massive stars at the end of their life cycles. Their masses can range from about 5 to several tens of solar masses. Observations of such black holes and the remnants of their progenitor stars have been reported in numerous studies (Burrows & Vartanyan, 2021, and reference therein).

- Intermediate black holes have masses in the range of hundreds to thousands of solar masses. Evidence for their existence is still largely circumstantial (Miller & Colbert, 2004). However, recent observations from gravitation wave detection may have found evidence for intermediate-mass black hole mergers (Abbott et al., 2020).

- Supermassive Black Holes are found at the centers of most large galaxies, including the Milky Way. Supermassive black holes have masses ranging from millions to billions of solar masses. Their existence has been inferred from the motion of stars and gas in the galactic centers and from the enormous energy output of active galactic nuclei, which are believed to be powered by accretion of matter onto supermassive black holes (Ghez et al., 2008; Kormendy & Richstone, 1995). Recent direct observations from the Event Horizon Telescope (EHT) Collaboration have confirmed the existence of supermassive black holes at the center of M87 and the Milky Way by showing the shadow of the black hole against the backdrop of the glowing gas in the accretion disk (Event Horizon Telescope Collaboration et al., 2019a, 2022a).

In addition to mass, black holes can have angular momentum and electric charge ,as a consequence of the no hair theorem (Israel, 1967). Charge is not astrophysically relevant due to the wide availability of free charges that will neutralize objects with sufficient charge to have a gravitational impact. Angular momentum, however, is critical, and the metric for a spinning black hole, known as the Kerr metric (Kerr, 1963), is given by

$$ds^2 = -\left(1 - \frac{r_s r}{\rho^2}\right) dt^2 - \frac{2 r_s r a \sin^2\theta}{\rho^2} dt d\phi + \frac{\rho^2}{\Delta} dr^2 + \rho^2 d\theta^2 + \left(r^2 + a^2 + \frac{r_s r a^2 \sin^2\theta}{\rho^2}\right) \sin^2\theta d\phi^2, \tag{1.3}$$

where t, r, θ and ϕ are the coordinates in the Boyer-Lindquist coordinate system, r_s is the aforementioned Schwarzschild radius, M is the black hole mass, J is total angular momentum, $a = J/M$, $\rho = r^2 + a^2 \cos^2\theta$ and $\Delta = r^2 - 2Mr + a^2$.

The spin of a black hole, characterized as $a_* = cJ/GM^2$, plays a important role in the a collection of astrophysical observations in the vicinity of black holes, particularly in

at early universe from the fluctuation of the dense mass field. Primordial black holes are proposed to be candidates of dark matter (Carr et al., 2021, 2024). However, they are intrinsically different from the astrophysical black holes that are of relevance to this dissertation.

the context of polarizations in the vicinity of black holes. The rotation of a black hole not only influences the innermost stable circular orbits of particles in its vicinity but also significantly impacts the accretion processes within the surrounding accretion disk. This process can lead to the emission of jets and the twisting of magnetic fields, phenomena that are deeply intertwined with the observed polarizations of light. Polarimetric observations, therefore, offer a window into the physics of these extreme environments, where the interplay between the black hole's spin, magnetic fields, and relativistic particles results in distinctive polarization signatures. These signatures provide crucial insights into the orientation, composition, and dynamics of the black hole and its accretion disk, making polarization studies a powerful tool in the astrophysical exploration of black holes and their cosmic environments (see, e.g., Piran & Stark, 1986; Broderick & Blandford, 2004; Agol, 1997; Palumbo et al., 2020).

1.1.2 Active Galactic Nuclei

Active Galactic Nuclei (AGN) are the extremely luminous central regions of some galaxies, whose energy output from AGN can outshine the combined stellar light of the host galaxy, making them some of the brightest objects in the universe. They feature some but not necessarily all of the following properties (Mo et al., 2010):

- high luminosity in the compact nuclei region;
- non-thermal continuum emission;
- strong emission lines;
- variable continuum emission.

AGNs are classified into different connected to their listed observational properties, some subgroup of which may overlap depending on the features of the specific AGN. There are different main types of AGNs: Seyfert galaxies, radio galaxies, quasars and blazars.

Seyfert galaxies, discovered in Seyfert (1943), are typically spiral galaxies with bright, point-like nuclei that show strong emission lines. They are further divided into: Type 1 Seyfert and Type 2 Seyfert, depending on the properties of their emission lines.

Quasars are the most luminous and distant types of AGN, characterized by their point-like appearance in optical telescopes, and high variability within one day. Quasars and Seyfert 1 galaxies share may similar features, including similar emission line properties.

They differ as quasars have much higher luminosities and are typically far away from the Earth. However, it is worth noting that distinction among different AGN classification may be blur, depending on their observational features.

Blazars, including BL Lacertae objects and Optically Violent Variables (OVVs), are a subgroup that are characterized by rapid variability, strong polarization, as a result of their relativistic jets pointed almost directly toward the Earth.

Radio galaxies are AGN that are radio-loud. They are first identified in Edge et al. (e.g., 1959). In principle, radio galaxies can usually be identified as Seyfert 1 and Seyfert 2 galaxies, depending on their emission lines. They usually feature jets and lobes extending well beyond the host galaxy. Radio galaxies are often further divided by (Fanaroff & Riley, 1974) depending on their viewing angles: Fanaroff-Riley Class I (FR I), whose radio sources with jets grow brighter at increasing distances from the central galaxy, and Fanaroff-Riley Class II (FR II), which is characterized by bright hot spots at the outer edges of their radio lobes, with the regions near the galaxy being less bright. However, recent studies have complicated this categorization even further, in the sense that substantial galaxies with morphologies in between FR I and FR II have been found (Mingo et al., 2019).

There have been attempts to unify all the AGN models (Urry, 2003). The classification of AGN, as mentioned above, is largely empirical and overlaps with one another. The unified model of AGN posits that many of the differences observed among various types of AGN are primarily due to the observational features rather than intrinsic differences: the orientation of the AGN relative to our line of sight and the presence of a jet. The presence of a dusty torus surrounding the accretion disk and black hole can obscure our view, leading to the classification of AGN into different types based on the observed features. AGN are known also for their variability across the electromagnetic spectrum, a characteristic that is influenced by the dynamic processes near the event horizon of the supermassive black hole. Variations in the accretion rate, disk instabilities, and changes in the orientation or structure of the dusty torus can all contribute to the observed variability.

AGNs are natural laboratories for studying high-energy astrophysical processes, including accretion physics and the formation of relativistic jets (Blandford & Znajek, 1977; Blandford & Payne, 1982). Additionally, AGNs also play a crucial role in the study of galaxy formation and evolution. The interaction between AGN and their host galaxies, known as AGN feedback, in the form of energetic winds and jets, can regulate star formation in the host galaxy (e.g. McNamara & Nulsen, 2012; Fabian, 2012), which the hot gas is heated and channeled outwards by the jet. The energy and material ejected by AGN can regulate star formation in the host galaxy by heating and dispersing the interstellar medium. This feedback mechanism is crucial in theoretical models to explain the observed

properties of galaxies and the co-evolution of galaxies and their supermassive black holes.

There are several different components of a typical AGN: the accretion disk, the jet (although not all of the AGNs have jet, including Sagittarius A*), and the dusty torus. The accretion disk consists of gas and dust spiraling into the supermassive black hole, caused by magnetohydrodynamic instability which transports angular momentum. There are a multiple ways to heat the disk, for example, viscous dissipation, magnetic reconnection and gravitational heating etc., causing it to emit radiation across the electromagnetic spectrum, from radio to X-rays (Shakura & Sunyaev, 1973).

Jets in AGN consist of relativistic particles ejected perpendicular to the accretion disk. These jets can extend well beyond the galaxy, emitting strong radio waves (Bridle & Perley, 1984). One of the leading theories explaining the formation of the jet is Blandford-Znajek process (Blandford & Znajek, 1977), in which the power is transferred by magnetic fields.

The dusty torus surrounding the accretion disk is a doughnut-shaped region of dust that can obscure the AGN when viewed from certain angles. The torus is responsible for the anisotropic emission of AGN, leading to different classifications based on the viewing angle.

1.1.3 Relationship between Black Holes and AGN

The relationship between AGN and supermassive black holes is a complex and dynamic relationship that encompasses the processes of accretion, energy conversion, jet formation and feedback mechanisms. This interplay is crucial for understanding not only the physical characteristics of AGN and black holes but also their significant impact on galaxy formation and evolution. The study of this relationship is central to many areas of astrophysics and provides key insights into the fundamental processes governing the universe.

To explain the high luminosity of AGNs, the leading theory believe that the supermassive black hole (SMBH) at the center of an AGN is the "central engine" driving the AGN's luminosity (see, e.g., Rees, 1984; Lynden-Bell, 1969). The evidence that AGNs house SMBHs is supported by many pieces of observational evidence, from the direct imaging of the vicinity of supermassive black holes (such as the Event Horizon Telescope's image of the black hole in M87 and the Milky Way (Event Horizon Telescope Collaboration et al., 2022a, 2019a)) to indirect observations such as the measurement of stellar velocities near galactic centers, which infer the presence of a massive central object (Ghez et al., 2008; Boehle et al., 2016).

The extreme luminosity of an AGN will suppress further accretion, leading to a characteristic luminosity limit, the Eddington luminosity. This limit may be calculated by

balancing the radiation pressure and the self-gravity of the gas, assuming spherical accretion (non-spherical accretion can achieve super-Eddington luminosity):

$$L_{Edd} = \frac{4\pi G c m_p}{\sigma_T}, \tag{1.4}$$

where m_p is the proton mas and σ_T is the Thompson scattering cross section.

If one believes that this luminosity is solely powered by the gravitational energy released by accretion, then the mass accretion rate corresponding to the luminosity is

$$\dot{M_{Edd}} = \frac{L_{Edd}}{\epsilon c^2}, \tag{1.5}$$

where ϵ is the accretion efficiency. Usually up to 10% of the accreted mass is converted into radiation. For AGNs with high luminosity, their luminosity can reach 1% of their Eddington luminosity limits. For low-luminosity AGNs, the ratio between their luminosity and Eddington limits can be orders of magnitude lower. For example, the two main targets of the EHT, M87* and Sgr A*, are both low-luminosity AGNs, with their luminosity being $3.6 \times 10^{-6} L_{Edd}$ and $10^{-9} L_{Edd}$, respectively. The inefficient accretion causes that much of the accreted energy is advected into the black hole or carried away by outflows and jets rather than being radiated away (Narayan & Yi, 1994; Blandford & Begelman, 1999). This inevitably causes the heating of the accretion disk, making the accretion disk thick and opaque and prompting the formation of the jet. This model is called radiatively inefficient accretion flow (RIAF), and the observed properties of Sgr A* has been very well explained by this model (see, e.g. Yuan et al., 2003; Broderick & Loeb, 2009a; Broderick et al., 2011).

In the accretion flow near SMBHs, material, such as interstellar gas and dust, loses angular momentum, causing them to spiral inward, before reaching a highly ionized state to form a plasma-rich accretion disk around the black hole. It's worth noting that, particularly in regions like the Galactic Center, the accretion might be primarily fed by winds from specific types of stars, such as Wolf-Rayet stars, rather than a interstellar gas and dust. The process of angular momentum transport, crucial for the inward spiral of matter, is complex and there are many mechanisms that can facilitate the process. For example, the differential rotation of the disk, where the inner parts rotate faster than the outer parts, leading to viscous shear between adjacent layers of the disk material, through which force angular momentum is transferred from the faster-moving inner layers to the slower-moving outer layers. Magnetic fields also plays an important role. Magnetorotational instability (MRI) is a key mechanism in angular momentum transport within accretion disks (Balbus & Hawley, 1991, 1998). MRI arises in disks that are weakly magnetized and exhibit differential rotation, and destabilizes the disk, leading to magnetohydradynamic

(MHD) turbulence. This turbulence effectively increases the viscosity within the disk, enhancing the transfer of angular momentum outward and allowing mass to spiral inward. Only very weak magnetic fields are needed to initialize the MRI, and it efficiently grows the magnetic field strength, facilitating even more effective angular momentum transport. However, it's crucial to understand that this description, particularly the formation of a plasma disk, may not universally apply to all types of accretion flows. In some efficient accretion systems, cooling mechanisms could maintain a cooler disk state, diverging from the highly ionized, plasma-rich disk model, like the systems of Sgr A* and M87.

In some AGNs, a significant portion of energy is emitted in the form of relativistic jets. These jets, aligned perpendicularly to the accretion disk, can extend well beyond the host galaxy. The exact mechanism behind jet formation is still uncertain, with magnetic fields in the accretion disk (Blandford & Payne, 1982) and/or the black hole's spin (Blandford & Znajek, 1977) being crucial factors. The manner by which black holes accrete matter and launch jets is far from incidental, but rather plays a significant role in regulating the star formation of its host AGN, essentially plays the role of "engine" of the universe. This regulation happens through the aforementioned feedback mechanism, where the radiation and outflows from AGN can heat and disperse the interstellar medium, impacting star formation rates within the galaxy. This self-regulating mechanism helps to explain the observed correlation between black hole mass and galaxy properties, such as the bulge mass and stellar velocity dispersion (Silk & Rees, 1998; Fabian, 2012; McNamara & Nulsen, 2012).

1.2 Very Long Baseline Interferometry

1.2.1 Introduction to VLBI

Interferometry involves combining the signals received at multiple telescopes to simulate a telescope with a size equal to the separation between the telescopes. The projected 2D separation between stations is known as the baseline. Long baselines would be able to resolve small structures, while short baselines captures the entire flux of the target source. At its core, interferometry achieves high angular resolution by extracting information from the electromagnetic wave interference pattern.

The development of Very Long Baseline Interferometry (VLBI), which utilizes telescopes at different locations scattered across the globe, The stations are sufficiently distant and the atmosphere is uncorrelated at two stations. The introduction of intercontinental baselines enable high angular resolution, surpassing that of individual telescope and

of connected-element interferometry by orders of magnitude. This allows astronomers to study fine details in the structure and motion of cosmic objects, such as the jets of AGN and the event horizon of supermassive black holes.

Fundamentally, VLBI becomes possible by recording the electric field at each telescope, which requires a high-accuracy local oscillator (e.g., hydrogen masers) to time-tag and record signals at each station, which preserves the coherence information long enough to make measurement of interferometry fringes. This recorded signal then is converted to lower intermediate frequency to be recorded on magnetic tapes. Finally, the taped signal is correlated at correlators. This underlying technique of VLBI was brought forward and discussed in the early 1960s (Matveenko et al., 1965) and summarized in Moran (1998).

In 1967, several groups developed and performed the first VLBI experiments independently. The very first experiment, by a group in University of Florida, detected interferometry fringes at 18MHz of Jupiter (Brown et al., 1968) with recording bandwidth $2kHz$. More complicated and more sensitive VLBI experiments were designed and performed later that year by other three groups on several quasars and masers, with much higher observational frequencies and recording bandwidth (Broten et al., 1967; Bare et al., 1967; Moran et al., 1967). The early experiments were able to achieve high angular resolution albeit the constraints set by the number of baselines available. However, early VLBI observations faced significant technical hurdles, including the synchronization of time and frequency standards between widely separated antennas and the recording and correlation of vast amounts of data.

Following these early experiments, VLBI saw a rapid expansion in VLBI capabilities, with international collaborations extending baselines to intercontinental distances. This era witnessed the establishment of dedicated VLBI networks, including the European VLBI Network (EVN) and the Very Long Baseline Array (VLBA) in the United States. In 2019, the Event Horizon Telescope Collaboration successfully captured the first image of a black hole's event horizon with VLBI. This global VLBI network, operating at unprecedented millimeter wavelengths, linked telescopes worldwide to observe the supermassive black hole in the galaxy M87*, showcasing the immense potential of VLBI for testing general relativity and studying extreme gravitational environments.

1.2.2 Technical Challenges and Solutions

VLBI operates by coordinating a global network of radio telescopes, effectively creating a continent-sized (e.g., MERLIN, EAVN) or planet-sized (e.g., EHT) interferometer. Some VLBI also includes a space station (e.g., VSOP/HALCA, Radio Astron) to further increase

the size of the aperture. This long baseline enables VLBI to achieve resolutions of the order of milliarcseconds or even microarcseconds for the EHT. For VLBI to work, the signals collected at each telescope must be precisely time-stamped using atomic clocks. This allows the data to be synchronized and combined accurately, preserving the phase information essential for constructing high-resolution images.

The nature of simultaneous observation at different locations require more sophisticated processing and calibration for the VLBI data, which includes atmospheric absorption and delay, instrumental effects, etc. Hence, advanced algorithms and computational resources are employed to reconstruct images from the collected data. Ongoing technological advancements, such as improved receiver sensitivity, faster data recording rates, and enhanced digital processing capabilities, continue to push the boundaries of VLBI's capabilities.

1.2.3 Applications in Studying Black Holes and AGN

VLBI is able to produce high-resolution images of AGN and black hole Surroundings. The prominent case is the EHT collaboration, which forms a synthesized global aperture by linking different telescopes in different locations at unprecedented shorted wavelength to date in VLBI ($1.3mm$) to achieve the highest resolution. By forming an aperture with size of the Earth, the EHT is able to achieve resolution up to 15 microarcseconds, which enables the direct observations of the resolved horizon of subjects as compact as the supermassive black holes in the center of the galaxy M87 and the Milky Way.

Prior to the EHT, several global VLBI experiments were performed on M87 since 2009 (see the summary and the references therein Wielgus et al., 2020). Those observations, although lack enough baselines, provided path-finding experience to the 2017 observations of the EHT. In 2017, the first observational campaign of the EHT was performed with eight telescopes in six locations: Atacama Large Millimeter/submillimeter Array (ALMA), Atacama Pathfinder Experiment (APEX), both in Chile, James Clerk Maxwell Telescope (JCMT), Submillimeter Array (SMA), both in Hawaii, Large Millimeter Telescope Alfonso Serrano (LMT) in Mexico, the Institut de Radioastronomie Millimétrique (IRAM) 30m telescope in Spain, South Pole Telescope (SPT) at the South Pole and Submillimeter Telescope (SMT) in Arizona, among which ALMA and SMA are arrays themselves, having 37 and 8 dishes each respectively. Each participating EHT telescope is equipped with an extremely precise hydrogen maser atomic clock. These clocks ensure that the observations made by all the telescopes are synchronized to within a fraction of a billionth of a second, which is crucial for the successful correlation of the data in VLBI

Due to the vast amount of data generated during observations and the limitations of real-time data transmission over long distances, the EHT records the data onto high-capacity hard drives. These drives are then physically transported to central processing facilities at MIT Haystack Observatory in Westford, Massachusetts, USA, and Max-Planck-Institut für Radioastronomie (MPIfR) in Bonn, Germany, where the data from all telescopes is correlated using specialized VLBI software (Deller et al., 2011), running on clusters of more than 1000 compute cores at each correlation site.

What is even more unprecedented for the EHT is the wavelengths at which it observes. The EHT operates at sub-millimeter wavelengths (specifically at 1.3 mm). The reasons behind the choice of this wavelength are manifold, including astrophysical, technical and atmospheric considerations.

First, the high frequency enables the high resolution, which is essential for imaging the small angular size of black hole event horizons from Earth. The resolution of a telescope is directly proportional to the wavelength it observes at,

$$R = \frac{\lambda}{D}, \tag{1.6}$$

where λ is the wavelengths and D is the size of the aperture.

Second, the optical depth due to synchrotron emission in the accretion disk makes the emission near the event horizon of Sgr A* and M87 decrease as we go to higher observational frequencies. 230 GHz is sufficiently high enough to penetrate the plasma to observe accretion from close enough to Sgr A*.

Third, the Earth's atmosphere is opaque to many wavelengths of electromagnetic radiation due to absorption by water vapor and other gases. However, there are specific "windows" where the atmosphere is relatively transparent, including 230GHz, 345GHz and 690GHz etc. The EHT opts for the 230GHz because at 230GHz many telescopes can participate. Interferometry becomes more and more difficult as the frequency is high. As a result, at 345GHz, only a fraction of the EHT telescopes can participate, while at 690GHz, even fewer telescopes would be able to observe. The next window is the near-infrared at which the interferometry must be done in the optical path. Observing at 230GHz allows ground-based telescopes to observe with reduced atmospheric interference. It should be noted that the air needs to be extremely dry, as absorption is primarily due to water vapors. This is why EHT sites are at high altitude or in dry locations like deserts, such as Atacama desert and Antarctica.

Lastly, specifically for Sgr A*, as Sgr A* lives within the Milky Way, observing it would require to see through the interstellar electrons, which would cause scattering. This interstellar scattering blurs and introduces small-scale structures to the observation of Sgr A*.

At lower frequencies observations (for example, 86 GHz and lower), scattering effect would dominate the observation of Sgr A*. However, this phenomenon is frequency dependent. Observing at high enough frequency, for example, 230 GHz, subdues the scattering, making horizon-scale information accessible (Event Horizon Telescope Collaboration et al., 2022b).

However, the choice of high frequency poses significant technical challenges due to the requirement of synchronization among the telescopes. Advanced techniques in signal processing, error correction, and image reconstruction are employed to overcome these challenges.

EHT has so far yielded many groundbreaking new discoveries The results include but not limit to the first images of the two supermassive black holes in the centers of the Galaxy M87 and the Milky Way, the first linear polarization mapping of horizon-scale structure near the vicinity of M87* and Sgr A*, high-resolution images and linear polarization mappings of several AGNs. The EHT's observation of the shadow and the photon ring of the supermassive black holes has contributes to understanding and constraining the mass and spin of black holes. These results also have allowed the study of the structure of accretion disks and the formation and evolution of relativistic jets emanating from the vicinity of supermassive black holes in AGN.

1.3 Polarization

1.3.1 Fundamentals of Polarization in Astrophysics

Polarization refers to the orientation of the electric field vector of electromagnetic waves. In astrophysics, light or other forms of electromagnetic radiation from cosmic sources can be intrinsically polarized or become polarized by a variety of physically processes (e.g., observations including Wardle & Kronberg, 1974; Homan & Lister, 2006). More specifically, the complex environments of AGN and the extreme gravitational fields of black holes can significantly affect the polarization state of emitted or scattered light, revealing the geometry and orientation of accretion disks, the properties of jets, and the influence of strong magnetic fields (e.g., see Broderick & Loeb, 2009b; Lyutikov et al., 2005; Gabuzda et al., 2004). Thus, polarization in the vicinity of AGN and black holes offers unique insights into the magnetic field structures, accretion processes, and relativistic jets associated with these objects.

The primary types of polarization include linear and circular, each characterized by the pattern of the electric field's oscillation. The general polarization, elliptical polarization,

is a combination of linear and circular polarization and can arise in various astrophysical processes. Linear polarization, where the electric field oscillates in a plane, is the most commonly observed type in astrophysical contexts, which often arises from synchrotron radiation in jets for AGN and in the accretion flow for black holes (Jones & O'Dell, 1977), as well as scattering processes in the accretion disk and broad-line region (Antonucci, 1993). Circular polarization happens when the electric field rotates around the direction of propagation, which may result from some polarization transfer effects in the magnetized plasmas (Burn, 1966). Observations of circular polarization, though challenging, can provide additional constraints on the magnetic field strength and topology in the vicinity of black holes and AGN jets.(Zavala & Taylor, 2003; Enßlin & Vogt, 2003).

There are a few different ways to cause polarization astrophysically, among which more relevant to this dissertation are through synchrotron radiation. Here are a few main mechanisms to generate polarization:

Thomson scattering, a classical electrodynamics phenomenon, is instrumental in inducing polarization in astrophysical contexts. When electromagnetic waves scatter off free electrons, the polarization state of the incident light can be altered, a process crucial for interpreting observations of the cosmic microwave background and the interstellar medium(e.g., see Rybicki & Lightman, 1986), as well as the polarization of X-ray binaries (Krawczynski et al., 2022). The high energy regime of Thomson scattering, known as inverse Compton scattering, where photons increase energy upon colliding with high-energy charged particles, can also create polarization. This phenomenon is particularly relevant in environments with strong magnetic fields and relativistic electrons, such as around pulsars and within AGN jets. The resulting polarization changes offer critical clues to the underlying magnetic and particle acceleration processes (e.g., see Blumenthal & Gould, 1970).

Synchrotron radiation is another significant polarization mechanism in AGN and around black holes, which is emitted by charged particles (usually electrons) gyrating at relativistic speeds around magnetic field lines. Many galactic radio emission is due to synchrotron, including accretion disk, jets, pulsars, supernova and supernova remnants, etc (Yuan & Narayan, 2014). Polarization measurements have been instrumental in mapping magnetic fields and understanding particle acceleration mechanisms in these extreme environments (see, e.g., Event Horizon Telescope Collaboration et al. (2021a,b) for black holes, Lyutikov et al. (2019) for pulsars, Lyutikov et al. (2005); Hovatta et al. (2019) for AGN jets).

There are other ways to generate linear polarization astrophysically, but is not directly related to the contents of this thesis. Therefore, we are going to briefly mention some of the other mechanisms:

Spinning dust grains in astrophysical environments can induce polarization in the light that passes through or is emitted from such regions. As the dust grains rotation introduces electric dipole, the electric dipole interacts with the passing charged particles, especially ions. This phenomenon would introduce extra polarization when there is alignment of the rotation and the magnetic field (Draine & Lazarian, 1998).

Zeeman and Goldreich-Kylafis Effects are another mechanism to generate polarization. Zeeman Effect involves the splitting of spectral lines under the influence of a magnetic field. The Zeeman effect in the presence of a strong magnetic field can lead to circular polarization in the spectral lines, providing direct measurements of the magnetic field strength in astrophysical objects. Goldreich-Kylafis Effect occurs in molecular clouds and regions of star formation, where non-spherical collisions in the presence of a magnetic field can induce linear polarization in molecular line emissions, offering insights into the magnetic field geometry in these regions (Goldreich & Kylafis, 1981).

Astrophysically, aside from mechanism of creating polarizations, transfer effects, which matters once polarization has been emitted, is also very important. Faraday rotation and conversion is such astrophysical mechanism that transfers polarization. Faraday rotation occurs when linearly polarized light passes through a magnetized plasma, causing the plane of polarization to rotate. This effect is due to the differential speed at which the left and right circular polarizations propagate through the plasma, influenced by the magnetic field. Faraday rotation is a powerful tool for probing magnetic fields in various environments, such as the interstellar medium, galaxies, and the vicinity of AGN. The degree of rotation provides information about the line-of-sight component of the magnetic field and the electron density of the intervening medium (Gardner & Whiteoak, 1966; Brentjens & de Bruyn, 2005). Usually, Faraday rotation is measured with multi-frequency observation, as Faraday rotation's effect on the plane of polarization of light is wavelength-dependent, with the rotation angle being proportional to the square of the wavelength:

$$\psi = RM\lambda^2, \tag{1.7}$$

where RM is the rotation measure, defined as:

$$RM = \frac{e^3}{2\pi m^2 c^4} \int n_e(s) B(s) ds, \tag{1.8}$$

where e is the electron charge, m is the electron mass, n_e is the electron number density, and $B(s)$ is the line-of-sight magnetic field strength Burn (1966). Recent studies of Faraday rotation in radio astronomy including probing magnetic fields in AGN jets are aplenty(Zavala & Taylor, 2002, 2003; Lyutikov et al., 2005; Homan & Lister, 2006; Broderick & Loeb, 2009b; Park et al., 2019; Goddi et al., 2021, see, e.g.,)

1.3.2 Stokes Parameters and Polarization

Stokes parameters offer a comprehensive framework for describing the polarization state of electromagnetic radiation, encapsulating information about the intensity and polarization direction of light waves. These parameters (I, Q, U, and V) represent a set of values that can fully characterize the polarization properties of light:

- I: the total intensity of the light. This parameter represents the sum of the intensities of two orthogonal components of the electric field vector. Mathematically, if E_x and E_y are the electric field amplitudes in two orthogonal directions (e.g., x and y), then $I = \langle E_x^2 \rangle + \langle E_y^2 \rangle$, where the angle brackets denote time averaging.
- Q: the difference in intensity between two orthogonal linear polarization components. If we consider the same orthogonal components as above, $Q = \langle E_x^2 \rangle - \langle E_y^2 \rangle$. A positive Q implies that the light is more polarized along the x-axis, while a negative Q indicates stronger polarization along the y-axis.
- U: The intensity difference between two linear polarization components at 45° to the x and y axes. If E_{45} and E_{-45} are the electric field amplitudes at $+45°$ and $-45°$ to the x-axis, then $U = \langle E_{45}^2 \rangle - \langle E_{-45}^2 \rangle$.
- V: the difference in intensity between right-handed and left-handed circularly polarized light. It describes the circular polarization of the wave, with positive V indicating right-handed circular polarization and negative V suggesting left-handed circular polarization.

In the context of astrophysical observations, Stokes parameters are crucial for extracting quantified information about the polarization state of light from celestial sources, offering insights into the physical conditions and magnetic fields in the regions where the light was emitted or interacted with matter.

1.3.3 Polarization Studies in AGN and Black Hole Environments

Polarization studies in astrophysics offer a unique window into the physical conditions and processes in the environments of AGN and black holes. By analyzing the polarization of light and other forms of electromagnetic radiation, astronomers can infer the properties of magnetic fields, probe the dynamics of jets and accretion disks, and test fundamental physical theories in some of the universe's most extreme environments.

As mentioned in the previous subsection, synchrotron radiation is the primary mechanism to generate polarization in the AGNs and around black holes, which is often associated with the jets ejected from the nucleus and the accretion disk near the black holes.

Observations of polarization allow researchers to probe the magnetic field structures and dynamics within the vicinity of these massive objects, offering insights into the magnetic fields influenced by extreme gravitational forces. For instance, polarization measurements is crucial in mapping the magnetic fields in jets emanating from supermassive black holes, which are significantly impacted by the strong gravitational pull of the black hole itself (Broderick & Loeb, 2009a; Johnson et al., 2015a; Doeleman et al., 2008). The linear polarization angle can provide insights into the magnetic field structure, and the polarization fraction indicates the nature of the synchrotron emission region, including the energy distribution of electrons in the jet . Recent studies highlight the role of polarization in mapping out the magnetic fields within AGN jets and accretion disks, contributing to our understanding of jet collimation and stability, as well as accretion hydrodynamics (e.g.,see Lyutikov et al., 2005; Broderick & Loeb, 2009b; Issaoun et al., 2021; Ni et al., 2022). Moreover, the extreme gravitational fields can also affect the polarization of light. The gravitational lensing near the event horizon can alter the observed polarization patterns. Studying these effects can test theories of gravity and provide insights into the physics of black hole event horizons (Palumbo et al., 2020; Event Horizon Telescope Collaboration et al., 2021a,b).

Recent advancements in observational techniques and instruments have significantly improved our ability to measure and interpret astrophysical polarization. High-resolution radio and optical polarimetry, as well as emerging X-ray polarimetry missions, are pushing the boundaries of what we know about the magnetic fields, accretion processes, and relativistic jets in AGN and black hole environments.

High-resolution polarization studies, particularly in radio wavelengths, have revealed the intricate magnetic field structures within AGN cores and jets. For example, observations of the radio galaxy M87 with the EHT have provided unprecedented details on the polarization near the black hole's event horizon, shedding light on the magnetic fields that govern accretion and jet launch processes (Event Horizon Telescope Collaboration et al., 2021a,b). Other polarization studies of AGN include recent EHT observations of NRAO 530 and J1924-2914, where the linear polarization structures in the jets are resolved, providing insights into the magnetic fields inside the jet (Issaoun et al., 2022; Jorstad et al., 2023). There are other non-EHT studies of polarization in AGN. For example, in the quasar 3C 273, polarization measurements have traced the magnetic field alignment along the jet, indicating a helical magnetic field structure potentially responsible for jet collimation and stability (Asada et al., 2008).

These studies not only enhance our understanding of individual AGNs and black holes but also contribute to broader astrophysical theories, including the dynamics of galactic nuclei, the interplay between black holes and their host galaxies, and the fundamental physics of gravity and high-energy phenomena. By dissecting the polarization observed in these extreme environments, astronomers can peel back layers of complexity and gain insights into some of the most energetic and dynamic processes in the universe.

1.4 Thesis summary

In this thesis, we explore using polarization as a leverage to extract astrophysical information, for AGN and supermassive black holes, from the VLBI observation of the EHT. In Chapter 2 and Appendix A, we use a Bayesian-based imaging pipeline, THEMIS, to construct the total intensity and the first linear polarization map of Centaurus A, an AGN observed by EHT. Based on the images we have constructed, we analyze the physical properties Centaurus A, constraining the magnetic field and electron density in the jet, as well as the jet velocity and inclination angle. In Chapter 3 and Appendix B, we design a new scheme to extract information of turbulence in the accretion flow of Sgr A*, essentially mitigating interstellar scattering. The key idea of this scheme is to utilize polarization information and the non-birefringence feature for the scattering screen. Finally, in Chapter 4, we summarize the thesis.

These two projects together showcase the importance of polarization in the era of submillimeter VLBI observations. The utilization of polarimetry to see through the scattering screen is not only a novel way of scattering mitigation, but also a direct probe into the fine structure of the turbulence in the accretion disk. On the other hand, using Bayesian method to construct Centaurus A images is the first polarization result of the Centaurus A jet at such high resolution. Methodologically, we push our current Bayesian-based imaging method to the limit, to tackle with the challenging dataset with weak polarization signal. Astrophysically, the detection of polarization enables constraints of magnetic field strength and electron number density in the innermost part of the jet.

Finally, with the advancement of VLBI technology, VLBI observations with higher sensitivity and better telescope coverage will provide us with more high quality datasets. More observations of Sgr A*, together with better telescopes with high sensitivity, would push the resolution of turbulence structure further, regardless of interstellar scattering. It will help better understand the accretion mechanism, answering many unknown questions like plasma instabilities and angular momentum transport near the black hole. More telescopes at different locations, on the other hand, will be extremely helpful in increasing

the number of baselines, essentially providing more constraints on the image structures of VLBI target sources. More sensitive telescopes can also help with the detection of weak polarization signals, which would shed light in understanding of the jet and horizon-scale physics. Applying our methods to future VLBI data will be left for future works.

Chapter 2

Centaurus A

2.1 Introduction

Centaurus A (Cen A; also NGC 5128) is a prominent radio-loud galaxy located approximately 3.8 Mpc away (Harris et al., 2010). This galaxy hosts an active galactic nucleus, which houses a supermassive black hole (SMBH) with an estimated mass of 55 million solar masses (Cappellari et al., 2009). The SMBH powers an extensive extragalactic jet that is prominently visible across multiple wavelengths. This prominent jet has large scale structure of a few degrees, which distinguishes Cen A from other AGNs (Remazeilles et al., 2015). As one of the closest radio-loud galaxies to Earth, Cen A offers a critical opportunity to study AGN jets at high resolution.

Over the past half-century, Cen A has been observed across a wide range of frequencies, from 100 MHz to TeV (see, e.g., Müller et al., 2011; Feain et al., 2011; Hardcastle et al., 2003; Clarke et al., 1992). Observations in the radio spectrum have revealed a complex lobe structure that provides evidence of ongoing energetic particle acceleration processes and interactions with the interstellar medium (Feain et al., 2011). These structures are believed to be shaped by the dynamics of the jet and the external medium, influenced by the central AGN.

The detailed imaging and spectroscopy from the Chandra X-ray Observatory have further contributed to the understanding of the high-energy emissions from Cen A, illuminating the jet structure and its X-ray emitting knots, which correlate closely with radio features (Kraft et al., 2002). These observations underscore the multi-wavelength synergy necessary for a comprehensive understanding of such a complex AGN.

Polarization studies of Cen A have also provided important insights into the magnetic field configurations and particle acceleration mechanisms within its jets and lobes. Observations with the Australia Telescope Compact Array (ATCA) have been pivotal in detailing the magnetic field structure. For example, studies using ATCA have revealed that the magnetic fields in the lobes are aligned with the edges of the radio-emitting regions, suggesting that the fields are shaped by the dynamics of the jets and the surrounding medium (Feain et al., 2009). This alignment supports the theory that magnetic fields play a critical role in the collimation and maintenance of the jet structures in AGN. Moreover, the detection of polarized emissions in the inner lobes indicates complex magnetic field interactions at the site where the jet interacts with the interstellar medium (O'Sullivan et al., 2013).

Further high-resolution polarization measurements by the Very Large Array (VLA) have allowed astronomers to map the polarization at different frequencies, providing a multi-frequency polarization analysis that helps in understanding the spectral energy distribution and magnetic field dispersion along the jet (Burns et al., 1983; Clarke et al., 1992). These studies confirm that the degree of polarization decreases towards the core, which is echoed in Goddi et al. (2021) and this thesis.

However, due to its large negative declination, past very-long-baseline interferometry (VLBI) observations below 1cm have not observed Cen A until 2017 with the advent of the Event Horizon Telescope (EHT), which observed Cen A at $\lambda = 1.3$mm (Janssen et al., 2021). This milestone observation has provided unprecedented close-up views of the core and enabled detailed studies of the jet launching region near the SMBH.

Simultaneous with the EHT observations, Atacama Large Millimeter/submillimeter Array (ALMA) observed Cen A at $\lambda = 1.3$ mm and $\lambda = 3$ mm (Goddi et al., 2021). At both wavelengths, Cen A was reported to be bright (5.66 ± 0.57 Jy). However, its linear polarization (LP) was notably weak, below 0.1%. Given these low values, Goddi et al. (2021) did not report any electric field position angle (EVPA) for Cen A. Additionally, at millimeter wavelengths, Cen A has a flat spectrum, with a spectral index of -0.197 ± 0.038, indicative of optically thick emission.

With the EHT's nominal resolution of 20 μas, the EHT resolved Cen A down to ~ 200 gravitational radii, about 0.6 light days. The constructed image showed a collimated and edge-brightened jet/counter-jet pair. However, the EHT's observations of Cen A face significant challenges for two reasons. First, only seven EHT telescopes that could observe Cen A, resulting in extremely sparse $(u, v)-$coverage. Second, all but three of these EHT stations are located in the northern hemisphere; therefore, most EHT stations can only observe Cen A at very low elevation.

These data problems motivates the re-imaging of Cen A from the 2017 observation data

using recently developed Bayesian method (Broderick et al., 2020a). In comparison to the methods used in Janssen et al. (2021), THEMIS (Broderick et al., 2020b), the Bayesian method we use, is able to produce a full image posterior (see, e.g., Event Horizon Telescope Collaboration et al., 2019b, 2022c; Kim et al., 2020; Issaoun et al., 2022; Jorstad et al., 2023). The image posteriors encompass all the possible representations of the data, and enable a quantitative analysis of image features.

We reconstruct the full image posteriors for Cen A for both the total intensity and LP map, accounting for all the unique EHT data challenges, including the aforementioned (u, v)-coverage, the large-scale structures, and telescope site calibrations etc. We obtain quantitative estimates of the uncertainty in the brightness distribution, LP fraction and the EVPA. Therefore, we present an independent characterization of the robustness of image reconstructions and the first LP map reconstruction of Cen A on light-day scales. Based on the images posteriors from the Bayesian method, we are able to assess the jet inclination angle and jet velocity based on the jet-counterjet brightness distribution. Further, we adopt a phenomenological model to probe the allowed joint distribution of magnetic field strength and the electron number density in the Cen A jet.

The structure of the chapter is as follows. Section 2.2 discusses the processing of the data and the Bayesian pipeline we used to produce the total intensity and linear polarization of Cen A. In Section 2.4, we present the Bayesian reconstruction of the total intensity image of Cen A. Then, the first linear polarization analysis of Cen A is presented in Section 2.5. Last, we discuss the physics results inferred from the image posteriors. In Section 2.6, we first estimate the magnetic field strength and the electron density given a two-zone phenomenological model. Then we assess the possible inclination and velocity of the Cen A jet. Finally, we provide preliminary conclusion to this chapter in Section 2.7.

2.2 EHT 2017 Cen A data

2.2.1 Review of Cen A data

Cen A was observed on April 10, 2017 by the EHT. In total, seven telescopes/arrays at 5 different locations carried out the observation, including ALMA, Atacama Pathfinder Experiment (APEX), both in Chile, James Clerk Maxwell Telescope (JCMT), Submillimeter Array (SMA), both in Hawaii, Large Millimeter Telescope Alfonso Serrano (LMT) in Mexico, South Pole Telescope (SPT) at the South Pole and Submillimeter Telescope (SMT) in Arizona, among which ALMA and SMA are arrays themselves, having 37 and 8 dishes

each respectively. The Institut de Radioastronomie Millimétrique (IRAM) 30m telescope, which participated in the EHT observation of other targets, did not join the observation of Cen A, due to the low elevation of the target (Event Horizon Telescope Collaboration et al., 2019c). All telescopes observed in full polarization modes, except for JCMT which observed only in left-circular polarization on April 10, 2017. The observation was carried out at two frequency bands, 227.1 and 229.1 GHz, dubbed "low" and "high" band, with bandwidths of 2 GHz. The detailed instrument configuration and the summary of the observational campaign can be found in Event Horizon Telescope Collaboration et al. (2019c).

Subsequently, the recorded data are further processed in Janssen et al. (2021), where two pipelines, rPICARD based on the Common Astronomy Software Applications (CASA) (Janssen et al., 2019) and EHT-HOPS based on the Haystack Observatory Post-processing System (HOPS) packages (Blackburn et al., 2019), are used. Independently, the two pipelines perform the required necessary calibration including the auto-correlation normalization, feed angle rotation, fringe fitting, and bandpass calibration, and reduce the phase from atmospherical turbulences. The reduced data are in the format of UVFITS files, which can be streamlined by THEMIS.

For the calibration of the polarimetry data, which is not in Janssen et al. (2019), we network calibrate the data, remove JCMT data (because JCMT only measures the left-hand polarization on April 10, 2017) and rotate the ALMA feed properly (as ALMA observes in linear polarization while other telescopes observe in circular). Note that, for example, the polarimetry calibration of Sgr A* requires correction of telescope parametric leakages. Telescope leakages and its D-term corrections are the instrumental effect, which causes the detected polarization signal "leaks" from one polarization band to the other. In Event Horizon Telescope Collaboration et al. (2024a), the leakage calibration is done by applying the pre-calculated D-term values from Event Horizon Telescope Collaboration et al. (2021a) directly. However, THEMIS does not require extra input from other sources to calibrate leakage, which is part of the MCMC fitting to the data already. This part shall be discuss more thoroughly in Section 2.3.

2.2.2 Data Challenges

The challenges faced by the Cen A dataset are threefold. The first issue(s) is telescope station-related, and has been known and discussed in Janssen et al. (2021). These station-related issues include signal loss at SMA and APEX, pointing errors at LMT and SPT, and the low elevation obstacle at the end of the observation for SMT. These issues would cause large sweeps of telescope gains across different scans.

The second issue for Cen A is intrinsic to VLBI, which is the sparse (u, v)-coverage. Although all EHT targets face the same problem of sparse (u, v)-coverage, the way this issue presents itself highly depends on the morphology of the targets. For the two horizon-scale targets, Sgr A* and M87*, they are azimuthally symmetric, and for other AGN targets, the direction of their jets are usually from northwest to southeast, where there is ample (u, v)-coverage. However, for Cen A, the jet exhibits itself across the off-diagonal, from northeast to southwest. In Figure 2.1, we show the (u, v)-coverage for Cen A on April 10, 2017, in which there is a noticeable region at $5\text{G}\lambda$ in the NE-SW direction (the gray circles) where (u, v)-coverage is minimal, which corresponds to roughly 40μas. In other words, in the direction of Cen A jet, we have very little control of structure at 40μas scales. In comparison, the size of Cen A jet in the $(u, v)-$space, shown as the blue circle, further shows the impact of the (u, v) cavities on jet structures.

The third issue is intrinsic to Cen A itself, which is the sheer size of Cen A on the night sky. The radio emission from Cen A extends over many degrees, resulting in structure on the EHT-intrasite baselines (Remazeilles et al., 2015). Although, other EHT targets like M87 also have large-scale structures, Cen A is different in the sense that large jet structure shares similar features with region that EHT is targeting (with angular size of hundreds of μas), while for M87, the jet structure is fundamentally different from the ring that EHT observes at the horizon scale. This complicates the traditional understanding of "intrasite baselines" within EHT. In other words, structures on the baseline of ALMA-APEX and SMA-JCMT may resolve large scale structure that is exclusive to Cen A among all EHT targets. Further more, another complication may be introduced by the large scale structure is that data of the high and low bands may be discrepant. A more thorough examination on the impact of the intrasite baselines will be discussed in Section 2.6.3.

2.2.3 Data Pre-processing

The three aforementioned data issues have different "solutions" that would enable us to make total intensity and linear polarization images, or at least lessen the impacts on our results.

To address the first station-related issues, in Janssen et al. (2021), the authors corrected the data losses mainly by calculating the self-calibration telescope gain solutions, and then applied the gain solutions to maximize their likelihoods. In comparison, the Bayesian method, THEMIS, generates image posteriors that solve telescope gains for every step when optimizing the likelihood. Hence, the signal loss should be encapsulated in the gain solutions. On top of the gain solutions as part of our models, we introduce some further

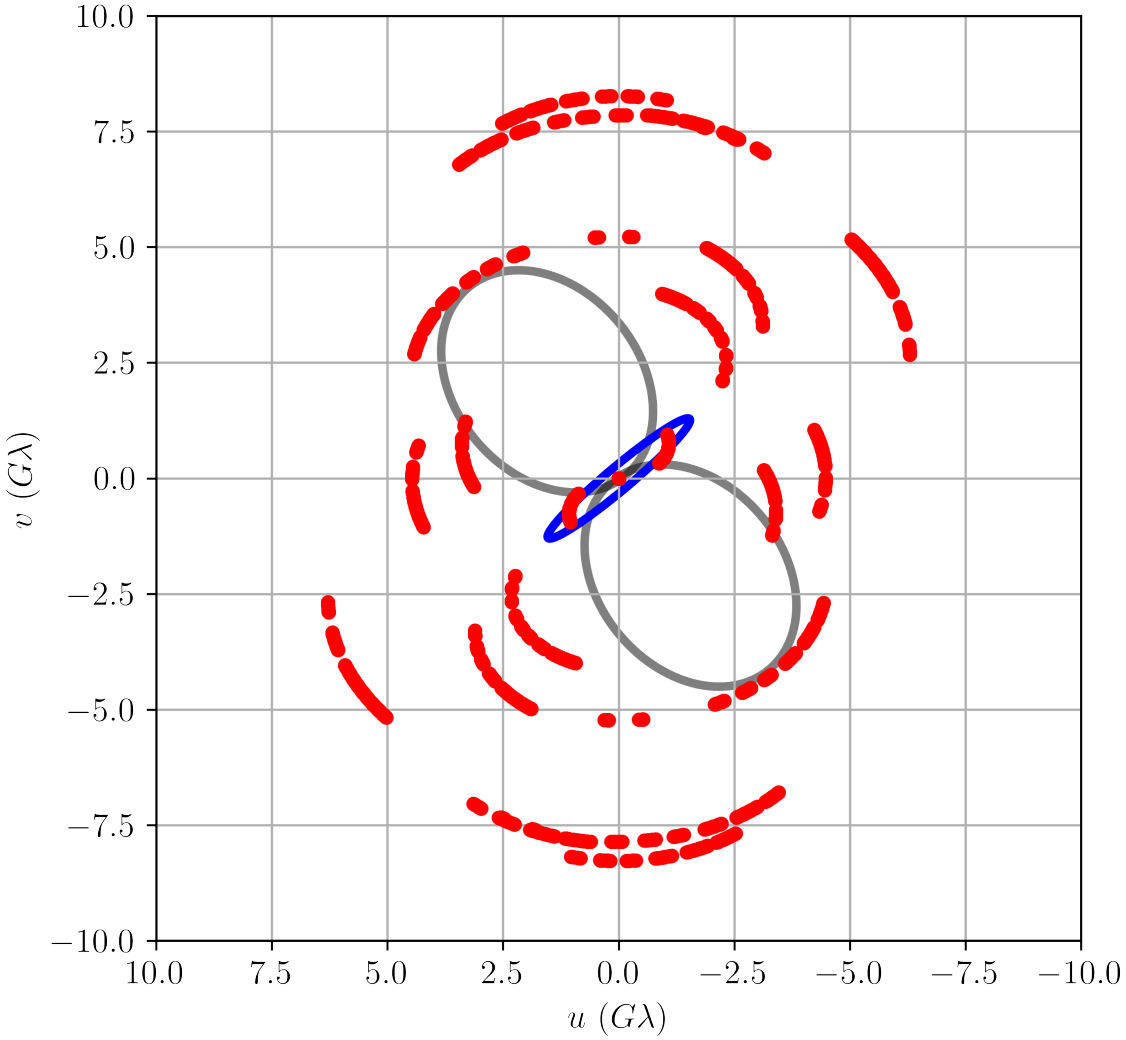

Figure 2.1: The current $(u, v)-$coverage of Cen A on April 10, 2017. The red lines are the $(u, v)-$track. The blue circle represents the size of Cen A in the Fourier space. The gray circles shows the large cavities in the $(u, v)-$space, where the Cen A jet is oriented.

data pre-processing to improve data quality. For the total intensity data, we adopt the following calibration:

1. Intrasite baselines (ALMA-APEX and SMA-JCMT) are removed, to avoid impact from the large-scale jet structures.
2. A self-calibration approach is used to stabilize the visibility amplitudes over a period of 10 seconds.
3. Anomalous S/N and anomalous amplitudes (3 sigma outliers in 500s segments) are flagged out.
4. Around 50min of LMT data (UT8.8 to 9.67) are removed as the pointing error is too significant to be corrected by the previous calibrations.

Similarly, for the linear polarization data, we also the intrasite baseline (ALMA-APEX) to avoid contamination from the large-scale structure from the jets.

The large scale structure-related issue, however, is different. Usually for other EHT targets, the two bands are combined to increase the data volume, including Janssen et al. (2021); however, upon examining the data more closely, we notice that the two bands are different in a non-negligible manner. This discrepancy exacerbates for the polarization data. We believe that this is attributed by the large-scale structure of Cen A jet, as we have mentioned in the earlier subsection. A more detailed analysis will be discussed in Section 2.6.3, but for now, all our results are studied and analyzed separately for the two bands, and all the intrasite baselines are removed, if not stated otherwise.

Finally, given the EHT dataset of Cen A, we can neither change the orientation of the jet, nor change the VLBI array. As a result, the image quality of Cen A from the 2017 EHT data is inevitably compromised from the nature of the data. This prompts the usage of Bayesian method to explore the posterior of the constructed image library that represents the data, as opposed to find one image with the highest likelihood. We will discuss details about our method in the next section.

2.3 Method

The method we are going to use here is a Bayesian-based pipeline, THEMIS, which has been widely used in the total intensity and polarization studies of various EHT results,

including the two horizon targets, Sgr A* and M87*, as well as several AGNs (Event Horizon Telescope Collaboration et al., 2019b, 2021a, 2022c, 2024a; Kim et al., 2020; Issaoun et al., 2022; Jorstad et al., 2023). The detailed introduction to THEMIS can be found in Broderick et al. (2020b,a). Here, we provide a brief introduction to the algorithm, and specifics that are relevant and tuned for Cen A.

THEMIS, as a Bayesian method, is able to explore the imaging posteriors for the full polarizations (including circular polarization), with a non-Reversible parallel Tempering: Deterministic Even-Odd (DEO) swaps (Syed et al., 2021) and the Hamiltonian Monte Carlo (HMC) sampling algorithm. The full Stokes description of the polarization that THEMIS samples can be presented in the Poincaré sphere as:

$$\begin{pmatrix} \mathcal{I} \\ \mathcal{Q} \\ \mathcal{U} \\ \mathcal{V} \end{pmatrix} = \mathcal{I} \begin{pmatrix} 1 \\ \mathcal{L}\sin\theta\cos\phi \\ \mathcal{L}\sin\theta\sin\phi \\ \mathcal{L}\cos\theta \end{pmatrix}, \tag{2.1}$$

where $\mathcal{I}$, $\mathcal{Q}$, $\mathcal{U}$ and $\mathcal{V}$ are the four Stokes parameters, presenting the total intensity, two linear polarization modes and the circular polarization. $\mathcal{L}$ is the polarization fraction, and θ is the EVPA and ϕ is the ellipticity, both of which are the two angles when projecting the polarization vector onto the Poincaré sphere.

The models that THEMIS uses to fit for the total intensity images are rectangular rasters, whose grid points are treated as model controlling points. The model parameters in these raster models include $\mathcal{I}$ at each grid point of the raster, and the field of view and the position angle of the raster. The size and geometry of the THEMIS models need to be pre-determined by finding the maximal Bayesian evidence for different raster resolutions. This entire process of acquiring the optimal model is described in Section 2.4.1. And the same model will be used to fit both the total intensity and polarization data. Similarly, the models that are used to fit the polarization data are the same rectangular rasters as in the total intensity fitting, albeit include the full polarization description: $\mathcal{I}$, $\mathcal{L}$, θ and ϕ at each grid point of the raster. That is fitting the Poincaré sphere at every grid point for the raster. After fitting the THEMIS raster models to the visibility data, we interpolate among the control points using bicubic spline, through which THEMIS is able to achieve "super resolution" in spite of the resolution limitation imposed by the (u, v)-coverage.

What marks THEMIS different from non-Bayesian algorithm is that THEMIS simultaneously fits telescope gains and leakages, as part of the image/polarization constructions. Stations gains are associated with the variations in the sensitivity and response of individual antennas or stations in a radio telescope array. Polarimetric leakage, on the other

hand, is unique to polarization detection, where an antenna or receiver that is meant to measure, for example, left-hand polarization, also picks up some right-hand signals. The telescope leakages for EHT data is in general worse than average due to the fact that EHT adopts a 2 GHz bandwidth. The impact of gains and leakages can be described by Jones matrix (Jones, 1941; Thompson et al., 2001):

$$J = \begin{pmatrix} G_R & 0 \\ 0 & G_L \end{pmatrix} \begin{pmatrix} 1 & D_R \\ D_L & 1 \end{pmatrix} \begin{pmatrix} e^{-i\phi} & 0 \\ 0 & e^{i\phi} \end{pmatrix}, \tag{2.2}$$

where G_R and G_L are the right- and left-gains, and D_R and D_L are the right- and D-term corrections. More specifically in THEMIS, the stations gains are set to be one, while permitting variance in among different scans. On the other hand, the polarimetric leakage corrections are presumed to be constant throughout the observation but not necessary equal between the right- and left-hands.

The data to be fitted by THEMIS, pre-processed as described in Section 2.2, are all scan-averaged complex visibilities, with a 2% (3%) multiplicative error budget to capture the systematic noise introduced by telescope's thermal noise, for the total intensity (polarization) data. The high and low frequency bands are fitted independently. Moreover, the intrasite baseline data are removed to avoid possible complications from the aforementioned large-scale structure.

2.4 Total Intensity Imaging

In this section, we present a total intensity analysis of Cen A, utilizing the EHT data. We will use the high and low bands data independently, whose calibration procedure has been described in Section 2.2. We start with a raster survey to determine the best THEMIS model, surveying different raster size and geometry. We then explore and test the models on the synthetic data from Janssen et al. (2021), before finally make the total intensity analysis with the two EHT datasets.

2.4.1 Raster Survey

The hyperparameters associated with THEMIS models are the raster size and geometry of the raster models, the two hyperparameters describing the two-dimensional size of the raster. These two free parameters must be determined before the actual fitting takes place. There are essentially three different methods in surveying the hyperparameter space:

1. Traditionally in VLBI imaging, a priori knowledge of the dataset is often used to find the parameters. In the case of EHT data, the nominal resolution of 15μas may put constraints on how many controlling points are needed in the raster model.

2. Performing surveys across viable models by optimization is the second method. Optimization can quickly finds the local maximum in the likelihood space. Calculating the Bayesian information criteria (BIC) based on the optimized result gives hint on the probability of the model given the data.

3. The more precise, yet more computationally expensive method is to survey the each viable model with a full THEMIS fitting. Then, we can compare the Bayesian evidence to determine the most appropriate hyperparameters.

The first image of Cen A in Janssen et al. (2021) shows us the size of Cen A as roughly 200 μas and 50 μas along and across the jet. The size, along with the nominal EHT resolution of 15 μas, gives the rough size of the raster as around 14 by 4. However, it would be unwise to set it as the fiducial model directly. In the case of Cen A, a wrong model may severely limit our capability to produce images that represent the data, given the large number of model parameters and the known data challenges, especially the sparse $(u, v)-$ coverage.

In contrast, optimizing offers a quantified metric to estimate the model probability given the data: the BIC. The BIC is defined as

$$BIC = -2\mathcal{L}_{\max} + k \log(N), \tag{2.3}$$

where $\mathcal{L}_{\max}$ is the maximum log-likelihood, and k is the number of parameters of the model, and N is the number of data points. The BIC penalizes models with high complexity, which discourages overfitting, as a more complex model can easily achieve higher likelihood simply because it has more flexibility.

However, optimizing may run into problems that the models may be trapped in local maximum. This problem becomes more prominent when the models have large number of parameters. In other words, there is no guarantee that a simpler model cannot achieve better BIC with more complicated models. This becomes especially true when the optimized results yield similar BICs. In the case of Cen A, after initial optimization, we recover a few similar yet different morphologies, some of which may due to aliasing. These image morphologies could be the results of aforementioned problem of local maximum in the likelihood space. The optimizing result and the different morphology patterns can be found in Section A.1.

Hereby, we survey the hyperparameter space with the hybrid of the latter two methods, optimizing and full THEMIS fitting. In more details, we perform raster survey across different raster size and geometry with optimizing; for models with similar BICs, we then initiate full THEMIS fittings on the EHT data, initializing the models with the optimizing results. Finally, we will be able to directly compare the Bayesian evidence, which is equivalent to BIC when the MCMC fitting is converged.

As mentioned above, the size of Cen A jet gives a rough estimate of the raster of 14 by 4. Thus, the raster survey would cover the number of controlling points between 10 to 18 along the jet, and 3 to 6 across the jet. The BIC values after optimization show minimum at between number of parameters of 40 to 90. Among those possible models, we perform full THEMIS fitting on the high band data. The models we survey include models with different raster geometries, whose results are tabulated in Table 2.1, in which the model of 16 by 4 outperforms the rest. And from now on, we will use this raster size for all the THEMIS fittings, as the fiducial model.

2.4.2 Total Intensity Fitting to the Synthetic Data

The objective of this subsection is to validate the selected model's performance by applying it to a set of synthetic data that closely resembles the characteristics of the images of Cen A from Janssen et al. (2021). This step is crucial for ensuring the model's robustness and its ability to accurately represent the complexity of the observed data. The synthetic dataset that we are going to leverage here is from Janssen et al. (2021), which was generated for the purpose of validate the jet-counterjet pair structure, as well as their method's robustness. The synthetic data, based on the ground truth image from Janssen et al. (2021), includes simulated parameters of the Earth's atmosphere, the noise introduced from the telescopes (gains, leakages, pointing errors and thermal noise), and is observed assuming the same telescope sensitivity and $(u, v)-$coverage as the real observation. The subsequent data calibration followed the exact same settings as the real data.

We then apply raster models acquired from the raster survey to the synthetic dataset. Not only do we apply the fiducial model of 16 by 4, models with different raster geometries are also used to fit the synthetic data, as a side-by-side comparison. The models inlude the fiducial 16 by 4 raster, as well as the 18 by 6 and 14 by 6 rasters. The initial configuration of the model parameters is a Gaussian of the size of the model-underlined raster. The prior for the model parameters is logarithmic, whose lower and upper bounds are e^{20} and e^{40}, in the unit of Jansky per steradian of each pixel. We then employ THEMIS, exploring the likelihood space. The convergence of the MCMC chains is monitored using DEO diagnostics to ensure robust parameter estimation.

The fitting result of different models to the synthetic data is assessed using a collection of statistical measures including the reduced chi-square test, the cross-correlation test, residual analysis, and the Bayesian evidence. These metrics provide insight into the model's adequacy in capturing the underlying structure of the synthetic data. The following shall present all the fitting results, along with the analysis results.

In Figure 2.2, we show the best fitted images for the three different models, 16 by 4, 14 by 6 and 18 by 6, compared with the ground truth. Despite the model's large number of model parameters and the (u, v)-coverage limitations of the data, THEMIS is able to produce very similar morphologies to the synthetic ground truth: a brighter southern limb of the jet as compared with northern one; faint emissions in the northeast; a faint counter-jet. However there lies caveats in understanding this initial success: these models are optimized and selected for the real EHT data. As a result, the best models to describe the EHT data may present model misspecification for the synthetic data. This "model misspecification" is supported by the cross correlation test and the reduced chi-square test. The reduced chi-square test yields results for the three models are: 1.46 for the model 18 by 6 , 2.32 for the model 14 by 6 and 5.0 for the model 16 by 4. The Bayesian evidence also tells the same story: -2080.5 for the 18 by 6, -2251.49 for the 14 by 6 and -2744.35 for the 16 by 4. There is a clear trend that the synthetic dataset strongly prefers more complex models. As we will present in the following sections of the analysis of the EHT data, there is a noticeable difference between the underlying image of the EHT data vs the synthetic data.

As a result, the fitting of the synthetic data serves as a very important reminder of how important it is to select the most appropriate model when it comes to different datasets. Nevertheless, we also demonstrate that THEMIS is able to construct the total intensity map with challenging datasets, especially with $(u, v)-$ coverage so sparse in the direction of the jet. The insights gained from this exercise guide the subsequent fitting of the model to the actual data, ensuring a reliable and accurate total intensity map of Cen A.

2.4.3 Best Total Intensity Fitting to the EHT Data

On top of the insights we have gained from the model survey and the synthetic data test, we apply the fiducial model to the actual EHT observations of Cen A. Exploring the model on two EHT datasets, high and low bands, with Bayesian method, the goal is to refine the model parameters to accurately reflect the observed intensity distribution, constructing a detailed intensity map of Cen A.

As discussed in Section 2.2, the EHT data for Cen A undergoes a series of calibrations, including correction for instrumental effects, and any necessary pre-processing, to ensure

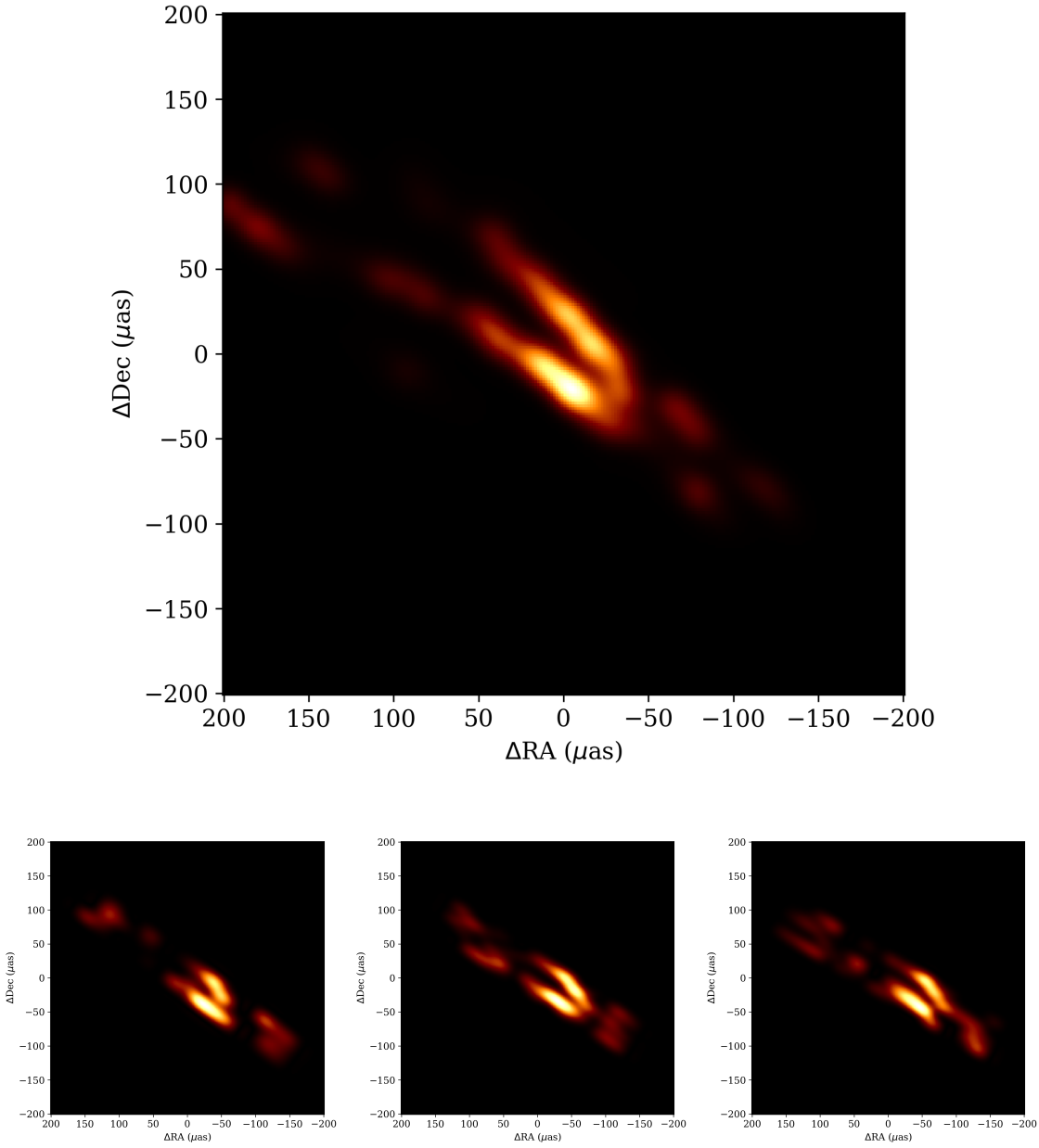

Figure 2.2: Top: the ground truth of the synthetic data. Bottom: from left to right are he best fitting images with the highest likelihood values, from 16 by 4 (left), 14 by 6 (middle) and 18 by 6 (right), each of which is blurred by a 15μas Gaussian.

the data are in a suitable form for model fitting. Based on the model selection through raster survey, the fiducial model of the raster size 16 by 4 is used to fit the high and low bands EHT data. However, we also include a series of models with different raster sizes and geometries, to build a full panorama of potential representations of the Cen A data. Thus, we are able to have two comparisons: comparison across different models and between two different datasets. The models are configured with initial parameter values from the insights gained from the synthetic data fitting; therefore, the model parameters from the best fitting result in the synthetic data test, i.e. the best-performed model of 18 by 6, are used to initialize the MCMC fitting of the real data. The MCMC process is carefully monitored for convergence and adequacy, ensuring that the parameter space is thoroughly explored through a collection of similar aforementioned diagnostic tools: parameter trace plots analysis, residuals analysis and the DEO diagnostics etc. This evaluation step is crucial for deciding the convergence of the MCMC chains and assessing the model's ability to capture the features of the observed intensity distribution of Cen A.

The fitting to the high band data with different raster models demonstrates a variety of different yet similar morphologies for the different models. We especially explore the performances of different raster models centering around the fiducial model, by increasing and decreasing the number of controlling points along and across the jet direction. The results are shown in Figure 2.3, which include the best fitting results with the highest likelihoods for each model. The highlighted image is the result for the fiducial model of 16 by 4.

Visually, there exists two morphologies of the Cen A jet across different models. The first one, which is more dominant and is for the fiducial model, puts the apex (where the black hole is supposed to be) towards the southwest corner; while the other one puts the apex more into the northeast. This is not unexpected, given the lack of $(u, v)-$ coverage in the jet direction. To analyze the performances of each model, the primary metrics used is the Bayesian evidence, which is listed in Table 2.1. The Bayesian evidence shows that the fiducial raster model of size 16 by 4 outperforms the rest of the models.

Second, we show the comparison between the two similar datasets, the high and low bands, both fitted with the fiducial raster model of 16 by 4. The MCMC fitting also demonstrates a high level of fidelity. In Figure 2.4, we show a selection of nine images randomly drawn from the image posterior distribution from the MCMC fitting of the low band data. The high degree of robustness of the fitting can be further seen in the bottom row, where we show the image with the highest likelihood, the mean and the standard deviation images from the image posterior distribution, where the standard deviation is plotted in logarithmic scale. The fitting results on both bands show a high degree of similarities, in terms of the distribution of emissions along the jet, which can be seen from

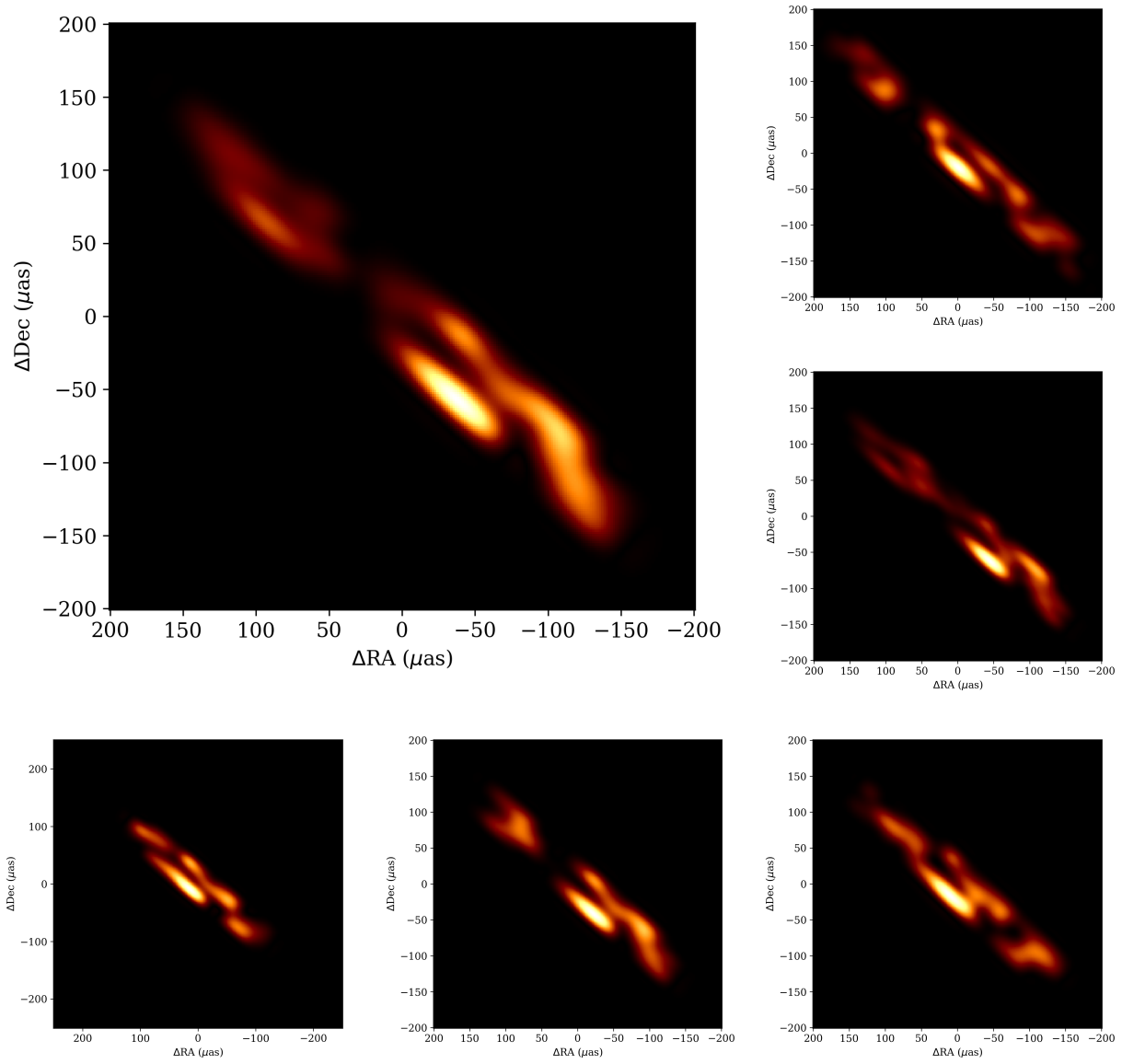

Figure 2.3: Top left: the best fitting image of the high frequency band with the highest likelihood of the 16 by 4 raster model. Bottom three panels: from left to right are the best images of the raster models of 12 by 4, 14 by 4 and 18 by 4. Right column: up to down are the best images of the raster models of 16 by 3 and 16 by 5. All convolved with a 15μas Gaussian beam.

N_y	N_x			
	12	14	16	18
3	-	-	-1973.06	-
4	-1906.33	-1835.17	-1827.41	-1844.91
5	-	-	-1845.05	-
6	-	-1875.56	-	-

Table 2.1: Dependence of the Bayesian evidence on Nx and Ny for the High Band Data Set of the 2017 April 10 EHT Observations of Cen A

the highlighted panel in Figure 2.3 for the high band and Figure 2.4 for the low band. A cross-correlation test gives value of 0.98, further indicating the robustness of the image constructions results.

Our Bayesian imaging unveiled a morphology that closely mirrors the elongated jet and counter-jet alignment stretching southeast to northwest, measuring approximately 150μas in length. Visually, the jet reveals two distinct limbs: a consistent, albeit fainter, northern limb, and a notably brighter southern counterpart. A less luminous blob is identified at the northeast end. And there exists a prominent counterjet. Interestingly, while this depiction has parallels with the image in Janssen et al. (2021), for example, the "fork" shape near the apex of the jet, it also presents non-negligent differences: the THEMIS result shows a more helical structure of Cen A jet. However, this helical configuration is not uncommon in AGNs. One example is given in Fuentes et al. (2022) of the quasar 3C 279.

Fitting the real EHT data serves an important step in understanding the EHT Cen A data. The resultant constructed images of Cen A offer insights into the galaxy's core structure and emission mechanisms, which we will discuss in more details in Section 2.6. This analysis not only enhances our understanding of Cen A but also serves as mid-step to analyze the linear polarization map of Cen A.

2.5 Polarimetic Imaging

In Goddi et al. (2021), Cen A was reported detection of a weak polarization ($< 0.2\%$) with a flat spectrum, and the EVPA was not even reported as a result. In fact, the authors believed that an improved future data with spectroscopy is needed to determine the linear polarization for Cen A and its depolarization mechanism. We agree that a better future data with higher $(u, v)-$coverage would drastically improve the robustness and constrain

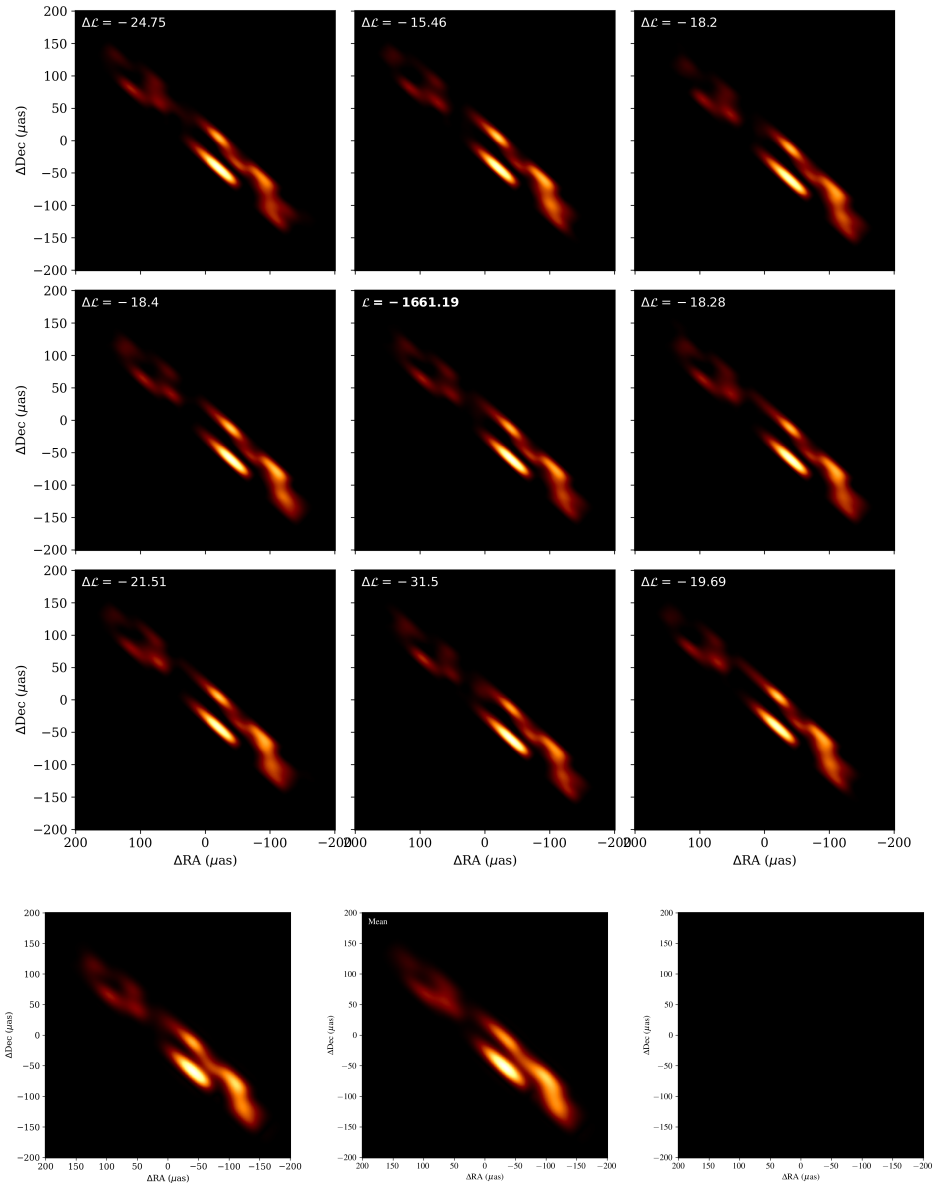

Figure 2.4: Top: the fitting posterior to the low band data. Bottom: from left to right are he best fitting image with the highest likelihood value (left), the mean image from the posterior (middle) and the standard deviation from the posterior (right), each of which is blurred by a 15μas Gaussian.

details of the image. However, in this study, we we are able to constrain and report the linear polarization values with posteriors distribution using the 2017 EHT data, albeit weak polarization and the aforementioned data quality problems.

2.5.1 Null Test with the Synthetic Data

The objective of conducting a null test using the synthetic data in our analysis stems from the fact that Cen A is a relatively weakly polarized AGN. Given Cen A's weak polarization signature, it is crucial to establish a robust baseline for our analysis methodologies to discern genuine polarization signals from noise and potential artifacts within the observational data.

The null test, involving the synthetic data from Section 2.4.2, which lacks any polarization, serves this purpose by allowing us to validate the sensitivity and capability of our MCMC fitting procedures. By ensuring that our analysis framework does not erroneously attribute significant polarization to data intrinsically lacking such signals, we can confidently interpret the subtle polarization features obtained in the actual EHT data of Cen A, providing insights into its magnetic field structure and emission mechanisms with a higher degree of reliability.

As such, we deploy THEMIS to fit the synthetic data, with the fiducial raster model of size 16 by 4. The outcome of this exercise is presented in Figure 2.5, where the posterior distribution is shown. Here, the vector ticks symbolizing the EVPAs appear scrambled and unfocused across the image posteriors, indicating a lack of consistent polarization direction. Additionally, the polarization fractions hover close to zero, and lack regions with consistent polarization detection.

Other diagnostics also points to non-detection of linear polarization, the most important of which is the D-term constructions. D-term coefficient, discussed in Section 2.3, is a quantification of polarimetric leakage between polarization hands in the instrument. The synthetic data, although lacks polarization, features a built-in 5% D-term coefficient in all telescopes, with the exception of Pico Veleta — an observatory location that lacks visibility to Cen A. THEMIS estimates the D-terms as part of its model-fitting procedure, and is able to generate posteriors for the leakage term of the synthetic data, recovering the 5% intrinsic leakage (see Figure 2.6). This result holds strong argument that THEMIS is discern zero polarization from systematic noises. A more detailed discussion will be continued in Section 2.6.2.

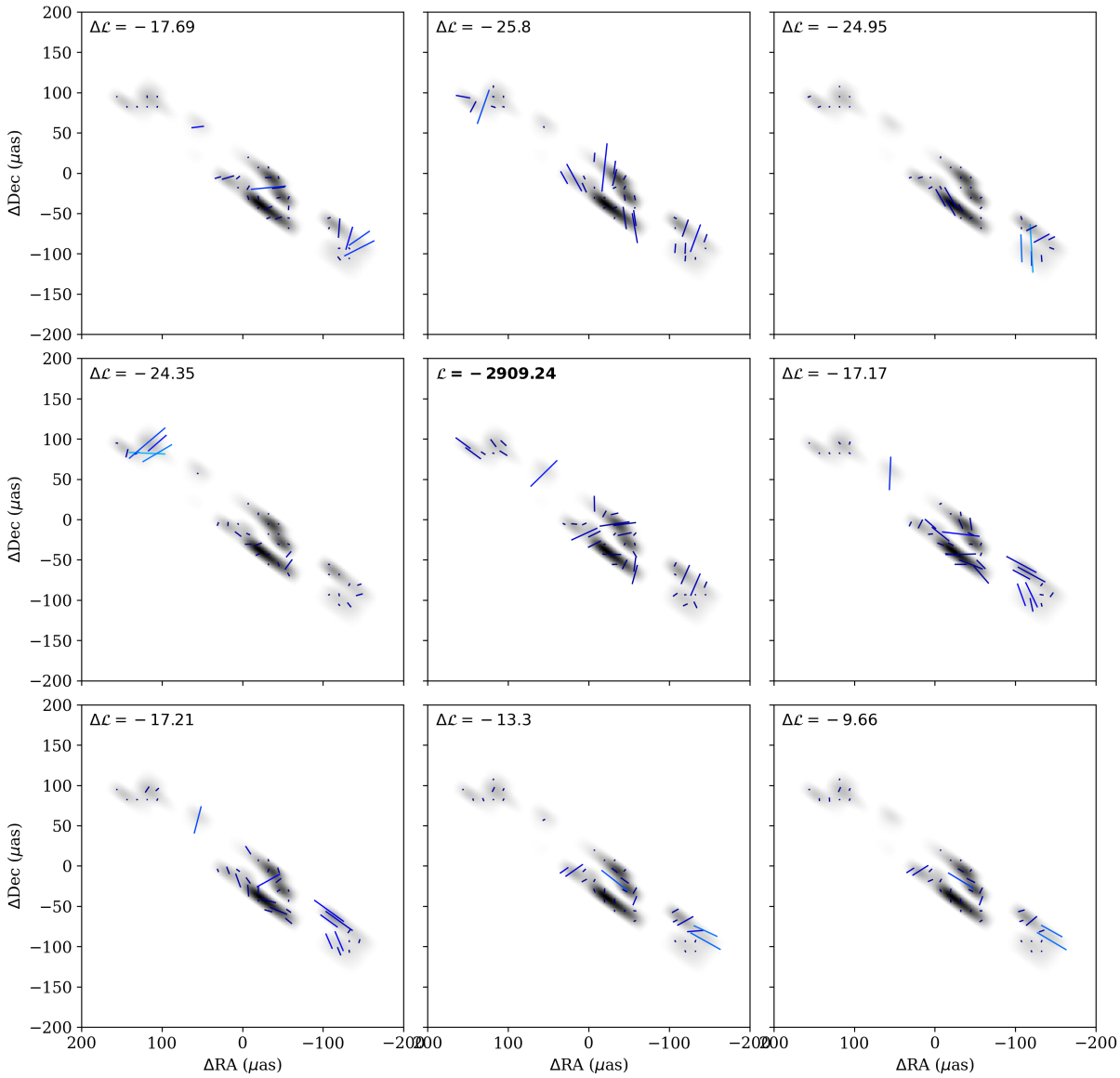

Figure 2.5: Image posteriors for the null test, where the 16 by 4 raster model is fitted to the synthetic data, which lacks polarization signals.

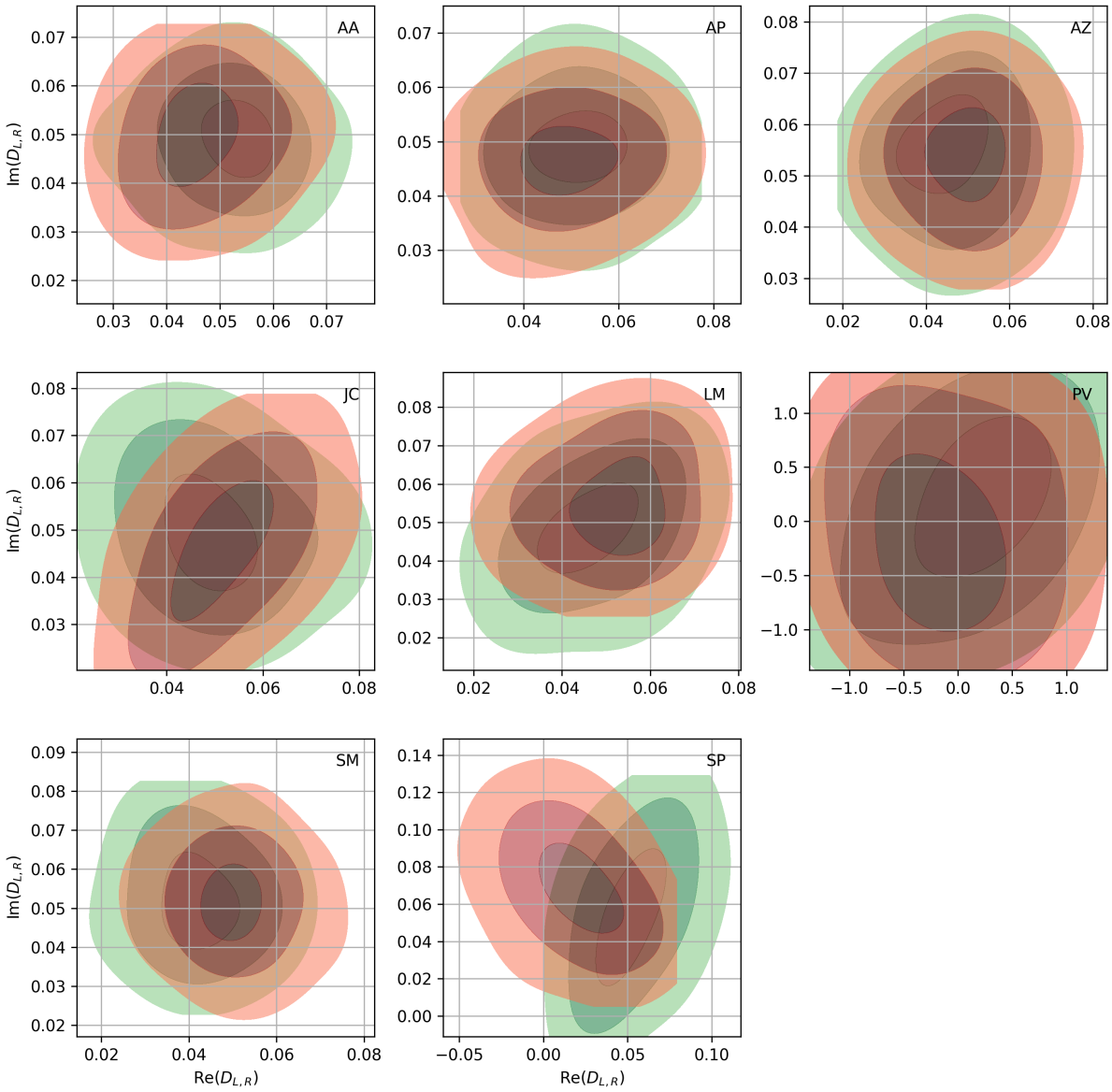

Figure 2.6: Posteriors of the D-term coefficients, as part of the model fitting to the synthetic data. The contours show 1σ, 2σ and 3σ regions. The red and green represent the two polarization hands.

2.5.2 Linear Polarization Images

In Figure 2.7, we present reconstructed linear polarization (LP) images of Cen A for both high and low bands, fitted independently. The data pre-processing is discussed in Section 2.2; in addition, the data is scan-averaged and added 3% of systematic noise.

The Cen A linear polarization exhibits high similarities for both high and low bands, in which the majority of the linear polarization lives in the apex of the jet. There is also a rotation of the EVPA from along the jet to across the jet near the apex. This rotation is visible in both frequency bands, which could be the transition from optically thick to optically thin. The overall polarization fraction is low, as expected, with the peak lower than 2%, as stated in Goddi et al. (2021). The biggest differences between the two frequency bands are the polarization structures in the regions away from the apex: the northeast blob and the southwest counterjet, although the differences are very small.

To understand the polarization structure statistically across different regions of the jet, we segment the image into five regions based on the jet morphology: three "cores" (C) and two "limbs" (L). The three cores are: the extended northeast blob (C1); the apex of the jet, potentially housing black holes (C2); and the counterjet (C3). The two limbs are the northern (L1) and the southern (L2) bright sheath of the jet. It is worth noting that the L zones and the C zones intersect with each other, as shown Figure 2.8. By analyzing a sample of one thousand images from our MCMC chain, we construct the posterior distribution for various metrics in these regions.

Following Event Horizon Telescope Collaboration et al. (2021a), we utilized two integrated metrics to quantify the LP fraction: an intensity-weighted average polarization fraction $\langle |m| \rangle$ and an averaged net polarization fraction m_{net},

$$\langle |m| \rangle = \frac{\Sigma_i \sqrt{Q_i^2 + U_i^2}}{\Sigma_i I_i^2}, \tag{2.4}$$

$$m_{net} = \frac{\sqrt{(\Sigma_i Q_i)^2 + (\Sigma_i U_i)^2}}{\Sigma_i I_i^2} \tag{2.5}$$

where I, Q and U are the Stokes parameters in the image-domain, and the subscript i denotes each pixel.

In Figure 2.9, we display the posterior distributions for the fittings to the high and low bands data, as well as the synthetic fitting result, of $\langle |m| \rangle$ and $m_{\rm net}$ and EVPA for the defined regions, with Gaussian fits on top. The inclusion of the synthetic test posteriors serves as another evidence of detection of weak polarization of Cen A from the null test.

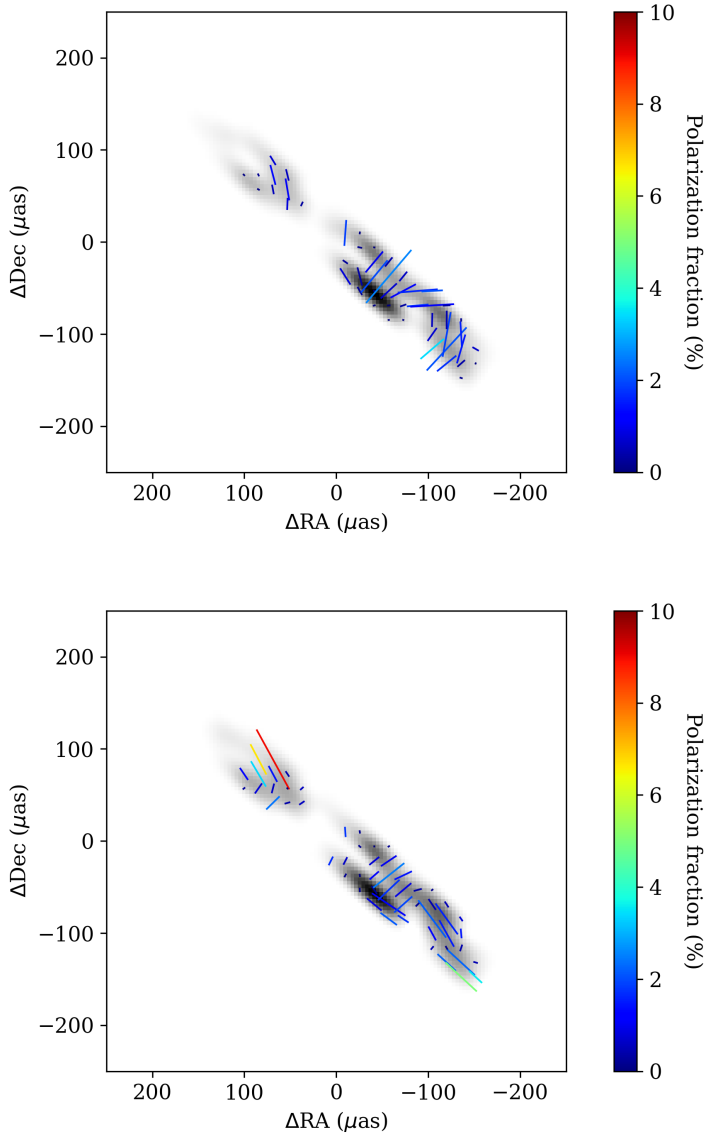

Figure 2.7: Top: the best linear polarization image to the high band Cen A data. Bottom: the best linear polarization image to the low band Cen A data. The base image in gray illustrates the total intensity, with the overlay features signifying the polarization characteristics. The length, color, and direction of these features provide insights into the magnitude, fractional polarization, EVPA, respectively.

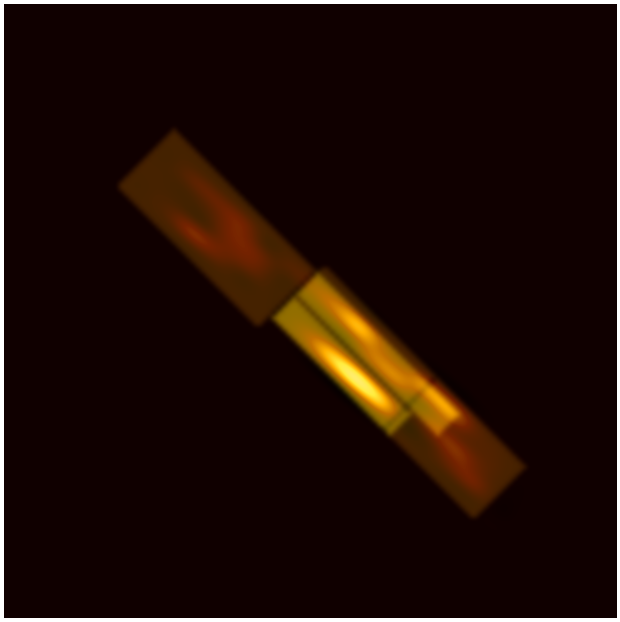

Figure 2.8: The segmentation of the Cen A image. Two colour schemes represent the "core" regions (red) and the "limb" regions (yellow).

The apex (C2) maintains a high degree of consistency between the frequency bands, among the three cores, attributed to its dominant intensity. Shown in Figure 2.7, its polarization direction appears mostly orthogonal to the jet, as evidence in the last column of Figure 2.9. A clockwise rotation in the EVPA from the intensity peak might be due to the transition from optically thick to thin. Similarly, the counterjet (C3) also exhibits the same linear polarization fraction in both metrics. The extended structure (C1) has the most disagreement in the polarization fraction between high and low bands on, although they still agree with each other within 1σ. The northern jet limb (L1) shows the most consistency in all the three posteriors. The southern jet limb (L2) also showcases consistency between the bands. L1 and L2 combined overlap almost entirely with C1, where the emission is the brightest.

Another very important comparison is that the red (low) and gray (high) histograms are all significantly larger than the blue (synthetic data) ones in the linear polarization fraction columns. While the blue regions hover over zero, the red and the gray clearly showcase small yet non-negligible linear polarization fractions, which we will discuss in Section 2.6.2.

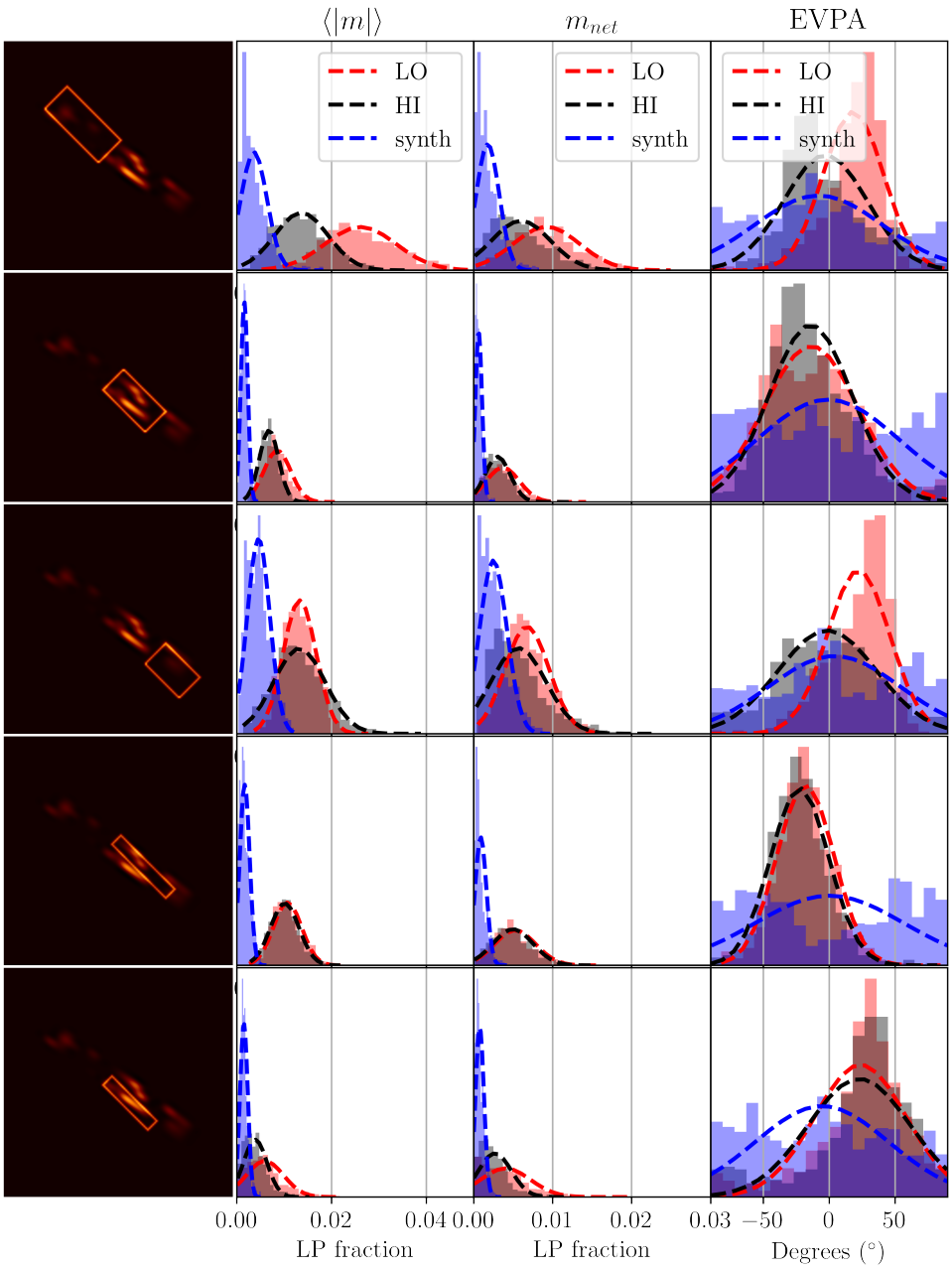

Figure 2.9: Posteriors for each segmented regions of Cen A, for linear polarization fraction (in two metrics) and the EVPA. Dashed lines are Gaussian fitting to the histogram. Black, red and blue represents the high band, low band and the synthetic data.

2.5.3 Key Diagnostics of the Linear Polarization Results

As a Bayesian-based imaging tool, THEMIS explores the posteriors of many uncertainties, as part of the diagnosis of the results. In linear polarization fittings, there are three important systematic uncertainties explored by THEMIS, which are the leakage terms, the gain solutions, and the underlined total intensity map.

The total intensity map from Section 2.4 is used to initialize the MCMC chain for its corresponding linear polarization fitting. As part of the four parameters explored for each controlling point in the model, the total intensity is also fitted during the exploration of the polarization map. Figure 2.10 highlights the high agreement between the frequency bands in five regions.

The telescope gains are also part of the posterior exploration. Similar to the total intensity fitting in Section 2.4, the telescope gains are solved for every step through a self-calibration approach. The gain solutions for the polarization fitting are shown in Figure 2.11. There is overall high level agreement between high and low bands. In general, most telescope gains are very close to unity, except for LMT and towards the end of the observation for SMT. This is not unexpected, as LMT suffered an overall pointing error during the observational campaign, and SMT had low-altitude obstruction at the end of its observation, both cases have been discussed in Section 2.2.

The two posteriors mentioned above are common for both the total intensity fitting and the polarization fitting, but leakage is a unique feature for polarization, where the signal for one polarization hand leaks in to the other. Since the D-term corrections are station-based quantities, independent of image reconstruction, the D-terms recovered for Cen A should be comparable to that of M87 on the same day. Figure 2.12 provides a visual representation of our results. The two panels, up for the high frequency band and bottom for the low frequency band, showcase the reconstructed D-terms. Superimposed on these plots is a cross, symbolizing the fiducial D-term derived for M87 on the corresponding observational day. Most D-terms are highly consistent with the M87 values, with the only exception of SMA.

In conclusion, among all three diagnostic metrics, the linear polarization posterior of Cen A between both frequency bands showcases the robustness of our fitting results, despite the overall low polarization fraction and the challenging dataset.

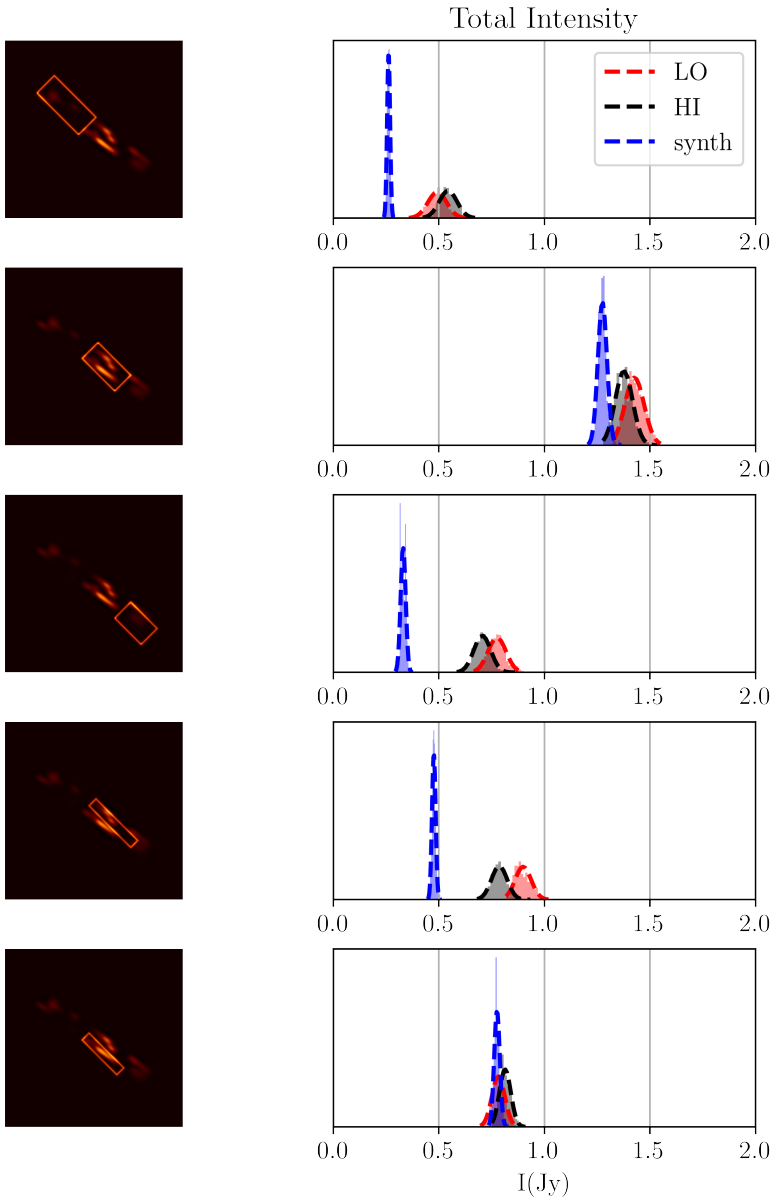

Figure 2.10: Posteriors for the total intensity by different regions. Dashed lines are Gaussian fitting to the histogram. Black, red and blue represents the high band, low band and the synthetic data.

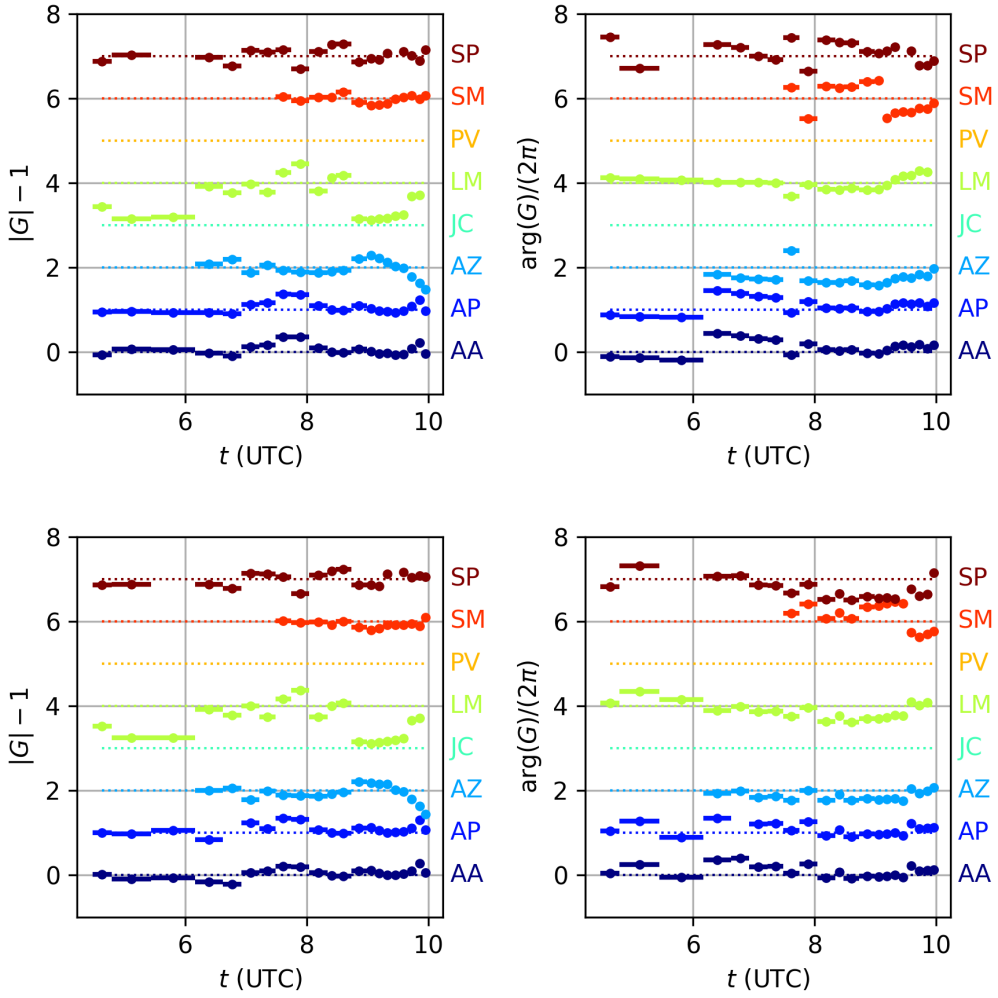

Figure 2.11: Top: Amplitude (left panel) and phase (right panel) of the telescope gain solutions to Cen A high band data. Bottom: Amplitude (left panel) and phase (right panel) of the telescope gain solutions to Cen A low band data. The vertical axis indicates different telescope station, offset to showcase each site, while the zeros in the amplitude and the phase are indicated by the horizontal lines. Values of PV and JCMT are absent because they are not included in the dataset, as PV cannot see Cen A and JCMT only has one polarization band, and thus has its data flagged.

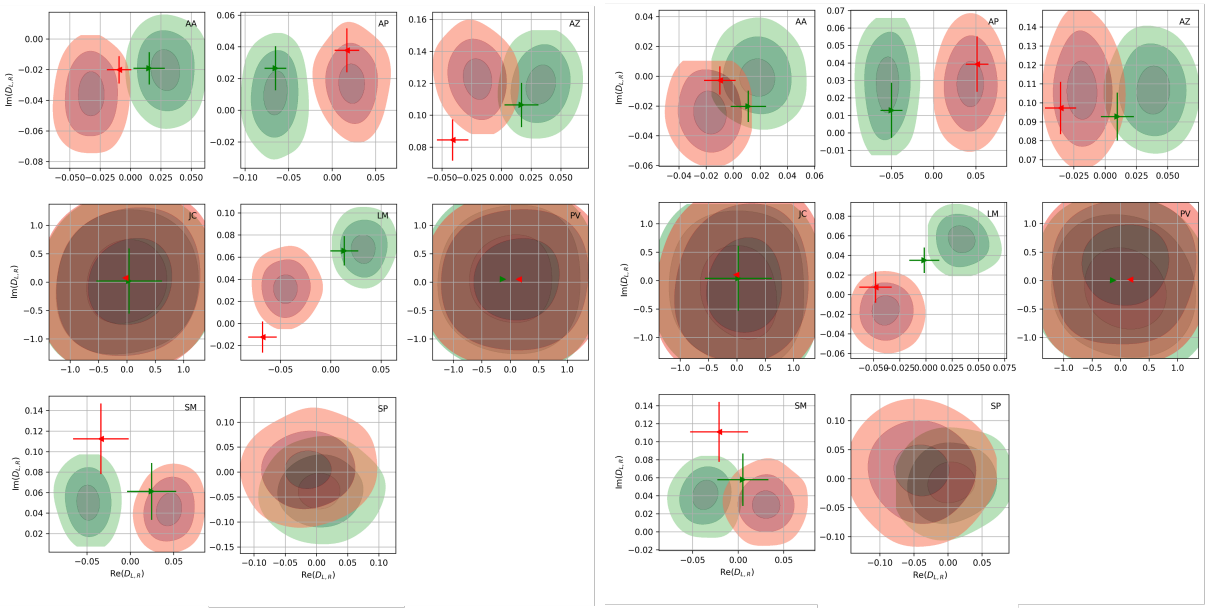

Figure 2.12: Posteriors of the D-term coefficients, as part of the model fitting to the synthetic data. The contours show 1σ, 2σ and 3σ regions. The M87* gain solution values are plotted with red/green points, with the crosses indicating the 2σ uncertainties. JCMT (JC) and IRAM30 (PV) display unconstrained D-terms, essentially showing the priors, due to two reasons: JCMT data is excluded because it only observes one polarization hand, and IRAM30, given its geographical positioning, inherently lacks the capability to observe Cen A. Also note the absence of the cross for SPT, which, analogously to IRAM30's inability to detect Cen A, cannot observe M87.

2.6 Discussion

2.6.1 Similarity and Differences with Past Publication

With the unprecedented resolution achieved by EHT, Janssen et al. (2021) was able to produce the first resolved structure of jet base of Cen A. However, due to the nature of the EHT $(u, v)-$coverage, a variety of underlined morphologies are able to describe the observed data. In fact, the multi-mode nature also applies to other EHT targets, especially Sgr A* (Event Horizon Telescope Collaboration et al., 2022b). Therefore, we deemed it necessary to produce a full posterior distribution of all the possible images described by the Cen A data.

Unlike the regularized maximum likelihood (RML) approach in Janssen et al. (2021), we apply the a Bayesian algorithm. The Bayesian approach differs from the RML approach in two fundamental ways. First, the Bayesian approach does not apply strong priors of our model, compared with the regularizers in the RML algorithm. Second, instead of returning the best fit image of Cen A in the RML algorithm, the Bayesian approach outputs a full posterior distribution of the likelihood. With the full posterior distribution, we are able to statistically assess the morphology of the target source and quantify the telescope gains at each telescope site. Similar Bayesian approaches have been applied to many past efforts of constructing and assessing images of the EHT targets (e.g., see Event Horizon Telescope Collaboration et al., 2019b, 2022c).

In lieu of the clear fork shape and the two prominent brightening limbs in Janssen et al. (2021), we nevertheless have a similar but different morphology of Cen A from THEMIS. Although the bright two limbs do exist, there is a large piece of southern limb missing as compared to Janssen et al. (2021). However, this morphology from THEMIS is not unique as there are other AGNs showing similar jet structure (Fuentes et al., 2022). Figure 2.10 showcases the difference of how the two methods differ at the distribution of the emission within the jet. The immediate attribution of this discrepancy is the lack of $(u, v)-$coverage in the NE-SW direction, which is the direction of the Cen A jet. In fact, as mentioned in Section 2.2, the largest cavity in the $(u, v)-$coverage map corresponds to the angular resolution of about 40μas. In other words, the 2017 EHT observation campaign of Cen A is unable to constrain structures of 40μas in the direction of the Cen A jet. This significantly impacts our ability to faithfully reconstruct the jet structure of Cen A, and hence the discrepancy.

The second possibility is that the Cen A image in Janssen et al. (2021) could be a local maximal in the likelihood space, given that the regularized maximum likelihood methods do

not produce posterior distributions. Although we are unable to constrain the jet structure as we would have hoped, THEMIS nevertheless provides a full posterior and the global maximal in the likelihood space, which features the most likely morphology of Cen A given the data. To verify this possibility that the morphology with two elongated bright limbs could be local maximal, we tested our model on Section 2.4.2, where we fit the THEMIS model to the underlined ground truth from Janssen et al. (2019), where the two limbs are both elongated and prominent. First, we notice that there are significant difference in how the flux is distributed between the jet in the fitting results of the synthetic and real EHT data. Second, when starting the fitting from the Janssen et al. (2019) image, although initially the produced image is able to maintain the two long bright limbs, the southern limb in the tentative image eventually starts to disappear. The final image fitted to the EHT data always drifts away from the Janssen et al. (2019), across different raster models.

The uncertainty in the structure of Cen A jet mainly comes from the lack of $(u, v)-$coverage, given the 2017 EHT observations. However, future observations, such as next generation EHT (ngEHT) would drastically improve the data. This can be achieved by increasing the number of telescopes in the southern hemisphere, and by performing multi-frequency observation of Cen A. In Doeleman et al. (2023), ngEHT proposes a multi-phase plan to build more telescopes across the globe with multi-frequency ability. The resulted $(u, v)-$coverage, shown in Figure 2.13 with multi-frequency $(u, v)-$tracks stacked, showcases how much the problem of telescope coverage can be resolved in the future.

2.6.2 Ability to Detect Weak Polarization

The authenticity of linear polarization detection can be challenged on two major grounds. The first skepticism surrounds the capability of THEMIS to discern faint linear polarization below certain threshold. If this were a limitation, THEMIS would invariably yield disparate linear polarization estimates for the identical source when the polarization fraction is meager. However, this notion is dispelled by the significant alignment in the results from the high and low band linear polarization analyses, elaborated comprehensively in Section 2.5.2, and with a cross-correlation value of 0.98. Revisiting the segmentation our image, we categorized Cen A into five interrelated subsections: the core, the diffuse emission zone, the counterjet, and the northern and southern jet structures, as in Figure 2.9. Remarkably, the derived linear polarization fractions for both the high and low bands, calculated based on two different metrics, consistently concur within a 1σ uncertainty, even though their absolute values predominantly linger below 1%. This consistency is mirrored in the EVPAs' posterior distributions, with the caveat that the EVPAs for the more weakly polarized segments aren't as precisely defined.

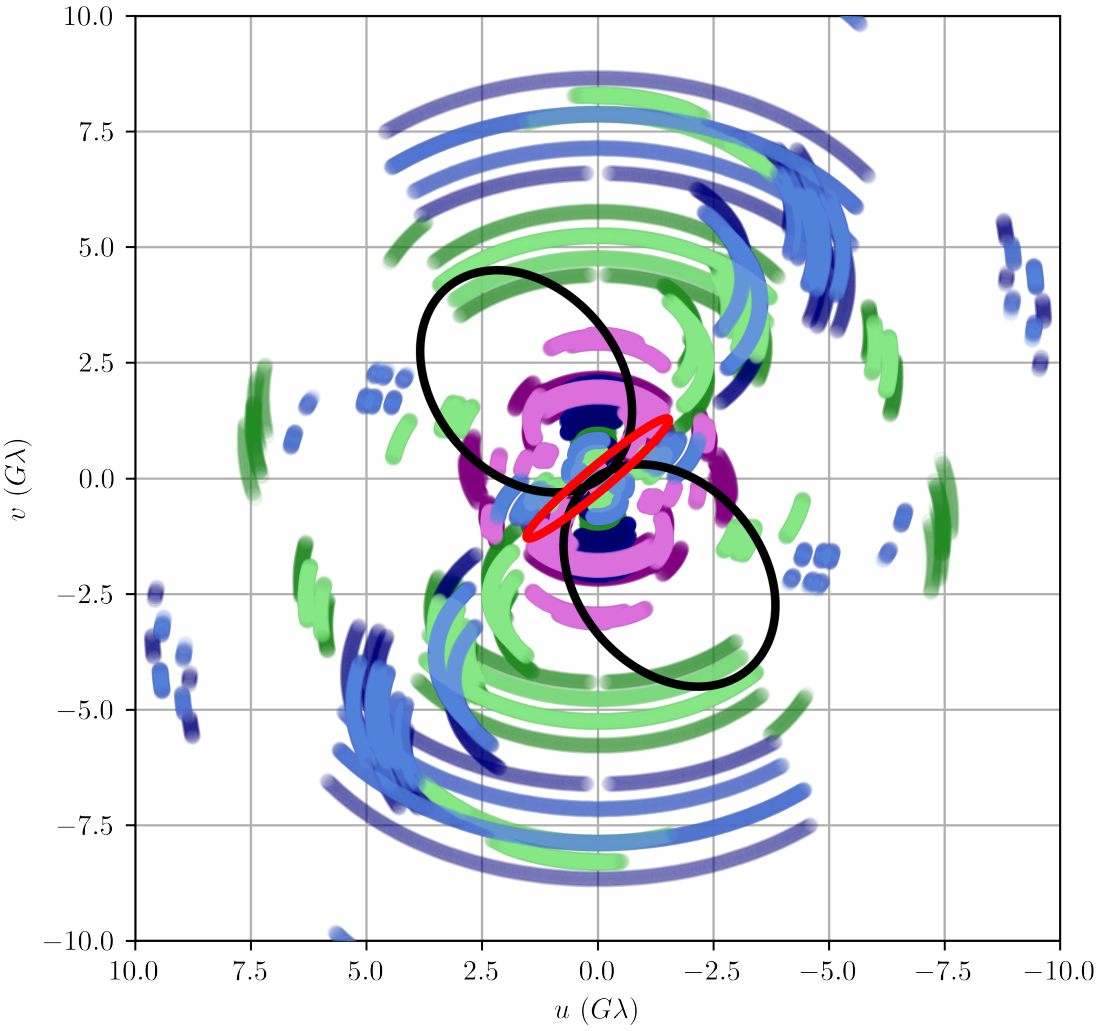

Figure 2.13: The future multi-frequency $(u, v)-$coverage of Cen A proposed. Purple, green and blue represent different frequencies ngEHT can observe (86, 230 and 345 Ghz). Light colors are the proposed phase one telescopes, while the shaded colors are for the proposed phase two. The black circles are the cavities in the current EHT $(u, v)-$coverage, and the red circle represents the size of Cen A jet.

The alternate hypothesis posits that the observed linear polarization stems from systematic noise introduced during data pre-processing. To rigorously preclude the chance of model inaccuracies or other anomalies potentially giving rise to erroneous detection of linear polarization signals, we deemed it crucial to conduct a null hypothesis test. Stated in Section 2.5.1 we applied the THEMIS polarization model to the simulated data where there exhibits no intrinsic polarization, but with 5% leakage at each telescope site. The null test clearly shows the non-detection of polarization and the recovery of the 5% leakage corrections, as in Figure 2.5 and Figure 2.6.

2.6.3 Implication of Large Scale Structure on Intrasite Baselines

We note that Cen A has one of the largest angular sizes on the sky. Early studies (see, e.g., Haslam et al., 1982; Remazeilles et al., 2015) at lower frequency show the size Cen A and other AGNs, where Cen A is measured around the size of degrees. This exceptional large size of Cen A, as an AGN target for the EHT, challenges two EHT "conventions". First, the concept of "zero-baseline", where the baseline between two very close telescopes are able to capture the entire flux of the target, is no longer valid for Cen A. Second, in the EHT, the high and low frequency bands data are usually combined to increase the volume of the data. However, the shear size of Cen A could make the two adjacent bands see different structures.

This piece of information has been known to us before the model fitting endeavors. As a precaution, we removed the zero-baseline data from both the high and low band datasets, to avoid the contamination from large-scale structure in both the total intensity and polarization fitting. However, we still want to address the influence of large-scale structure on the observational data of Cen A.

In Figure 2.14, the EVPA at ALMA-APEX baseline is plotted for both the high and the low frequency bands. Two features stand out: first, the EVPA for the two bands do not agree with each other; second, there is evolution for the EVPA across the first few hours of observation. These two outstanding features usually indicate two possible scenarios. First, the source itself undergoes some dynamic movements, example of which is Sgr A* (Event Horizon Telescope Collaboration et al., 2024a,b), causing variance in the EVPA. Second, there exists a strong Faraday rotation, which causes the differences in multi-frequency observations of EVPA. Although we cannot rule out the possibility that Cen A may have either intrinsic evolution or a strong external Faraday screen, the outstanding features may be a direct results of the aforementioned large-scale structure.

One possible explanation concerning this observational feature lies within the ALMA-

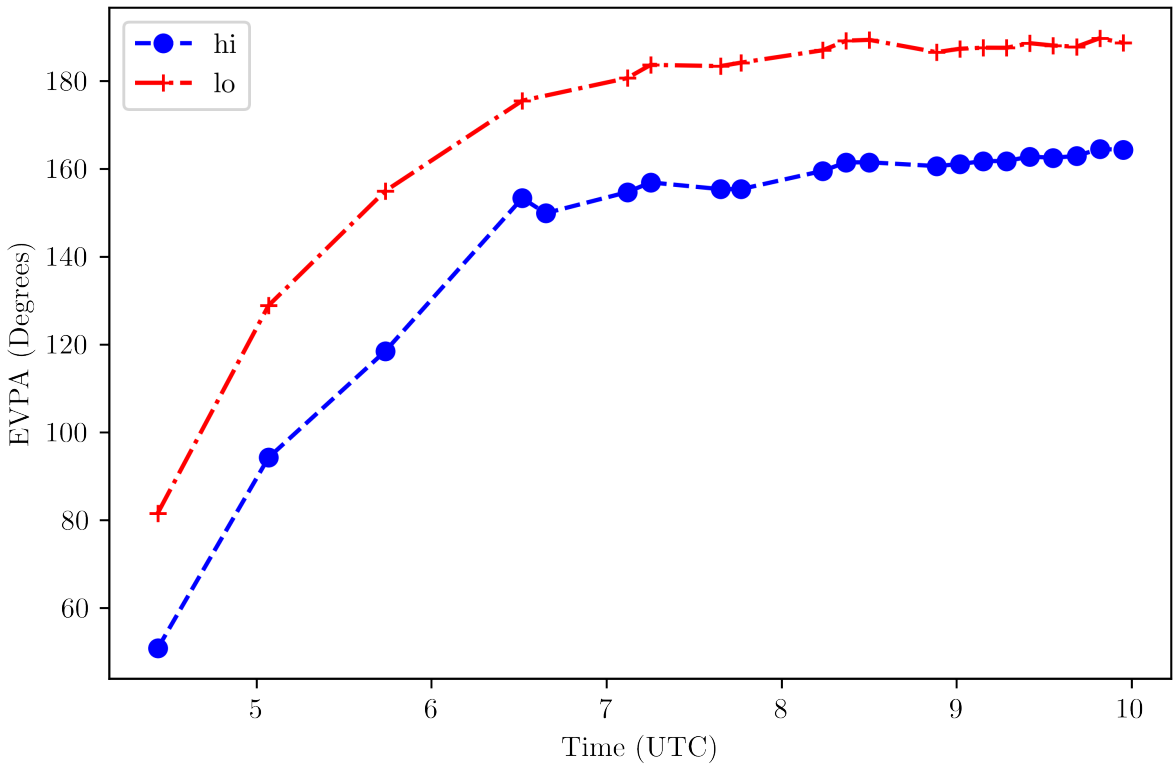

Figure 2.14: EVPA for ALMA-APEX baselines. The red line shows the low frequency band, and the blue line shows the high frequency band. Each point indicates the scan-averaged value within one scan in the simulated observation.

APEX baseline. The ALMA-APEX baseline in EHT is usually regarded as a zero-baseline for all the other EHT targets (Event Horizon Telescope Collaboration et al., 2019a, 2022a). This is typically true as no other EHT targets have significant structure on such large spatial scales, and this baseline should be able to capture the total flux. The distance between ALMA and APEX on average is less than $2M\lambda$. At this baseline length, the resolution is

$$\theta = \frac{\lambda}{D} \approx 0.1\text{”}. \tag{2.6}$$

At this angular size, what is different in Cen A is that we have potentially small-scale $(50 - 100\mu\text{as})$ structures separated by 0.1”. This is due, in part, to the fact that the EHT does not resolve a dynamically unique region in Cen A, as it does for M87 and Sgr A*. As a result, ALMA-APEX baseline is not a zero-baseline for Cen A.

Similarly for ALMA-APEX baselines, targets with large scale structures (that can be resolved by this baseline) will exhibit different complex visibilities when observed at adjacent frequencies, even only separated by $2GHz$ as in the EHT. Usually, the structure that can be resolved by this baseline can be approximated to be the same for the high (229.1 GHz) and low (227.1 GHz) frequency bands in EHT. However, for large targets like Cen A, this may no longer be the case. At this physical distance, the high and low frequencies can resolve, respectively:

$$\theta_{hi} = \frac{\lambda_{hi}}{D_{hi}} = 0.108\text{”}, \tag{2.7}$$

$$\theta_{lo} = \frac{\lambda_{lo}}{D_{lo}} = 0.110\text{”}. \tag{2.8}$$

For supermassive black holes and small AGNs, the difference of 1% is negligible, as there is no structure at this scale; however, for Cen A, the zero-baseline at these two frequencies are resolving different structures. A simple toy model can be designed to demonstrate this fact.

The toy model consists of two polarized Gaussians, which are 0.1” in size and separated by 30as. The two Gaussian blobs also include linear polarization. The first Gaussian blob has linear polarization fraction of 10%, with EVPA of zero degree. The second Gaussian blob has 20% linear polarization and 45 degrees of EVPA. When observed in the Fourier space, assuming same Dec and RA as Cen A and the same telescope settings, the visibility (for both total intensity and linear polarization) would have an oscillation with frequency of 1/30as enveloped by large oscillation with size of 1/0.1as. If, in the Fourier space, the difference for the Fourier frequencies of the high and low bands are larger than 1/30as, then

the observations at these two frequencies would see different visibilities, and vice versa. For the ALMA-APEX baseline, its Fourier frequency is

$$u_{AAAP} \approx 0.1", \tag{2.9}$$

and the Fourier frequency difference between the two bands is

$$\Delta u = u_{AAAP} \frac{\Delta\nu}{\nu} \approx \frac{1}{23"}, \tag{2.10}$$

where ν is the observational frequency, approximating to $230GHz$. As a result, the ALMA-APEX baseline would see difference in the visibility between high and low bands. This is shown in Figure 2.15. We also show the EVPA of the toy model at the ALMA-APEX baseline in Figure 2.16. Although this toy model does not include any temporal evolution nor undergoes external Faraday rotation, the large scale structure (30as separation) manifests itself in the EVPA as large sweeps over short periods of time, as well as difference in between the two frequency bands.

In conclusion, the known large-scale structure is expected to produce polarimetric behaviors on the ALMA-APEX baseline similar to those observed. Consequently, data on ALMA-APEX baseline is removed from the construction of the total intensity and linear polarization map of Cen A.

2.6.4 Jet Phenomenological Model

From the total intensity and linear polarized image of Cen A at 230GHz, obtaining estimates of plasma properties of Cen A becomes possible. By adopting a structured, self-absorbed synchrotron source, we are able to interpret the images in terms of physics parameters. To do that, assuming a phenomenological model with a conical, constant velocity jet, as in Blandford & Königl (1979), we derived a joint estimate of the magnetic field strength, B, and the plasma electron number density, n_e, based on three observational constraints: the fluxes, the optical depth and the linear polarization fraction at the core and the blob.

For this model, the underlined magnetic field is dominated by its toroidal component, which scales as $1/r$ due to current conservation:

$$B(r) = B_0 \left(\frac{r_0}{r}\right), \tag{2.11}$$

where r_0 is the assumed emission radius for the core, $r_0 = r_A$.

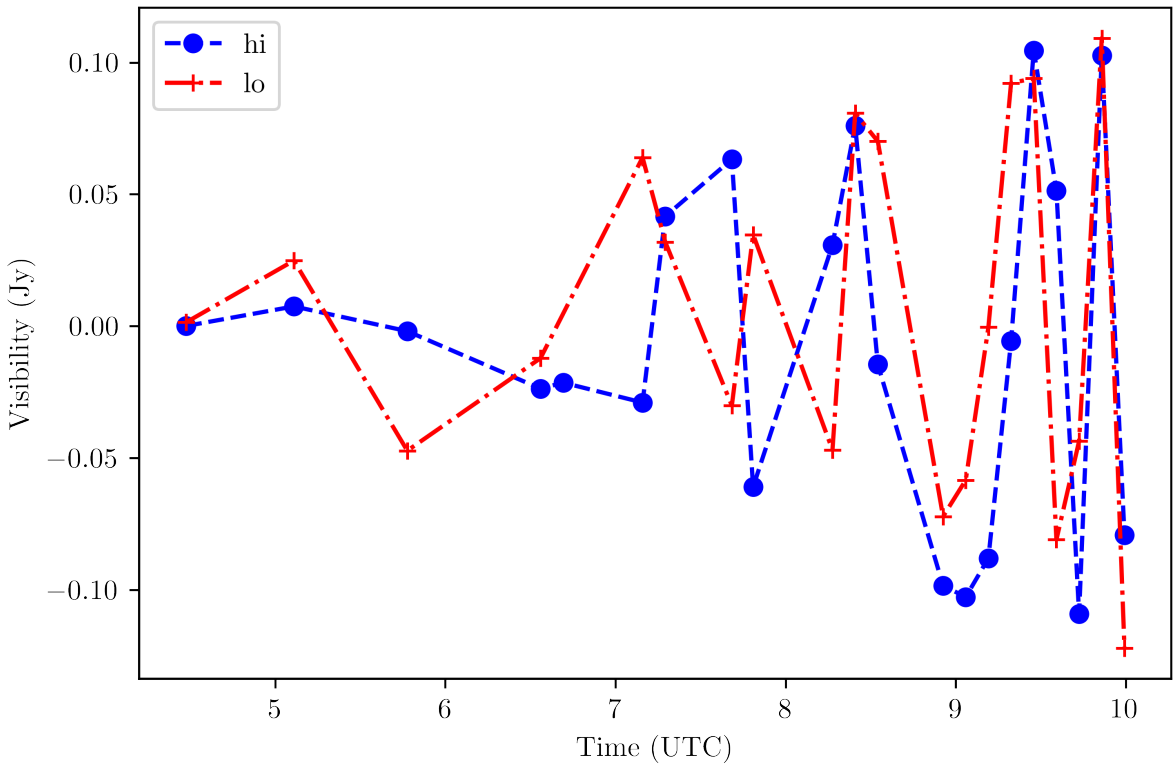

Figure 2.15: The visibility for the toy of double Gaussians. The red line shows the low frequency band, and the blue line shows the high frequency band. Each point indicates the scan-averaged value within one scan in the simulated observation.

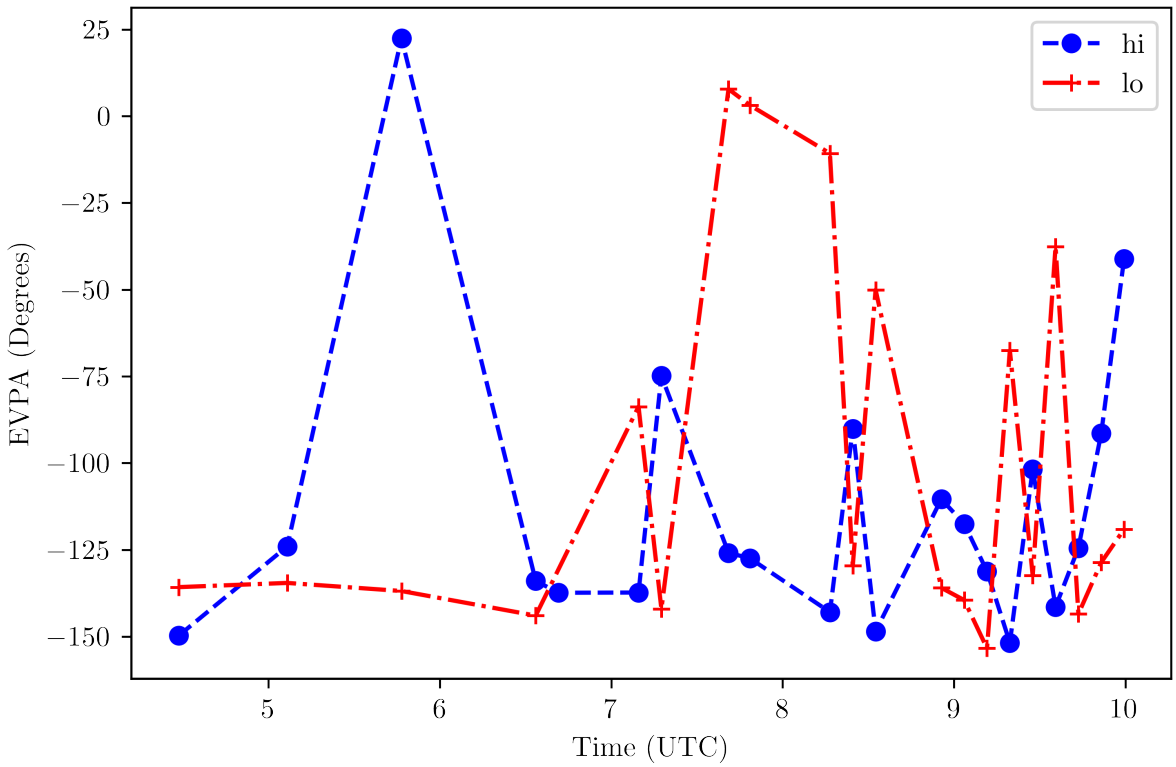

Figure 2.16: The EVPA for the toy of double Gaussians. The red line shows the low frequency band, and the blue line shows the high frequency band. Each point indicates the scan-averaged value within one scan in the simulated observation.

The electron number density, on the other hand, does not explicitly follow mass conservation because of the large population of nonthermal electrons. However, assuming the energy equipartition of the density of nonthermal particles to the electromagnetic energy density, we obtain similar scaling as the magnetic field strength as $n_e \propto B^2 \propto r^{-2}$:

$$n_e(r) = n_0 \left(\frac{r_0}{r}\right)^2 . \tag{2.12}$$

To assess the constraints of the magnetic field strength and the electron number density from observations, we write down the emission, absorption and rotativity coefficient:

$$\begin{aligned} j_\nu &= \frac{\pi}{2\sqrt{3}} \frac{(p-1)}{(p+1)} \gamma_m^{p-1} \frac{mc^2}{\lambda^3} \Gamma_j X y^{(p+1)/2} \\ \alpha_\nu &= \frac{\pi}{4\sqrt{3}} (p-1) \gamma_m^{p-1} \frac{1}{\lambda} \Gamma_\alpha X y^{(p+2)/2} \\ \zeta_V &= 2\pi \frac{1}{\lambda} XY \cos\theta = \frac{2\pi}{3} \frac{1}{\lambda} \cot\theta X y \end{aligned} \tag{2.13}$$

where

$$\begin{aligned} \Gamma_j &\equiv \Gamma\left(\frac{p}{4} + \frac{19}{12}\right) \Gamma\left(\frac{p}{4} - \frac{1}{12}\right) \\ \Gamma_\alpha &\equiv \Gamma\left(\frac{p}{4} + \frac{1}{6}\right) \Gamma\left(\frac{p}{4} + \frac{11}{6}\right) \\ y &\equiv 3Y \sin\theta \\ X &\equiv \frac{\omega_P^2}{\omega^2} = \frac{4\pi e^2 n}{m\omega^2} \\ Y &\equiv \frac{\omega_B}{\omega} = \frac{eB}{mc\omega}, \end{aligned} \tag{2.14}$$

and p is the power law index for the electron density distribution function, $dn = C\gamma^{-p} d\gamma$, whose typical value is 2. γ_m is the minimum microscopic Lorentz factor of the accelerated electron/positron population, whose typical value might range from 1 to 100. θ is the observing angle relative to the magnetic field. This should vary across the jet, but we might adopt the value of $\pi/4$.

We estimate the physical parameters of this jet model from the measurement of the images, as well as the reported values from previous publications (Janssen et al., 2021; Müller et al., 2014). These values include: The observations include some additional empirical quantities for the core (A) and blob (B):

r_i Radial location of the component in cm.

Ω_i Solid angle of the component in Sr.

m_i Polarization fraction of the component.

τ_i Optical depth of the component (we argue that $\tau_A > 1$ and $\tau_B < 1$ based on polarization rotation).

$F_{\nu,i}$ Integrated flux of the component at the EHT observing frequency, $\nu = 230$ GHz or $\lambda = 1.3$ mm.

The values of these quantities are tabulated in Table 2.2.

The first constraint comes from the optical depth, and the optical depth is

$$\tau = \alpha_\nu(r)\theta_j r = \frac{\pi}{4\sqrt{3}}(p-1)\gamma_m^{p-1}\frac{1}{\lambda}\Gamma_\alpha\theta_j r X y^{(p+2)/2}. \tag{2.15}$$

Under equalpartition of particle and magnetic energy density, we expect to see an optically thick core, and downstream the jet, the jet transits from optically thick to optically thin. This places an implied constraint on τ in the two regions, such that for optically thick gives,

$$\tau_A > 1 \quad \rightarrow \quad X_0 > \frac{1}{\bar{\tau}}\left(\frac{r_A}{r_0}\right)^{(p+4)/2} y_0^{-(p+2)/2}. \tag{2.16}$$

Similarly, the condition that the blob be optically thin gives,

$$\tau_B < 1 \quad \rightarrow \quad X_0 < \frac{1}{\bar{\tau}}\left(\frac{r_B}{r_0}\right)^{(p+4)/2} y_0^{-(p+2)/2}. \tag{2.17}$$

In the absence of a measurement of τ_A or τ_B, these two define a band of acceptable values of X_0 and y_0, and thus the magnetic field strength B and the electron number density n_e.

The second constraint comes from the flux of the jet, which is proportional to the emission profile. Because of the definite EHT resolution limited by the size of the Earth, we are able to resolve along, but not across, the jet. However, it can reasonably be assumed that the constant structures across the jet. In this case, the flux at the core and blob can be written as

$$F_\nu = \Omega\frac{j_\nu(r)}{\alpha_\nu(r)}\left[1 - e^{-\tau}\right], \tag{2.18}$$

where Ω is the corresponding solid angle to the emission region. The fluxes of the core and the blob and the measured emission region sizes, measured from the MCMC chain, hence, translate to the joint constraint on the $B - n_e$ $(X - Y)$ plane:

$$X_0 = -\frac{y_0^{-(p+2)/2}}{\bar{\tau}} \left(\frac{r_0}{r_i}\right)^{(p+4)/2} \ln\left(1 - \frac{F_{\nu,i} y_0^{1/2}}{f\Omega_i}\sqrt{\frac{r_0}{r_i}}\right), \tag{2.19}$$

where

$$f = \frac{2mc^2}{\lambda^2}\frac{\Gamma_j/\Gamma_\alpha}{(p+1)}. \tag{2.20}$$

Note that there is a natural transition from optically thin to thick when $\Omega \to 0$. Thus, the fact that the EHT is unable to fully resolve the jet width means that we can only place a lower limit curve in the $X - Y$ plane associated with the smallest flux and largest size consistent with observation (smallest brightness).

The last constraint is from the linear polarization fraction. The linear polarization fraction for optically thin synchrotron emission is

$$\bar{m} = \frac{p+1}{p+7/3} \sim 0.7, \tag{2.21}$$

where we set $p \sim 2$. However, this is significantly reduced by in situ Faraday rotation. We can estimate this by solving the radiative transfer equation, assuming no linear-circular polarization conversion. The solution is

$$S_\pm = \frac{\bar{m} j_\nu/\alpha_\nu}{1 \mp i\zeta_V/\alpha_\nu}\left\{1 - \exp\left[-\left(1 \mp i\frac{\zeta_V}{\alpha_\nu}\right)\tau\right]\right\}, \tag{2.22}$$

and thus

$$\begin{aligned} m = \frac{|S_+|}{I} &= \bar{m}\frac{\sqrt{1 - 2e^{-\tau}\cos(\tau\zeta_V/\alpha_\nu) + e^{-2\tau}}}{\sqrt{1 + (\zeta_V/\alpha_\nu)^2}\,(1 - e^{-\tau})} \\ &= \frac{\bar{m}}{\sqrt{1 + (\zeta_V/\alpha_\nu)^2}}\sqrt{1 + \frac{4e^{-\tau}}{(1 - e^{-\tau})^2}\sin^2\left(\frac{\tau\zeta_V}{2\alpha_\nu}\right)}. \end{aligned} \tag{2.23}$$

Unlike the previous two constraints, there is no explicit solution to Equation 2.23, as ζ_V/α_ν is independent of X, τ does depend on both X and Y. Beyond that, the periodicity introduced by the trigonometry would make the inversion non-unique. However, the general outermost bound may be determined using limiting expressions.

If $\tau \gg 1$, which is at the core (A), then

$$m_A \approx \frac{\bar{m}}{\sqrt{1+(\zeta_V/\alpha_\nu)^2}}, \tag{2.24}$$

which depends on Y alone, and is therefore a vertical bound in the X-Y plane at

$$y_A = \bar{y}_A = \frac{r_A}{r_0}\left\{\left(\frac{8\cot\theta}{\sqrt{3}(p-1)\gamma_m^{p-1}\Gamma_\alpha}\right)^2\left[\left(\frac{\bar{m}}{m_A}\right)^2-1\right]^{-1}\right\}^{1/p}. \tag{2.25}$$

If $\tau \ll 1$, which is at the blob (B), then

$$m_B \approx \frac{\bar{m}}{\sqrt{1+(\zeta_V/\alpha_\nu)^2}}\sqrt{1+(\zeta_V/\alpha_\nu)^2\mathrm{sinc}^2(\tau\zeta_V/2\alpha_\nu)}, \tag{2.26}$$

which oscillates down to the expression for Equation 2.24 when

$$\frac{\tau\zeta_V}{2\alpha_\nu} = \frac{\pi}{\lambda}X_B Y_B \cos\theta r\theta_j = \pi + k\pi \tag{2.27}$$

for any integer k. The lower bound in the Y-X plane (and thus B-n plane) occurs when

$$X_B Y_B = \frac{\lambda}{r\theta_j\cos\theta}, \tag{2.28}$$

and therefore

$$X_B = \frac{3\lambda\tan\theta}{r\theta_j}y_B^{-1}. \tag{2.29}$$

Matching these provides the desired curve,

$$X_B = \begin{cases} \dfrac{3\lambda\tan\theta}{r\theta_j}y_B^{-1} & \text{if } y_B < \bar{y}_B \\ \infty & \text{otherwise.} \end{cases} \tag{2.30}$$

In terms of X_0 and y_0 this corresponds to,

$$X_0 = \begin{cases} \dfrac{3\lambda\tan\theta}{r_0\theta_j}\left(\dfrac{r_i}{r_0}\right)^2 y_0^{-1} & \text{if } y_0 < (r_i/r_0)\bar{y}_i \\ \infty & \text{otherwise.} \end{cases} \tag{2.31}$$

Plotting the allowed regions from the three constraints, along with the Eddington limits estimated from the bolometric luminosity reported in Borkar et al. (2021), we would able to constrain the joint distribution the the magnetic field and the electron number density at 100μas, which translates to 660 R_g for Cen A, as in Figure 2.17 and Figure 2.18. The values for allowed magnetic field is between 40 and 80 G, and the allowed number density for electron is between 1.5×10^4 and $4.5\times10^4\mathrm{cm}^{-3}$

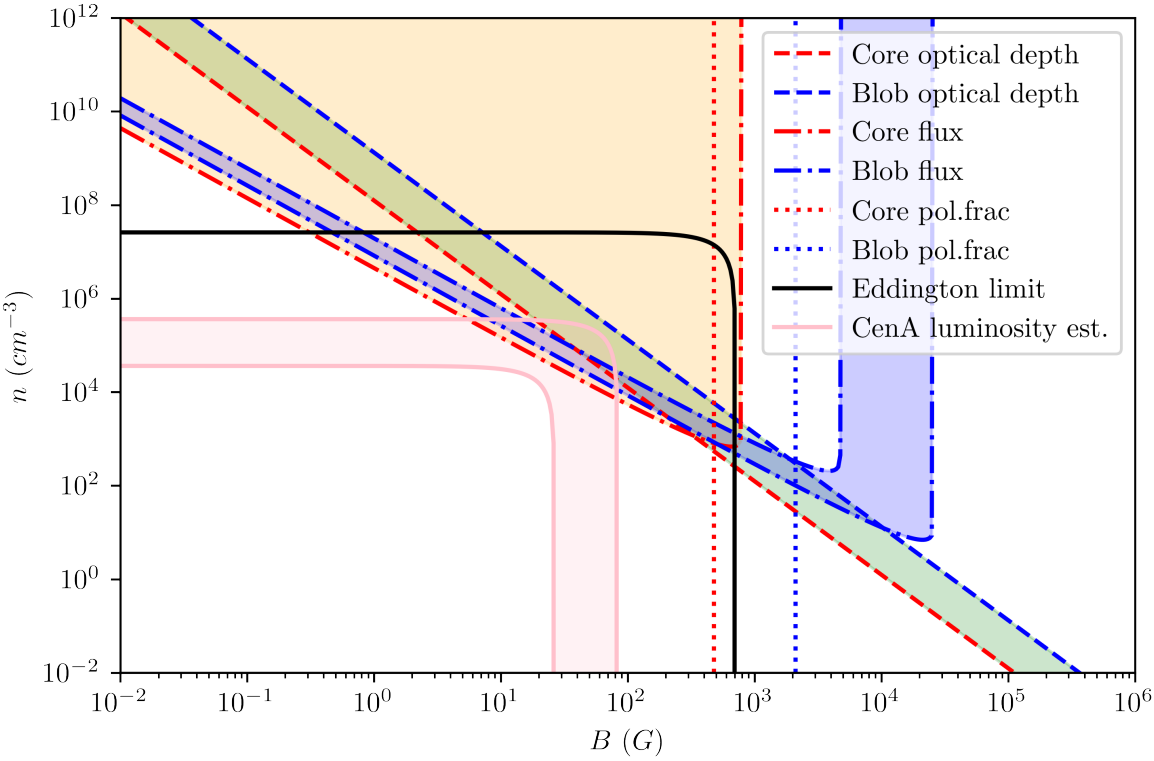

Figure 2.17: The model constraints assuming a Blandford-Konigl jet model. The red and blue dashed lines represent the constraint of optically thick and optically thin emission regions, in between which the green band is the allowed region. The red and blue dotted lines represent the upper limits from the polarization fraction in the core and the extended emission. The blue solid lines and the blue region are the allowed region based on the flux from the extended emission, while the orange solid lines and the orange region are the allowed region based on the flux from the core emission. The black lines are the referenced values from the Eddington limits, where the horizontal line is primarily from the kinetics estimate and the vertical line from the magnetic energy estimate. Similarly, the pink band is the estimate based on the bolometric luminosity of Cen A, reported in Borkar et al. (2021).

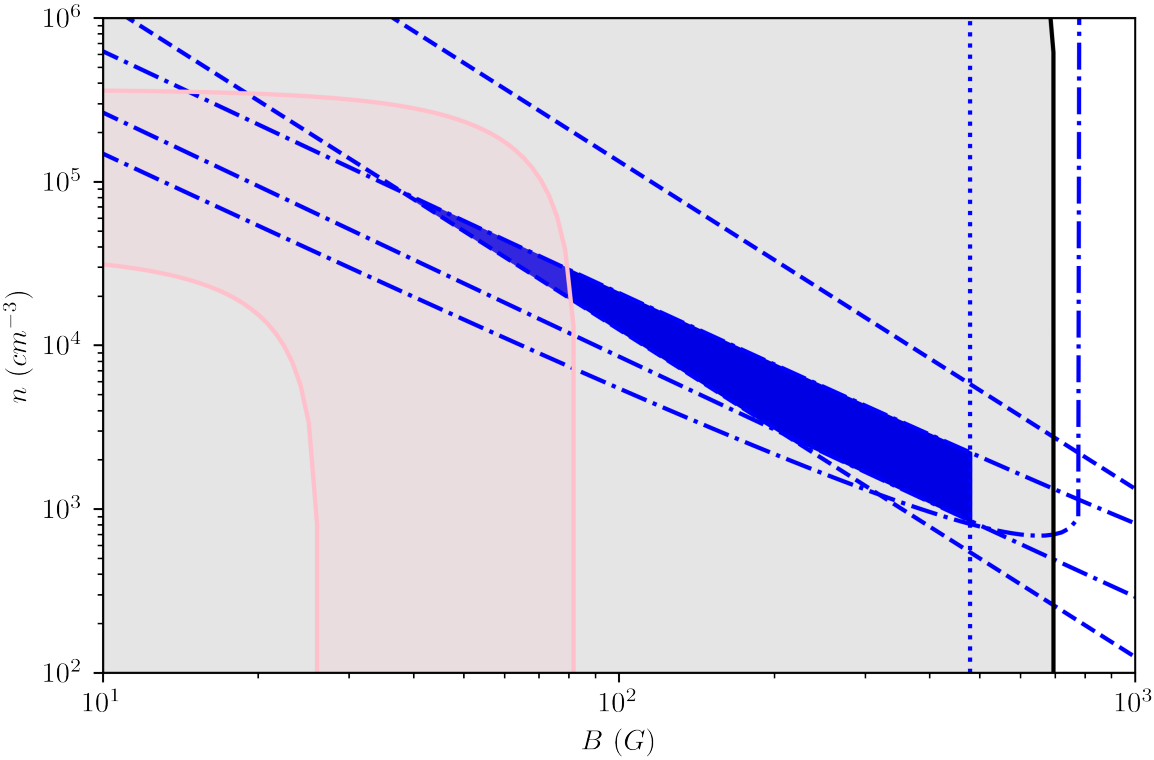

Figure 2.18: The zoomed-in version of the allowed region from Figure 2.17. The allowed region from constraints of the image is marked with blue, and the pink and black bands represent limits from the Bolometric luminosity and the Eddington limit.

Observables	Core	Blob
Observational frequency	229.1 GHz	-
Spectral index	-0.2	-
Distance to Earth	3.8 Mpc	-
Black Hole Mass	$5.5 \times 10^7 M_\odot$	-
Jet opening angle	9°	-
r_0	r_A	-
Distance to the apex	100μas	220μas
Solid angle	$1930\mu\text{as}^2$	$2700\mu\text{as}^2$
Flux mean	1.37 Jy	0.54 Jy
Flux std	0.05 Jy	0.04 Jy
Pol. frac. mean	0.3%	0.6%
Pol. frac. std	0.16%	0.37%

Table 2.2: All the values that are either read directly off the MCMC chain, or reported values associated with Cen A. The dash in the table means the value is the same for both the core and the blob.

2.6.5 Jet Velocity and Inclination Angle

In AGN, the Lorentz factor and the inclination angle are crucial in determining the jet-counterjet brightness ratio due to relativistic beaming effects and Doppler effect.

Lorentz factor is a measure of the relativistic effects experienced by an object moving at a significant fraction of the speed of light. It's defined as

$$\Gamma = \frac{1}{\sqrt{1 - (v^2/c^2)}}, \tag{2.32}$$

where v is the velocity of the jet and c is the speed of light. The Lorentz factor plays a critical role in the beaming of radiation from the jet, making the jet moving towards us appear much brighter than it intrinsically is. This effect increases with the Lorentz factor.

The inclination angle is the angle between the line of sight of the observer and the direction of the jet. A smaller inclination angle means the jet is pointed more directly towards the observer. The brightness of the jet is significantly enhanced when it is aligned close to our line of sight, due to the relativistic Doppler boosting.

The jet-counterjet brightness ratio (R) in AGN can be expressed in terms of the Lorentz

factor, Γ, and the inclination angle, θ, using the formula:

$$R = \left(\frac{1 + \beta \cos \theta}{1 - \beta \cos \theta} \right)^{2-\alpha}, \tag{2.33}$$

where $\beta = v/c$ is the jet speed as a fraction of the speed of light, and α is the spectral index of the jet emission (typically ranging from 0 for flat spectrum sources to 1 for steep spectrum sources). This formula encapsulates the effects of relativistic beaming, where the forward jet (pointing towards us) is significantly brighter than the counterjet (pointing away from us) due to the combination of the Lorentz factor and the inclination angle.

In combination, a higher Lorentz factor and a smaller inclination angle will result in a higher jet-counterjet brightness ratio due to the increased effects of relativistic beaming. This leads to situations where, in some AGN, the counterjet is almost or entirely invisible, while the jet pointed towards us is highly bright and easily observable.

For Cen A, as the posterior distribution from the total intensity construction gives an estimate on the luminosity for the jet and counterjet, we are able to constrain the values for the inclination angle and the Lorentz factor. As in Goddi et al. (2021), Cen A has a flat spectrum at submillimeter wavelength; thus, we take the value of $\alpha = 0$. Stacking measurements of the brightest point in the jet and in the counterjet, we are able to calculate its mean and standard deviation. In Figure 2.19, we plot the calculated jet velocity, β, against the inclination angle, utilizing our measurements of the jet-counterjet brightness ratio. On top, we also show the 1σ band from the standard deviation of the brightness measurement. To make a comparison, the reported inclination range (12 to 45 degrees) is shown as the green band, while the yellow band is the jet velocity range of $0.24c$ to $0.37c$, reported in Tingay et al. (1998); Hardcastle et al. (2003); Müller et al. (2014)

2.7 Conclusion

This chapter has focused on an in-depth analysis of the EHT 2017 observations of Cen A, one of the closest radio-loud galaxies. Our study utilizes the EHT data of Cen A to construct the total intensity and first linear polarization mapping of Cen A, overcoming several challenges in the dataset. Using the high-resolution polarization image of Cen A, we dissect the complex jet dynamics and magnetic field interactions within this significant astronomical object.

First, the data from the EHT's observations have allowed us to construct detailed models of the jet and counter-jet emitted by the supermassive black hole at the center

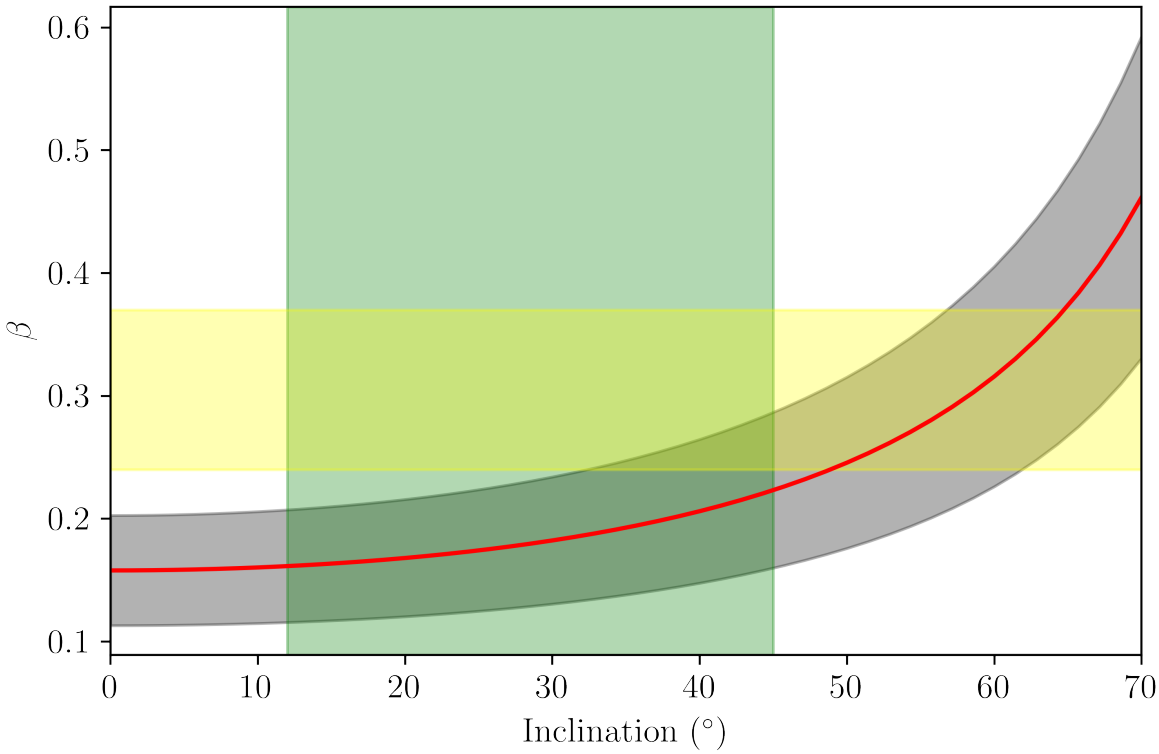

Figure 2.19: The joint plot for the jet velocity and the inclination angle, constrained by the jet/counterjet brightness ratio. The gray band around the red line is the 1σ range. The green band is the reported range for inclination angle from centimeter observations (Hardcastle et al., 2003). The yellow band is the reported range in the jet velocity. (Müller et al., 2014).

of Centaurus A, for both the total intensity and linear polarization structures. Through Bayesian imaging and analysis, we have identified key features in the jet emission regions, which we compare with the previous publication with the same dataset.

Further, our polarization analysis reveals weak but highly structured linear polarization patterns in the Cen A jets, indicating Cen A as a weak but polarized AGN. These linear polarization structures, segmented into different regions based on its emission profile, constrain the magnetic field strength and the electron number density in the jet, which the polarization is produced through synchrotron emissions.

The implications of this research extend beyond just an improved understanding of Centaurus A. They contribute significantly to the broader field of AGN physics, offering insights into the general mechanisms that may be at play in other similar galaxies. The methodologies developed here overcome a very challenging dataset and successfully extract weak polarized information, which sets a precedent for future dataset, where better quality is expected.

In summary, this chapter not only advances our knowledge of Centaurus A but also enhances our theoretical and observational frameworks for studying jet dynamics in AGNs. It sets the stage for subsequent observational strategies and theoretical models that can further elucidate the intricate relationships between supermassive black holes, their jets, and the cosmic environment.

Chapter 3

Probing Accretion Turbulence in the Galactic Center with EHT Polarimetry

3.1 Introduction

Black holes have been implicated as the engines of active galactic nuclei (AGN) and X-ray binaries. Within these objects, both their extreme luminosities and growth rate are presumably due to the interaction with the accretion of nearby matter. This occurs via accretion disks, through which material orbits, cools and falls inward toward the central object. Accretion flows are generic features in astronomical systems, from the formation of planets to the powering of AGN, and thus understanding the processes by which they operate informs astrophysics broadly.

The supermassive black hole at the Galactic Center, Sagittarius A* (Sgr A*), offers us a laboratory in which to study accretion flows in detail. Located 8 kpc from the Earth, with a mass of $4.3 \times 10^6\ M_\odot$ (Boehle et al., 2016; Gillessen et al., 2009; Gravity Collaboration et al., 2018), Sgr A* has now been resolved on event horizon scales with the Event Horizon Telescope (EHT Event Horizon Telescope Collaboration et al., 2022a,d,b,c,e,f). These observations present an unprecedented opportunity to probe the nature and characteristics of the hot plasma orbiting Sgr A* under the extreme conditions near the horizon.

The EHT is a global array of millimeter and sub-millimeter telescopes that achieves resolutions of 20 μas at a wavelength of 1.3 mm (230 GHz) via very-long baseline interferometry (VLBI). This resolution is sufficient to resolve the event horizons of Sgr A* and

M87*, silhouetted against the emission from the surrounding hot plasma. In comparison, the typical angular size of the shadow for Sgr A* and M87 is around 50μas. Therefore, it has now become possible to probe accretion physics on scales comparable to those relevant for MHD turbulence.

Four observing campaigns have been completed by the EHT, in April 2017, 2018, 2021 and 2022, and the first M87 and Sgr A* EHT results have been published (Event Horizon Telescope Collaboration et al., 2019d,e,f,g,h,i, 2022a,d,b,c,e,f). The full complement of Stokes parameters were measured at 230 GHz. Future development of the array will include the ability to observe at 345 GHz.

Sgr A* presents a natural target for studies of the role played by MHD turbulence in black hole accretion because of its short timescale and lack of an obvious relativistic jet. However, interpreting the small-scale brightness fluctuations, presumably associated with MHD turbulence within the accretion flow, is complicated by the interstellar scattering observed toward the Galactic center (Lo et al., 1998; Frail et al., 1994; Lazio & Cordes, 1998a). This scattering is believed to be a result of variations in the electron density along the line of sight (Goldreich & Sridhar, 1995; Lazio & Cordes, 1998b; Cordes & Lazio, 2002; Rickett, 1990). Typically, the origin of the scattering is abstracted to a thin scattering screen, for which detailed models exist (Psaltis et al., 2018; Johnson et al., 2018; Issaoun et al., 2021; Cho et al., 2021). For Sgr A*, two aspects of the scattering are of interest, corresponding to different regimes: diffractive and refractive scattering (Narayan, 1992; Johnson & Gwinn, 2015).

The diffractive scattering is the consequence of the combined effect of small-scale fluctuations in the interstellar electron density, whose impact is to blur the image with a nearly-Gaussian kernel (Johnson & Narayan, 2016; Issaoun et al., 2021). This angular broadening is formally reversible, i.e., images of Sgr A* may be effectively "deblurred" by applying the appropriate multiplicative correction in the Fourier (visibility) domain (Fish et al., 2014; Lu et al., 2018; Johnson et al., 2015b).

The impact of refractive scattering is more subtle. Associated with the large-scale fluctuations of the interstellar electron density, refraction induces coherent and variable substructures in the image (Johnson et al., 2018). These additional variations in the image are extrinsic to the source, and indicative of the interstellar scattering screen. Unlike diffractive scattering, it is not formally invertible, and may not be simply removed during image generation. In principle, it may be modeled, leveraging the modestly different timescales between the refractively induced extrinsic substructure and the intrinsic brightness fluctuations induced by MHD turbulence.

In this chapter, we demonstrate that the action of the scattering screen is expected to be

independent of polarization. Based on this, we develop a new scattering mitigation scheme that exploits this non-birefringence of the scattering screen. We demonstrate that for the angular scales accessible to the EHT and ngEHT, it is possible to effectively eliminate the impact of interstellar scattering on the estimators of the intrinsic structural polarimetric fluctuations, and thus probe MHD turbulence intrinsic to the near-horizon emission region directly. Although a complete spatiotemporal characterization of the turbulence is highly desirable (see, e.g., Georgiev et al., 2022), we focus on mitigating the spatial distortions resulting from scattering here, leaving the construction of the temporal component of the power spectrum for future work.

In Section 3.2 we review scattering in the thin-screen approximation, assess the impact on polarized emission, and demonstrate that scattering can be implemented as a non-birefringent tensor convolution that may be inverted. In Section 3.3, we construct toy models that mimic the gross properties of Sgr A*, and test the feasibility of scattering mitigation. In Section 3.4, we apply our scheme to a representative simulation from the existing EHT general relativistic magnetohydrodynamic (GRMHD) simulation library, and confirm we are able to extract intrinsic information about the structural variability in spite of the intervening scattering. Finally, we conclude in Section 3.5.

3.2 Scattering and Observation of Polarized Light

We begin with a summary of the action of an intervening scattering screen upon the emission from a compact source observed via a local interferometer. This is appropriate, e.g., for observations of Sgr A* by the EHT and ngEHT. We will follow presentation of Johnson & Gwinn (2015) where possible and refer the reader there for a detailed description.

3.2.1 Scattering and the Visibility Function

The primary observable quantity in interferometric radio observations, like those made by the EHT and ngEHT, is the "visibility", $V(\mathbf{b})$, constructed by cross-correlating signals at antennae separated by a projected baseline $\mathbf{b}$. This quantity is directly given by the Fourier transform of the intensity map, i.e.

$$V(\mathbf{b}) = \int d^2\mathbf{x} e^{2\pi i \mathbf{b}\cdot\mathbf{x}/\lambda} I(\mathbf{x}), \tag{3.1}$$

where $I(\mathbf{x})$ is the intensity map projected at the source distance, $\mathbf{x}$ is an angular location on the sky, and λ is the observing wavelength (see, e.g., Thompson et al., 2001). As a consequence, the $V(\mathbf{b})$ encodes the degree of source structure on an angular scale of $\lambda/|\mathbf{b}|$, oriented along the direction of $\mathbf{b}$.

Scattering is frequently modeled in the thin-screen approximation (Bower et al., 2014). The physical picture is presented in Figure 3.1, which shows the relative position of the emitting source, an intervening thin screen, and the observer on Earth. Thick scattering screens include additional complication, and may be required toward Sgr A* (for example, see Pen & Levin (2014)). Nevertheless, in many cases, these extended scattering regions may be abstracted to a sequence of thin screens. Thus, we will focus on the latter.

The impact of scattering in the thin-screen limit, is to impart a random phase shift at the screen, $\phi(\mathbf{x})$. That is, the observed visibilities are

$$\begin{aligned} V_{\rm obs}(\mathbf{b}) = \frac{1}{4\pi^2 r_F^4} \int d^2\mathbf{x}_1 d^2\mathbf{x}_2 \\ \times\, e^{i\left[\left(\mathbf{x}_1^2 - \mathbf{x}_2^2\right) + \mathbf{b}/(1+M)(\mathbf{b}_1+\mathbf{x}_2)\right]/\left(2r_F^2\right)} \\ \times\, e^{i[\phi(\mathbf{x}_1)-\phi(\mathbf{x}_2)]} V_{\rm int}\left[(1+M)\left(\mathbf{x}_2 - \mathbf{x}_1\right)\right]. \end{aligned} \tag{3.2}$$

where the Fresnel radius,

$$r_F = \sqrt{\frac{DR}{D+R}\frac{\lambda}{2\pi}} \tag{3.3}$$

is the characteristic radius at the observer on which the spherical nature of the approaching radio wave become important, and provides a useful scale for scattering phenomena. In Equation 3.2, we have introduced $V_{\rm obs}(\mathbf{b})$ for the visibility that is observed after scattering and $V_{\rm int}(\mathbf{b})$ for the visibility that would have been observed in the absence of scattering. It is, fundamentally, $V_{\rm int}(\mathbf{b})$ that is of interest to studies of the compact astronomical sources.

In the ensemble average regime, obtained after averaging $V_{\rm obs}(\mathbf{b})$ over many realizations of the scattering screen, the observed visibility is given by

$$\left\langle V_{\rm obs}(\mathbf{b})\right\rangle_{\rm ea} = e^{-D_\phi(\mathbf{b})} \left\langle V_{\rm int}[(1+M)\mathbf{b}]\right\rangle_{\rm ea} \tag{3.4}$$

where $\langle \ldots \rangle_{\rm ea}$ denotes ensemble averaging (Johnson & Gwinn, 2015). The $D_\phi(\mathbf{b})$ is the structure function of the phase fluctuations on the scattering screen, defined in the normal way:

$$D_\phi(\mathbf{b}) = \left\langle [\phi(\mathbf{x}+\mathbf{b}) - \phi(\mathbf{x})]^2 \right\rangle_{ea} \tag{3.5}$$

where for a statistically isotropic screen, like that we assume here, the absolute position $\mathbf{x}$ does not matter. Equation 3.4 is the well-known diffractive limit, in which scattering

imparts only a multiplicative correction to the appropriately averaged intrinsic visibilities, and in which images may be deblurred in the normal sense (Johnson & Gwinn, 2015).

Analogous observable quantities can be constructed for polarized emission, and we do so for the Stokes maps, $S(\mathbf{x}) = [I(\mathbf{x}), Q(\mathbf{x}), U(\mathbf{x}), V(\mathbf{x})]$, where here Stokes V refers to the excess right-handed circular polarization, not the visibility[1]. In general, the phase shifts may depend on the particular polarization under consideration. In practice, for credible values of the magnetic field strength in the interstellar medium, the scattering screen is non-birefringent.

3.2.2 (Non-)Birefringence of Scattering in the ISM

The degree to which we may assume that an intervening scattering screen is non-birefringent depends on the magnitudes of two closely related quantities, the angular deflections experienced by radio waves passing through the screen (refraction), and the phase shifts imparted on those radio waves during their passage (dispersion). Here, we show that for models of interstellar scattering in which both are due to turbulent fluctuations in the magnetized interstellar plasma, both are sufficiently small that we may treat scattering as independent of the polarization of the radio waves under consideration. We will begin by analyzing the properties of the scattering in the unmagnetized limit, and thus produce estimates for the unpolarized case, followed by an analysis of a weakly magnetized screen to estimate the disparate impact on different radio wave polarizations. Before starting, we define the following dimensional variables, X and Y, following the conventions in plasma physics,

$$X \equiv \omega_P^2/\omega^2, \tag{3.6}$$

$$Y \equiv \mathrm{sgn}(\mathbf{B}\cdot\mathbf{z})\omega_B/\omega, \tag{3.7}$$

where $\omega_P = (4\pi n_e e^2/m_e)^{1/2}$ is the plasma frequency, n_e is the free electron density, e the electron charge, and m_e the electron mass, $\omega_B = eB/m_e c$ is the cyclotron frequency, and $\mathbf{z}$ is the line-of-sight direction. X and Y are proportional to the plasma density and the magnetic field strength at given frequency, ω.

Detailed computations for screens composed of turbulent magnetized plasmas reach similar conclusions and are presented in Section B.1.

[1]Henceforth, we will use superscripts to indicate Stokes parameters to avoid confusion.

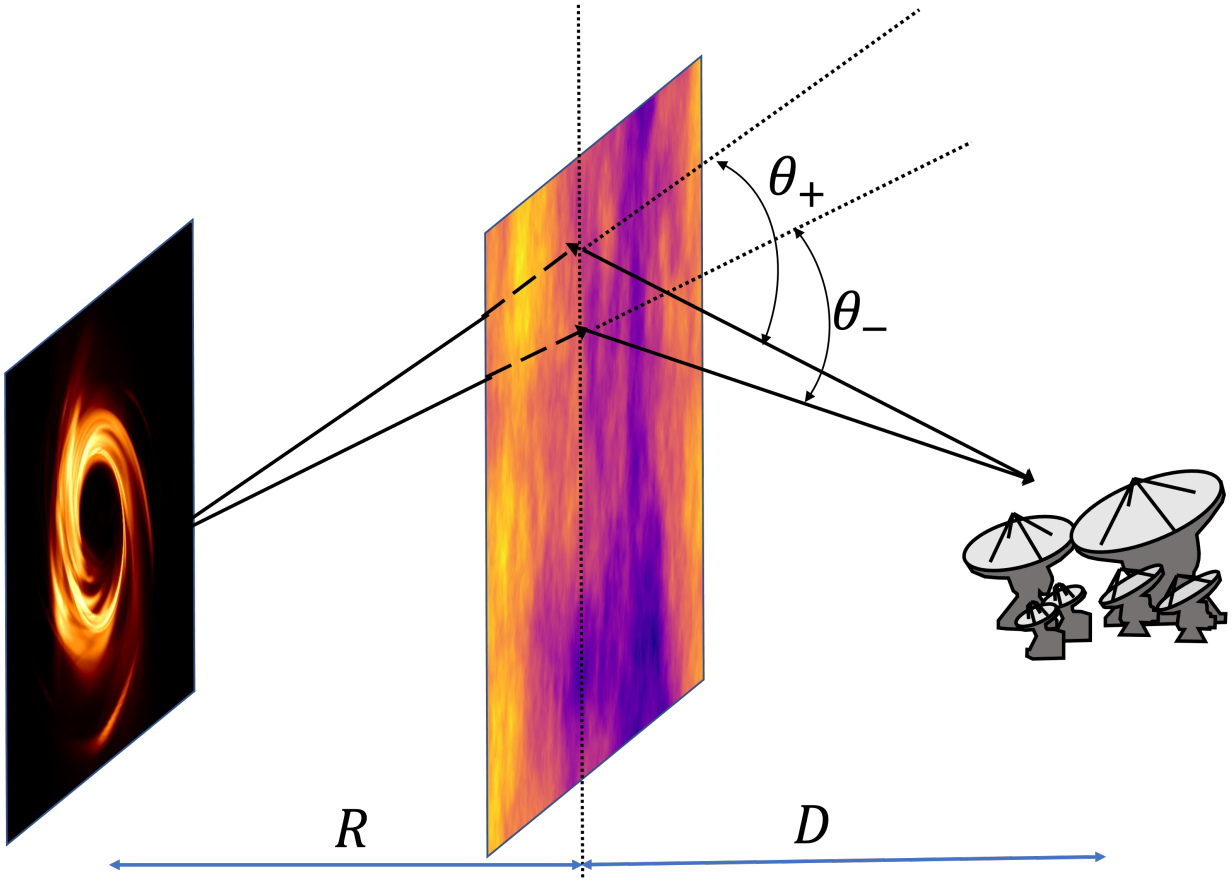

Figure 3.1: Schematic illustration of the interstellar scattering at a thin screen that imparts random phase fluctuations. The paths of two rays, differing in polarization, are shown, indicating the slight difference in the refractive deflection angles $\theta_{\pm}$. The source-screen (R) and screen-observer (D) distances are indicated.

Refraction in an Unmagnetized Screen

In the absence of a magnetic field, the long-wavelength dispersion relation for electromagnetic waves in an electron-ion plasma is,

$$\omega^2 = k^2 c^2 + \omega_P^2, \tag{3.8}$$

The associated equations of motion for radio wave are then given by Hamilton's equations obtained by setting $H(\mathbf{x}, \mathbf{k}) = \hbar\omega(\mathbf{x}, \mathbf{k})$,

$$\dot{\mathbf{k}} = -\vec{\nabla}\omega\left(\mathbf{k}, \mathbf{x}\right) = -\frac{\omega_P^2}{2\omega}\vec{\nabla}\ln n_e, \tag{3.9}$$

where $\mathbf{k}$ is the wave vector and related to the photon momentum by $\mathbf{p} = \hbar\mathbf{k}$. This equation of motion describes how electromagnetic waves refract when traveling through the scattering screen. In the weak-deflection limit, the perpendicular momentum gained after propagating through the scattering screen is,

$$k_{\mathbf{r}} = \int dz \frac{dk_{\mathbf{r}}}{dz} = -\int dz \frac{\omega_P^2}{2\omega c}\nabla_{\mathbf{r}} \ln n_e, \tag{3.10}$$

where we have made use of the approximation that the line-of-site velocity of the wave is c. Thus, the deflection angle is approximately the ratio between $k_{\mathbf{r}}$ and k_z,

$$\theta_0 = -\int dz \frac{\omega_P^2}{2\omega^2}\nabla_{\mathbf{r}} \ln n_e = -\frac{1}{2}\int dz \nabla_r X, \tag{3.11}$$

where we used that $k_z \approx \omega/c$.

The typical size of scattered compact sources, broadened by the diffractive scattering, places a constraint on the magnitude of $\theta_0 \approx \theta_{\rm diff}$, and therefore, the line-of-sight integrated transverse gradients of the fluctuating electron density within the screen. It is against this value that we will normalize the impact of non-zero magnetic fields, and thus the degree of birefringence for a weakly magnetized scattering screen.

Refraction in a Weakly Magnetized Screen

In the presence of a weak magnetic field, the dispersion relation of electromagnetic waves traveling through a plasma is slightly modified, becoming

$$\omega^2 = k^2 c^2 + \omega_P^2 \left(1 \pm \frac{\omega_B}{\omega}\right), \tag{3.12}$$

where there are now two propagating modes, ordinary and extraordinary, signified by the $\pm$ sign. In the quasi-transverse limit (propagation along the magnetic field), the two polarization modes are nearly circular.

We again obtain the equations of motion from Hamilton's equations, though in this instance they differ for the two polarization modes,

$$\dot{\mathbf{k}_{\pm}} = -\vec{\nabla}\omega\left(\mathbf{k},\mathbf{x}\right) = -\frac{1}{2\omega}\vec{\nabla}\left(\omega_P^2 \pm \frac{\omega_B}{\omega}\omega_P^2\right). \tag{3.13}$$

The deflection angle after integration through the screen is, therefore,

$$\theta_{\pm} = -\frac{1}{2}\int dz X\left(1 \pm Y\right)\nabla_{\mathbf{r}} \ln\left[n_e\left(1 \pm Y\right)\right], \tag{3.14}$$

where we have defined Y previously.

The mean deflection of the two modes is just that associated with the unmagnetized plasma

$$\bar{\theta} = \frac{\theta_+ + \theta_-}{2} = \theta_0. \tag{3.15}$$

The differential deflection, and thus the disparity in the impact of the weakly magnetized scattering screen on the two polarizations, is given by

$$\delta\theta = \theta_+ - \theta_- = -\int dz \nabla_{\mathbf{r}}\left(XY\right). \tag{3.16}$$

Upon averaging over a random magnetic field orientation, and thus sign of Y, this would vanish. However, the variance of $\delta\theta$, and thus its typical value, does not vanish,

$$\langle\delta\theta^2\rangle \approx \langle\bar{\theta}^2\rangle\langle Y^2\rangle > \approx \theta_{\rm diff}^2\sigma_Y^2, \tag{3.17}$$

where $\sigma_Y^2 \sim Y^2$ is the variance in Y, associated with the magnitude of the magnetic field fluctuations. Thus, typically, the difference in the deflection of the two polarization modes, is reduced by a factor of Y^2, which at 1.3 mm is small for credible interstellar magnetic field strengths ($\lesssim 1$ mG)

Phase Shift Induced by a Weakly Magnetized Screen

The typical phase fluctuations imparted by the scattering screen are related to, but distinct from, the refraction. Given the dispersion relation in Equation 3.12, the phase shift for the transverse electromagnetic modes grow as,

$$\phi_{\pm} = \int k dz \approx \frac{\omega}{c}\int dz\left(1 - \frac{1}{2}X \pm \frac{1}{2}XY\right), \tag{3.18}$$

and thus the difference between the phases of the the polarization modes is,

$$\delta\phi = \frac{\omega}{c}\int dz XY. \tag{3.19}$$

This expression suggests that the differentially accumulated phase and typical differential deflection angle differs by a factor of L/λ, where L is the typical correlation length within the plasma. This suspicion is born out by detailed calculations for a variety of magnetic field and electron density fluctuation spectra presented in Section B.1. Similar results are presented in the past literature (e.g. see Macquart & Melrose (2000)).

In particular, for power-law electron fluctuation spectra, we show that L may be associated with the inner scale, $r_{\rm in}$, in Psaltis et al. (2018) and Johnson et al. (2018). Therefore, the typical differential deflections may be related to the typical differential phase fluctuations induced by a thin scattering screen by,

$$\langle\delta\phi^2\rangle \approx \frac{r_{\rm in}^2}{\lambda^2}\langle\delta\theta^2\rangle. \tag{3.20}$$

Given a typical value for $\theta_{\rm diff} \approx 10$ μas, an interstellar magnetic field of 1 μG, and an inner scale within the Galactic center scattering screen of $r_{\rm in} \approx 800$ km (Johnson et al., 2018; Issaoun et al., 2021), we estimate that the root-mean-square phase difference between different polarization modes at 1.3 mm is of order

$$\sqrt{\langle\delta\phi^2\rangle} \approx 10^{-12}\left(\frac{B}{1\mu{\rm G}}\right)\left(\frac{r_{\rm in}}{800\ {\rm km}}\right)\ {\rm rad}. \tag{3.21}$$

Note that the wavelength dependence of $\sqrt{\langle\delta\phi^2\rangle}$ is now nominally dropped. But the implicit dependence of the wavelength is within $\theta_{\rm diff}$, which is the typical value at 230GHz. As a result, for the purposes of the EHT, we may safely assume that the Galactic center scattering screen is non-birefringent.

3.2.3 Characterizing Turbulent Substructure in Images

In this paper we are primarily interested in the measurement and characterization of the statistical properties of small-scale fluctuations in the underlying image of Sgr A*, presumably arising due to turbulent structures in the accretion and/or jet launching region. Typically, these are expressed in terms of power spectra, which measure the degree of fluctuations on each spatial scale.

As the Fourier transform of the sky brightness map, the $V(\mathbf{b})$ already directly contain a measure of the degree of structure on various spatial scales. Therefore, it is natural to construct statistical measures of the variability on different spatial scales from the $V(\mathbf{b})$. For reasons that will become clear in following sections, we choose to do this with the full visibilities, and characterize the spatial power spectrum of image fluctuations via,

$$P^S(\mathbf{b}) = \left\langle |V^S(\mathbf{b})|^2 \right\rangle_{\rm turb}, \tag{3.22}$$

where the superscript S indicates which Stokes parameter is used to construct the visibilities, and $\langle \ldots \rangle_{\rm turb}$ indicates averages over timescales long in comparison to the turbulent timescales in the source on the spatial scales of interest (typically many hours or longer). We will presume henceforth that all time averages will include both turbulent averages and ensemble averages, i.e., independent averages over realizations of the stochastic source structure and the intervening scattering screen, dropping the specifier in what follows.

Note that this does not subtract the mean $V(\mathbf{b})$, and therefore contains contributions from the variable and static components of the image. Nevertheless, we will find that this is the more convenient power spectrum for scattering mitigation. It is also defined consistently with the power spectral densities in Georgiev et al. (2022).

Impact of Scattering on the Power Spectrum

After scattering via a thin screen, as described in Section 3.2.1, the power spectrum is modified. The resulting expression may be found in Eq. 32 of Johnson & Gwinn (2015), which reads

$$\begin{aligned} P^S_{\rm obs}(\mathbf{b}) = e^{-D_\phi[\mathbf{b}/(1+M)]} P^S_{\rm int}(-\mathbf{b}) \\ - \frac{1}{(2\pi r_F^2)^2} \frac{1}{2 r_F^4} \int d^2\mathbf{y} \left[\mathbf{y} \cdot \left(\mathbf{y} + \frac{\mathbf{b}}{1+M} \right) \right]^2 \\ \times \tilde{D}_\phi \left(\mathbf{y} + \frac{\mathbf{b}}{1+M} \right) e^{-D_\phi(\mathbf{y})} P^S_{\rm int}[(1+M)\mathbf{y}], \end{aligned} \tag{3.23}$$

where

$$\tilde{D}_\phi(\mathbf{y}) = \int d^2\mathbf{x}\, e^{i\mathbf{y}\cdot\mathbf{x}/r_F^2} D_\phi(\mathbf{y}) \tag{3.24}$$

is the Fourier transform of the structure function.

Hidden within Equation 3.23 is a convolution that, like for diffractive scattering, expresses the impact of refractive scattering as a linear operator, defined by the tensor convolution kernel,

$$\mathbf{K}(\mathbf{y}) = -\frac{\mathbf{y}\tilde{D}_\phi[\mathbf{y}/(1+M)]\mathbf{y}^T}{8\pi^2 r_F^8 (1+M)^6}. \tag{3.25}$$

Expressing Equation 3.23 in terms of $\mathbf{K}(\mathbf{y})$, we obtain,

$$P^S_{\rm obs}(\mathbf{b}) = e^{-D_\phi[\mathbf{b}/(1+M)]} P^S_{\rm int}(-\mathbf{b}) \int d^2\mathbf{y} \sum_{ij} \mathbf{K}\left(\mathbf{y}+\mathbf{b}\right)_{ij} \left[\mathbf{y} e^{-D_\phi[\mathbf{y}/(1+M)]} P^S_{\rm int}(\mathbf{y})\mathbf{y}^T\right]_{ji}, \tag{3.26}$$

where both indices of $\mathbf{K}(\mathbf{y})$ are summed over. Equation 3.26 is equivalent to Eq. 16 of Johnson & Narayan (2016) after identifying $\tilde{D}_\phi$ with their Q, up to appropriate scaling. Within Equation 3.26, the impact of diffractive and refractive scattering are clearly delineated by the first and second terms, respectively.

Characteristic scales for $\mathbf{K}(\mathbf{y})$

The typical scales for $\mathbf{K}(\mathbf{y})$ may be inferred from its definition and the approximate limiting expressions for $D_\phi(\mathbf{x})$, and thus $\tilde{D}_\phi(\mathbf{y})$. On very small scales, $D_\phi(\mathbf{x})$ is generically quadratic, smoothly vanishing at $\mathbf{x} = 0$. Assuming isotropy of the phase screen, on very large scales, $D_\phi(\mathbf{x})$ is a power law fixed by the nature of the turbulence within the ISM that gives rise to the scattering screen. Therefore, following Johnson & Gwinn (2015), we express $D_\phi(\mathbf{x})$ in terms of these two regimes, separated by a spatial scale within the scattering screen, r_0, which we will assume is much smaller than the scale at which the ISM turbulence is damped, the "inner scale", $r_{\rm in}$:

$$D_\phi(\mathbf{x}) = \begin{cases} \left(\dfrac{|\mathbf{x}|}{r_0}\right)^2 & |\mathbf{x}| \ll r_{\rm in} \\ \dfrac{2}{\alpha_{\rm sc}} \left(\dfrac{r_{\rm in}}{r_0}\right)^{2-\alpha_{\rm sc}} \left(\dfrac{|\mathbf{x}|}{r_0}\right)^{\alpha_{\rm sc}} & |\mathbf{x}| \gg r_{\rm in}. \end{cases} \tag{3.27}$$

Typically, the longest baselines accessible to the EHT array are well into the power-law regime, assuming the inner scale of 800km.

In this case, the above expressions simplify to

$$D_\phi(\mathbf{x}) \approx \left(\frac{|\mathbf{x}|}{r_{\rm diff}}\right)^{\alpha_{\rm sc}}, \tag{3.28}$$

where

$$r_{\rm diff} = r_{\rm in}\left(\frac{\alpha_{\rm sc}}{2}\right)^{1/\alpha_{\rm sc}}\left(\frac{r_0}{r_{\rm in}}\right)^{2/\alpha_{\rm sc}}. \tag{3.29}$$

The corresponding $\tilde{D}_\phi(\mathbf{y})$ is given in Eq. 34 of Johnson & Gwinn (2015),

$$\tilde{D}_\phi(\mathbf{y}) = 2^{2+\alpha_{\rm sc}}\pi\frac{\Gamma(1+\alpha_{\rm sc}/2)}{\Gamma(-\alpha_{\rm sc}/2)}r_{\rm diff}^2\left(\frac{r_{\rm diff}}{r_F}\frac{|\mathbf{y}|}{r_F}\right)^{-(\alpha_{\rm sc}+2)}. \tag{3.30}$$

The collection of constants in front of $r_{\rm diff}^2$ evaluate to -7.09 for $\alpha_{\rm sc} = 1.38$, appropriate for Sgr A* (Issaoun et al., 2021). Inserting this into Equation 3.25, the refractive scattering kernel is approximately

$$\mathbf{K}(\mathbf{y}) \approx -\frac{2^{\alpha_{\rm sc}-1}}{\pi}\frac{\Gamma(1+\alpha_{\rm sc}/2)}{\Gamma(-\alpha_{\rm sc}/2)}\frac{1}{r_F^4(1+M)^{4-\alpha_{\rm sc}}} \times \left(\frac{r_{\rm diff}}{r_F}\right)^{-\alpha_{\rm sc}}\frac{\mathbf{y}}{r_F}\left(\frac{|\mathbf{y}|}{r_F}\right)^{-(\alpha_{\rm sc}+2)}\frac{\mathbf{y}^T}{r_F}. \tag{3.31}$$

Approximate Inversion of Refractive Scattering

Equation 3.26 provides $P^S_{\rm obs}(\mathbf{b})$ in terms of a linear operation upon $P^S_{\rm int}(\mathbf{b})$. Because it is the latter that is of particular interest here, we need to invert this relation, giving $P^S_{\rm int}(\mathbf{b})$ in terms of $P^S_{\rm obs}(\mathbf{b})$. How to do this is discussed in detail in Section B.2. If the refractive term is small, this inversion can be constructed perturbatively, yielding to first order

$$P^S_{\rm int}(\mathbf{b}) = e^{D_\phi[\mathbf{b}/(1+M)]}\left\{P^S_{\rm obs}(\mathbf{b}) - \int d^2\mathbf{y}\sum_{ij}\mathbf{K}(\mathbf{y}+\mathbf{b})_{ij}\left[\mathbf{y}P^S_{\rm obs}(\mathbf{y})\mathbf{y}^T\right]_{ji}\right\}. \tag{3.32}$$

The accuracy of this approximation is dependent on the magnitude of $P^S_{\rm obs}(\mathbf{b})^{-1}\int d^2\mathbf{y}\sum_{ij}\mathbf{K}(\mathbf{y}+\mathbf{b})_{ij}\left[\mathbf{y}P^S_{\rm obs}(\mathbf{y})\mathbf{y}^T\right]_{ji}$, which must be small. This ratio is approximately the fraction of the observed power due to refractive scattering, which is what we are explicitly expanding in.

It also indicates the origin of the scattering-mitigation strategy pursued by combining multiple polarization modes. The idea is to minimize this ratio. It is now clear how this may be done. Very red or blue $P^S_{\rm obs}(\mathbf{b})$ will distribute power from large or small scales, respectively, throughout $P^S_{\rm int}(\mathbf{b})$. Therefore, suppressing strong variations with spatial frequency in $P^S_{\rm obs}(\mathbf{b})$ is primary way in which the choice of polarization mode can impact the fidelity of the $P^S_{\rm int}(\mathbf{b})$ reconstruction.

At the same time, it explicitly identifies that this approximation cannot be satisfied at all baseline lengths. At sufficiently long baselines, $P^S_{\rm obs}(\mathbf{b})$ is exponentially suppressed by

the diffractive scattering. As a result, the power distributed from short baselines by the convolution term will inevitably dominate. As a result, it is exponentially difficult to push toward longer baselines in the exponentially suppressed regime. If we define $\mathbf{b}_{\text{diff}}$ to be the shortest baseline for which $D_\phi[\mathbf{b}_{\text{diff}}/(1+M)] \approx 1$, then the perturbative expansion will be poorly justified for baseline lengths above $|\mathbf{b}_{\text{max}}|$, defined by

$$\sum_{ij} \mathbf{K}(\mathbf{b}_{\text{diff}} + \mathbf{b}_{\text{max}})_{ij} \left[\mathbf{b}_{\text{diff}} P^S_{\text{int}}(\mathbf{b}_{\text{diff}}) \mathbf{b}^T_{\text{diff}}\right]_{ji} |\mathbf{b}_{\text{diff}}|^2 \approx e^{-D_\phi[\mathbf{b}_{\text{max}}/(1+M)]} P^S_{\text{int}}(\mathbf{b}_{\text{max}}). \tag{3.33}$$

If we assume that at long baselines the intrinsic spatial power spectrum has a power-law fall off, i.e., $P^S_{\text{int}}(\mathbf{b}) \sim |\mathbf{b}|^{-\alpha}$, then with $D_\phi(\mathbf{b})$ and $\tilde{D}_\phi(\mathbf{y})$ given by Equation 3.28, Equation 3.30, and Equation 3.31

$$|\mathbf{K}(\mathbf{b}_{\text{max}})| \approx \frac{K_0}{64 r_F^4} \left(\frac{b_{\text{diff}}}{r_F}\right)^{-2\alpha_{\text{sc}}} \left(\frac{b_{\text{max}}}{b_{\text{diff}}}\right)^{-\alpha_{\text{sc}}}, \tag{3.34}$$

where K_0 encapsulates the α_{sc}-dependent coefficient preceding the factor of r_F^{-4} in Equation 3.31. Therefore, the condition that the refractive and diffractive contributions to P^S_{obs} are similar becomes,

$$\frac{K_0}{64} \left(\frac{b_{\text{diff}}}{r_F}\right)^{4-2\alpha_{\text{sc}}} \left(\frac{b_{\text{max}}}{b_{\text{diff}}}\right)^{\alpha-\alpha_{\text{sc}}} \approx e^{-[b_{\text{max}}/b_{\text{diff}}(1+M)]^{\alpha_{\text{sc}}}}, \tag{3.35}$$

and therefore, the maximum baseline length at which we may perturbatively invert Equation 3.26 to obtain P^S_{int} is

$$b_{\text{max}} \approx (1+M) b_{\text{diff}} \left[\ln\left(\frac{64}{K_0}\right) + (4-2\alpha_{\text{sc}}) \ln\left(\frac{r_F}{b_{\text{diff}}}\right)\right]^{1/\alpha_{\text{sc}}}, \tag{3.36}$$

where we have ignored a logarithmic term that scales as $(\alpha - \alpha_{\text{sc}}) \ln(b_{\text{max}}/b_{\text{diff}})$.[2]

For $\alpha_{\text{sc}} = 1.38$, $R = 2$ kpc and $D = 6$ kpc, $r_F \approx 10^5$ km, and $b_{\text{min}} \approx 3\ \text{G}\lambda$ (corresponding to the long-axis of the diffractive scattering kernel at 1.3 mm), this gives that $b_{\text{max}} \approx 3.4 b_{\text{diff}}(1+M) \approx 13.6\ \text{G}\lambda$.

Note that because b_{diff} grows as λ^{-2} and r_F grows as $\lambda^{1/2}$, b_{max} grows more rapidly than the maximum baseline as λ shrinks. For example, if λ decreases from 1.3 mm to 0.87 mm, b_{diff} grows by a factor of 2.2, while the remainder of the coefficient in Equation 3.36

[2]Explicitness including this term does not significantly change the approximate limit.

decreases to 3.1, and thus $b_{\max}$ increases to 32.8 Gλ. In comparison, the maximum Earth-bound baseline grows from 8.5 Gλ to 12.8 Gλ. Hence, at 0.87 mm, the linear approximation improves dramatically.

Henceforth, we will assume that we may utilize the first order inversion approximation in Equation 3.32 to recover $P^S_{\rm int}(\mathbf{b})$ from observations of $P^S_{\rm obs}(\mathbf{b})$.

3.2.4 Exploiting Polarization

The dominant impact of scattering on $P^S_{\rm int}(\mathbf{b})$ is the reduction of power at long baselines due to diffractive scattering. However, because the action of scattering is independent of the polarization of the observed radio wave, combinations of polarized power spectra may be constructed such that the diffractive suppression is canceled identically. That is, with Equation 3.32 applied to the power spectra measured for Stokes parameters S and S', we have

$$\frac{P^S_{\rm int}(\mathbf{b})}{P^{S'}_{\rm int}(\mathbf{b})} = \frac{P^S_{\rm obs}(\mathbf{b}) - \int d^2\mathbf{y} \sum_{ij} \mathbf{K}(\mathbf{y}+\mathbf{b})_{ij} [\mathbf{y} P^S_{\rm obs}(\mathbf{y}) \mathbf{y}^T]_{ji}}{P^{S'}_{\rm obs}(\mathbf{b}) - \int d^2\mathbf{y} \sum_{ij} \mathbf{K}(\mathbf{y}+\mathbf{b})_{ij} [\mathbf{y} P^{S'}_{\rm obs}(\mathbf{y}) \mathbf{y}^T]_{ji}}, \tag{3.37}$$

which is impacted only by refractive scattering. In this way, diffractive scattering can effectively be mitigated, even without an explicit model for the scattering process (i.e., a specific choice of $D_\phi(\mathbf{x})$).

The reconstruction of $P^S_{\rm int}(\mathbf{b})$ from $P^{S'}_{\rm obs}(\mathbf{b})$ in Equation 3.32 improves dramatically when $P^S_{\rm obs}(\mathbf{b})$ is small on short baselines, and therefore there is less refractive contamination at long baselines to the recovered intrinsic power spectrum. This is reflected by the smaller contributions from the convolution term in Equation 3.32. When this may be neglected, Equation 3.37 reduces to

$$\frac{P^S_{\rm int}(\mathbf{b})}{P^{S'}_{\rm int}(\mathbf{b})} \approx \frac{P^S_{\rm obs}(\mathbf{b})}{P^{S'}_{\rm obs}(\mathbf{b})}. \tag{3.38}$$

Given the measurement of the full Stokes maps, it is generally possible to construct specific polarization modes for which the assumptions underlying Equation 3.38 are satisfied.

Because the $P^S_{\rm obs}(\mathbf{b})$ are typically "red", it will suffice to select the polarization modes to preferentially suppress the short-baseline (large-scale) power. By doing so, the contamination of the estimated $P^S_{\rm int}(\mathbf{b})$ at long baselines (small scales) from the $P^S_{\rm obs}(\mathbf{b})$ at short baselines (large scales) can be nearly eliminated. That is, by minimizing the large scale power in the $P^S_{\rm int}(\mathbf{b})$, we are able to minimize the magnitude of the ratio of $P^S_{\rm obs}(\mathbf{b})^{-1} \int d^2\mathbf{y} \sum_{ij} \mathbf{K}(\mathbf{y}+\mathbf{b})_{ij} \left[\mathbf{y} P^S_{\rm obs}(\mathbf{y}) \mathbf{y}^T\right]_{ji}$ in Equation 3.37, rendering Equation 3.38 an excellent approximation at sufficiently long baselines.

We begin by constructing the Stokes vector, $\mathbf{S}_0$, associated with the time-averaged values of zero-baseline Stokes visibility maps Q, U, and V (corresponding the source-integrated polarization). This vector is shown in Figure 3.2 after projecting it onto the Poincare sphere. We construct two additional polarization modes, $\mathbf{S}_1$ and $\mathbf{S}_2$, chosen to be orthogonal to $\mathbf{S}_0$. As a direct result, $\langle \mathbf{S}_1 \rangle = \langle \mathbf{S}_2 \rangle = 0$ identically, and therefore $P^{S1}_{\rm obs}(0)$ and $P^{S2}_{\rm obs}(0)$ are generally small.

We choose to construct $\mathbf{S}_1$ from $\langle V^Q \rangle(0)$ and $\langle V^U \rangle(0)$, thereby ensuring that it corresponds to a linearly polarized mode. The resulting $\mathbf{S}_1$, after enforcing orthogonality with $\mathbf{S}_0$ is shown in Figure 3.2. The second polarization is then unique defined up to a sign by the requirement that $\mathbf{S}_2$ be orthogonal to both $\mathbf{S}_1$ and $\mathbf{S}_0$, as shown in Figure 3.2. Generally, $\mathbf{S}_2$ will be an elliptical polarization mode.

Explicitly, in terms of $\mathbf{S}_0 = (q_0, u_0, v_0)$, $\mathbf{S}_1$ and $\mathbf{S}_2$ can be expressed as

$$\mathbf{S}_1 = (q_1, u_1, 0) \quad \text{and} \quad \mathbf{S}_2 = (q_2, u_2, v_2)\,, \tag{3.39}$$

where q_1, u_1, q_2, u_2 and v_2 are the projected components of the Stokes vector onto Q, U and V axes:

$$\begin{aligned}
q_1 &= -u_0/\sqrt{q_0^2 + u_0^2} \\
u_1 &= q_0/\sqrt{q_0^2 + u_0^2} \\
q_2 &= -u_1 v_0/\sqrt{q_0^2 + u_0^2 + v_0^2} \\
u_2 &= q_1 v_0/\sqrt{q_0^2 + u_0^2 + v_0^2} \\
v_2 &= (q_1^2 + u_1^2)/\sqrt{q_0^2 + u_0^2 + v_0^2}
\end{aligned} \tag{3.40}$$

The power spectra for the two polarization modes can be written down as the linear combination of the power spectra associated with the polarization components Q, U and V, with the coefficients q_1, u_1, q_2, u_2 and v_2, i.e.,

$$\begin{aligned}
P^{\mathbf{S}_1} &= q_1^2 P^Q + u_1^2 P^U + q_1 u_1 \langle V^Q V^{U*} \rangle + u_1 q_1 \langle V^U V^{Q*} \rangle \\
P^{\mathbf{S}_2} &= q_2^2 P^Q + u_2^2 P^U + v_2^2 P^V \\
&\quad + q_2 u_2 \langle V^Q V^{U*} \rangle + u_2 q_2 \langle V^U V^{Q*} \rangle \\
&\quad + q_2 v_2 \langle V^Q V^{V*} \rangle + v_2 q_2 \langle V^V V^{Q*} \rangle \\
&\quad + u_2 v_2 \langle V^U V^{V*} \rangle + v_2 u_2 \langle V^V V^{U*} \rangle
\end{aligned} \tag{3.41}$$

The benefits of these two constructed polarization modes are two-fold. First, the Stokes vectors of $\mathbf{S}_1$ and $\mathbf{S}_2$ are perpendicular to S_0, so they both incorporate zero-mean value

property, which ensures minimal impact from scattering. First, the absence of a mean value for $\mathbf{S}_1$ and $\mathbf{S}_2$ renders Equation 3.38 an excellent approximation of the relationship between the observed and intrinsic power spectra. Second, they have a clear physical meaning.

Fluctuations in $\mathbf{S}_1$ correspond to variations in the observed electric vector position angle (EVPA), i.e., the orientation of the linear component of the polarization. For synchrotron sources, as Sgr A* is believed to be, this maps the projected orientation of the net magnetic field as measured on different spatial scales. Fluctuations in $\mathbf{S}_2$ correspond to variations in the observed ellipticity, i.e., the degree of circular polarization relative to that of the linear polarization. For synchrotron emission from ion-electron plasmas, again, anticipated to be the case in Sgr A*, this directly maps to the angle between the magnetic field and the line of sight. Therefore, these two polarization modes are intrinsically probing the stochastic variability in the three-dimensional magnetic field, integrated throughout the emission region.

MHD turbulence is expected to generate large variations in the plasma density, magnetic field strength, and magnetic field orientation. Thus, given global simulations of the emitting plasma, testable predictions for $P^{S1}_{\rm int}(\mathbf{b})$ and $P^{S2}_{\rm int}(\mathbf{b})$, and hence their ratio, may be generated. That is, not only is $P^{S1}_{\rm int}(\mathbf{b})/P^{S2}_{\rm int}(\mathbf{b})$ technically easier to measure, but it is precisely the quantity that is expected to provide direct insight into the astrophysical processes within the source.

3.2.5 Signatures of Temporal Variability

In Equation 3.22, we intentionally did not construct the more common power spectrum of the fluctuations about the mean, $\mu^S(\mathbf{b}) \equiv \left\langle V^S(\mathbf{b}) \right\rangle_{\rm turb}$. This is because the impact of scattering on $P^S(\mathbf{b})$ and $\mu^S(\mathbf{b})$ are very different, with

$$\mu^S_{\rm obs}(\mathbf{b}) = e^{-D_\phi[\mathbf{b}/(1+M)]/2}\mu^S_{\rm int}(\mathbf{b}) \tag{3.42}$$

(Johnson & Narayan, 2016). Nevertheless, observed and intrinsic estimates for ratios of the $\mu^S(\mathbf{b})$ may also be constructed:

$$\frac{\mu^S_{\rm obs}(\mathbf{b})}{\mu^{S'}_{\rm obs}(\mathbf{b})} = \frac{\mu^S_{\rm int}(\mathbf{b})}{\mu^{S'}_{\rm int}(\mathbf{b})} \tag{3.43}$$

and their relationship to the corresponding ratios of $P^S(\mathbf{b})$ provide evidence for intrinsic source variability.

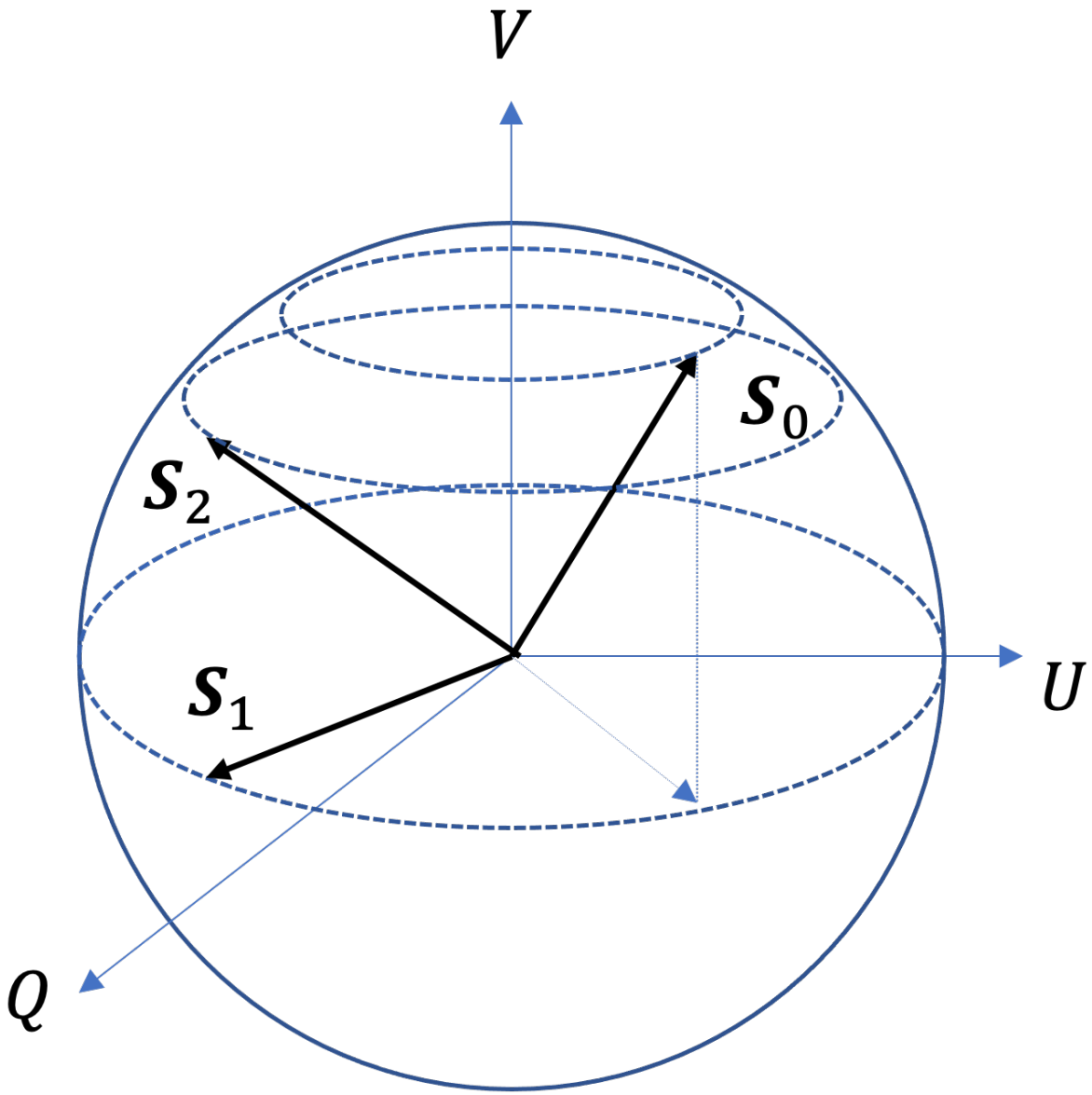

Figure 3.2: Relative orientations of $\mathbf{S}_0$, $\mathbf{S}_1$ and $\mathbf{S}_2$ are shown on the Poincare sphere. $\mathbf{S}_1$ is orthogonal to $\mathbf{S}_0$ and is restricted to lie the Q-U plane. $\mathbf{S}_2$ is orthogonal to both $\mathbf{S}_0$ and $\mathbf{S}_1$. See the text for explicit definitions.

If the intrinsic source is stationary,

$$P^S_{\rm int}(\mathbf{b}) = |\mu^S_{\rm int}|^2(\mathbf{b}), \tag{3.44}$$

and the ratio of $P^S(\mathbf{b})$ and $|\mu^S|^2(\mathbf{b})$ are identical. In contrast, when the intrinsic source is variable,

$$P^S_{\rm int}(\mathbf{b}) = |\mu^S_{\rm int}|^2(\mathbf{b}) + \Sigma^2_S(\mathbf{b}) \tag{3.45}$$

where $\Sigma^2_S(\mathbf{b})$ is the variance due to temporal fluctuations in the source structure on spatial scales $\mathbf{b}$. Thus, when the source is intrinsically variable, $P^S_{\rm int}(\mathbf{b})$ is strictly larger than $|\mu^S_{\rm int}|^2(\mathbf{b})$. Unfortunately, in the absence of prior knowledge about the nature and magnitude of the variability in the two Stokes parameters, we do not know a priori if the ratios are larger, smaller or equal. Nevertheless, if

$$\frac{P^S_{\rm obs}(\mathbf{b})}{P^{S'}_{\rm obs}(\mathbf{b})} \neq \frac{|\mu^S_{\rm obs}|^2(\mathbf{b})}{|\mu^{S'}_{\rm obs}|^2(\mathbf{b})}, \tag{3.46}$$

at a statistically significant degree, then the source must be intrinsically temporally variable. That is, the variability cannot simply be due to the impact of scattering.

3.3 Validation with Simple Source Structure

In this section, we present numerical experiments of scattering mitigation with simple source structures for which we have full control of the relevant power spectra. The purpose of this section is to demonstrate:

1. The ability to construct simple source structures with reasonable power spectra that are similar to the target source, Sgr A*,
2. That the approximation in Equation 3.38 is well justified and successfully permits reconstruction of probes of the intrinsic variability.

We begin with a description of how toy image models with different power spectra and polarization modes are constructed. This is followed by a set of simulated observations in which scattering is incorporated using `eht-imaging` (Chael et al., 2018; Chael et al., 2022). Power spectra are constructed and Equation 3.37 for various choices of S and S' are compared for the intrinsic (pre-scattered) and observed (post-scattered) images. In all cases we assumed a wavelength of 1.3 mm.

3.3.1 Constructing Structured Intrinsic Image

The toy model is comprised of a Gaussian delta ring envelope and set of over-imposed fluctuations with a known power spectrum. In more detail:

1. A mean background image is chosen, $G(\mathbf{x})$. For all experiments reported in this section, we adopt a Gaussian delta ring with radius of 25 μas and with width of 5 μas

2. A power spectrum for the fluctuations is chosen, i.e.,

$$\wp(\mathbf{k}; \sigma_P, \alpha) = \sigma_\wp^2 \left[1 + \left(\frac{\mathbf{k}X}{2\pi}\right)^2\right]^{\alpha/2}, \tag{3.47}$$

   for some normalization $\sigma_\wp$ and fluctuation spectral index α, where X is some maximum spatial scale. Because both Sgr A* and GRMHD simulations exhibit fluctuations dominated by those on the largest spatial scales, we will assume that $\alpha < 0$ generally.

3. A realization of fluctuations are constructed from a set of zero-mean, unit variance Gaussian random variables (GRVs). That is, on a grid in the Fourier domain, at each $\mathbf{k}$ we choose two GRVs, $\mathcal{N}_1$ and $\mathcal{N}_2$, from which the Fourier components of the fluctuation map are given by

$$F_\mathbf{k} = \sqrt{\frac{\wp(\mathbf{k})}{2}} \left(\mathcal{N}_1 + i\mathcal{N}_2\right), \tag{3.48}$$

   where we have suppressed the remaining arguments of the fluctuation power spectrum. The spatial $f(\mathbf{x})$ is constructed by the Fast Fourier transform of the $F_\mathbf{k}$.

4. In the image domain, the desired model for the total intensity is obtained via

$$I(\mathbf{x}) = G(\mathbf{x})e^{f(\mathbf{x})}, \tag{3.49}$$

   where we exponentiate $f(x)$ to ensure positivity.

5. Polarized images are generated in a similar fashion as described above, with two additional Gaussian random fields, $l_1(\mathbf{x})$ and $l_2(\mathbf{x})$ constructed similarly to $f(\mathbf{x})$ but with independent α_{L1} and α_{L2}, from which

$$L_1(\mathbf{x}) = l_1(\mathbf{x})I(\mathbf{x}) \quad \text{and} \quad L_2(\mathbf{x}) = l_2(\mathbf{x})I(\mathbf{x}). \tag{3.50}$$

   These have zero mean by construction.

The definition and the setup the toy model are controlled by five parameters, which encodes five aspects of the desired properties of the toy model: the amplitude of the fluctuations, $\sigma_{\wp}$, the spectral indexes of the power spectra for the total intensity, α, and two polarization models α_{L1} and α_{L2}, and a spatial scale on which power spectrum flattens, X, which we will set to $25\,\mu$as.

Now, we have successfully generated the toy model, with both the total intensity and the polarized components, and the next step is to simulate observations.

3.3.2 Simulated Ensemble of Observations

Observations of Sgr A* are impacted by two additional effects: variability and the interstellar scattering we seek to mitigate. To apply the scattering we make use of the Stochastic Optics package within `eht-imaging`, which implements the scattering model described in Johnson (2016) with the parameters measured in Johnson et al. (2018) and Issaoun et al. (2021). For all simulated Stokes map (I, L_1, and L_2), a single realization of the scattering screen is employed for each simulated instantaneous image.

Variability, both within the source and the scattering screen, is incorporated by producing a large collection of scattered images, each with a unique randomly constructed scattering screen and set of intrinsic fluctuations. In this way, we generate a statistical ensemble of observed images. Note that this procedure ignores potential temporal correlations within the image that will present themselves in the following section, when GRMHD models are considered.

Specifically, in this numerical experiment, we chose the following values for the parameters for this simple source structure model. The amplitude of the fluctuation of the Gaussian delta ring envelope, $\sigma_{\wp}$, is 100. The power index for the total intensity, α, is -4. The power indices associated with the two polarization modes, α_{L1} and α_{L2}, are -4 and -2, respectively. In conclusion, the simple source model has a red power spectrum, dominated by large-scale fluctuation. The associated two polarization modes also have independent red spectra, but with different power indices.

With this source model, we first calculate its intrinsic visibility, for the total intensity and the polarization modes, noted as $V^{I}_{\rm int}(\mathbf{u})$, $V^{L1}_{\rm int}(\mathbf{u})$ and $V^{L2}_{\rm int}(\mathbf{u})$. Second, we generate the scattered image using the scattering model implemented in `eht-imaging`. Each snapshot of the source is scatted with an independent realization of the scattering screen. Third, we calculate the scattered visibility, noted as $V^{I}_{\rm obs}(\mathbf{u})$, $V^{L1}_{\rm obs}(\mathbf{u})$ and $V^{L2}_{\rm obs}(\mathbf{u})$. Then, the intrinsic and scattered visibilities are averaged down over 100 realizations of the source and the

scattering screen. Finally, we take the ratios among averaged scattered visibilities and averaged intrinsic visibilities, respectively.

For this first set of validation tests, we ignore measurement uncertainties, e.g., those associated with thermal fluctuations. Thus, the primary source of uncertainty is sampling error associated with the finite number of simulated images in the ensemble. In Section 3.4, we include more realistic assessments of array performance for EHT and ngEHT.

3.3.3 Power Spectra Estimation Results

We first examine the impact of the scattering on the power spectra of the total intensity, which is shown in the left panel of Figure 3.3. The central peak is associated with the net source structure, i.e., a unit Jy Gaussian delta ring with radius of 25 μas. The ringing is associated with the Fourier transform of the the delta ring as the envelope. The extended plateau at baselines longer than 15 Gλ is associated with two effects: first the small-scale variable structures that we seek to recover, and second the refractive scattering.

It is, in fact, the latter of these two that overwhelmingly dominates, as evidenced by the impact of diffractive scattering, shown by the dashed blue line, which strongly suppresses the contributions from the intrinsic source structure at $u \gtrsim 10\,\mathrm{G}\lambda$.

The power spectra associated with the polarization, shown in the center and right panels of Figure 3.3, do not have a prominent central peak because the total polarization flux vanishes on average (though while small, is non-zero for any given realization). Thus, while again the diffractive scattering suppresses the power at long baselines due to intrinsic structure, there is much less contamination from refractive scattering, which dominates only for $u \gtrsim 20\,\mathrm{G}\lambda$.

In all cases, the power spectra after scattering deviate substantially from those intrinsic to the source. That is, as anticipated, due to both diffractive and refractive effects, the observed power spectra are themselves a poor proxy for the intrinsic power spectra, becoming worse as the spatial scale decreases.

The ratios of observed power spectra, as defined in Equation 3.38 and shown in Figure 3.4, produce remarkable agreement with those from the intrinsic images (i.e., prior to scattering). When the ratio is made with P^I, the intrinsic source structure and positive definite nature of the intensity responsible for the large bump in the left panel of Figure 3.3 introduces a large depression, overwhelming any structure that may be attributed to the small-scale fluctuations. In addition, the dominance of refractive scattering at long baselines in P^I results in a significant departure of the observed from the intrinsic power spectra ratios by $u = 12\,\mathrm{G}\lambda$ as anticipated at the end of Section 3.2.3.

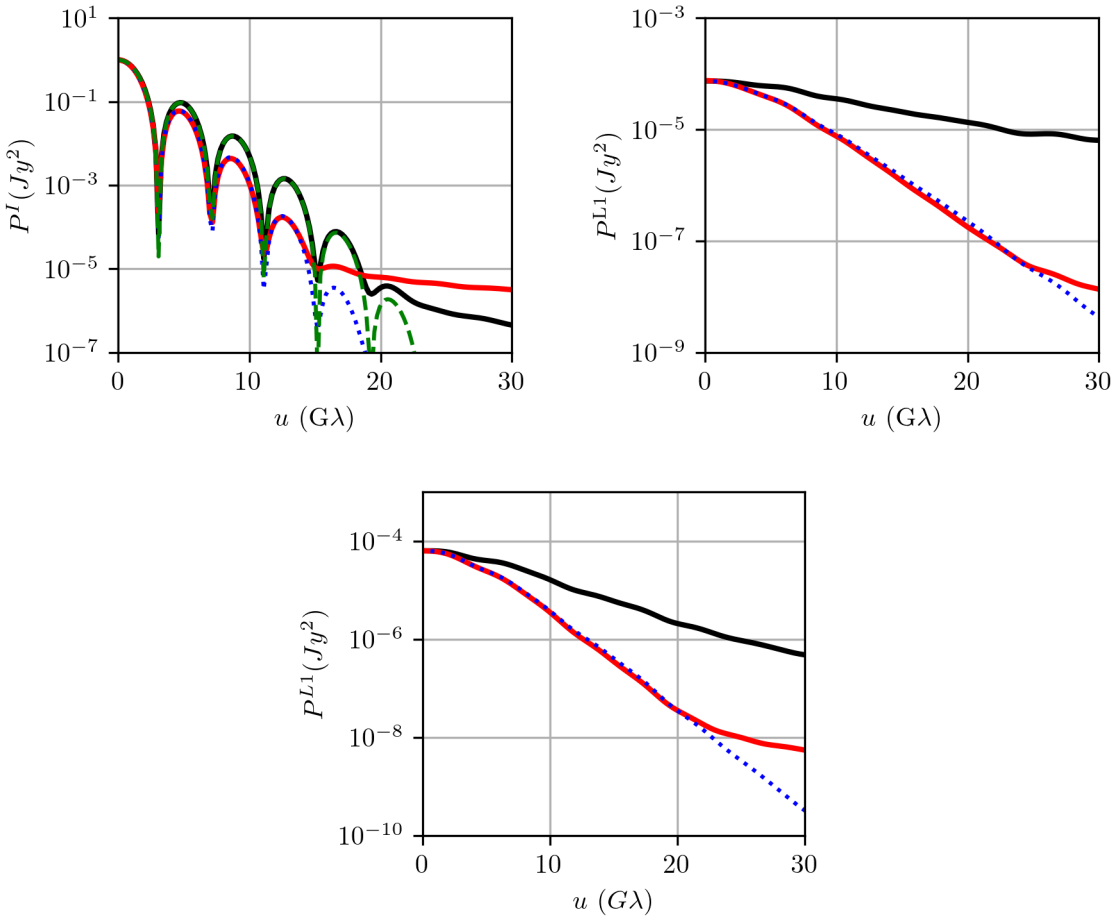

Figure 3.3: Power spectra for the total intensity and two linear polarization modes. From top left clockwise, the three panels are for total intensity, first linear polarization and second linear polarization. The black and red lines are the intrinsic and scattered power spectra, respectively. The blue dotted lines are the diffractively scattered power spectra. The green dashed line in the leftmost panel is the power spectrum of the Gaussian delta ring with radius of 25 μas, which is the same envelope for the simple source model.

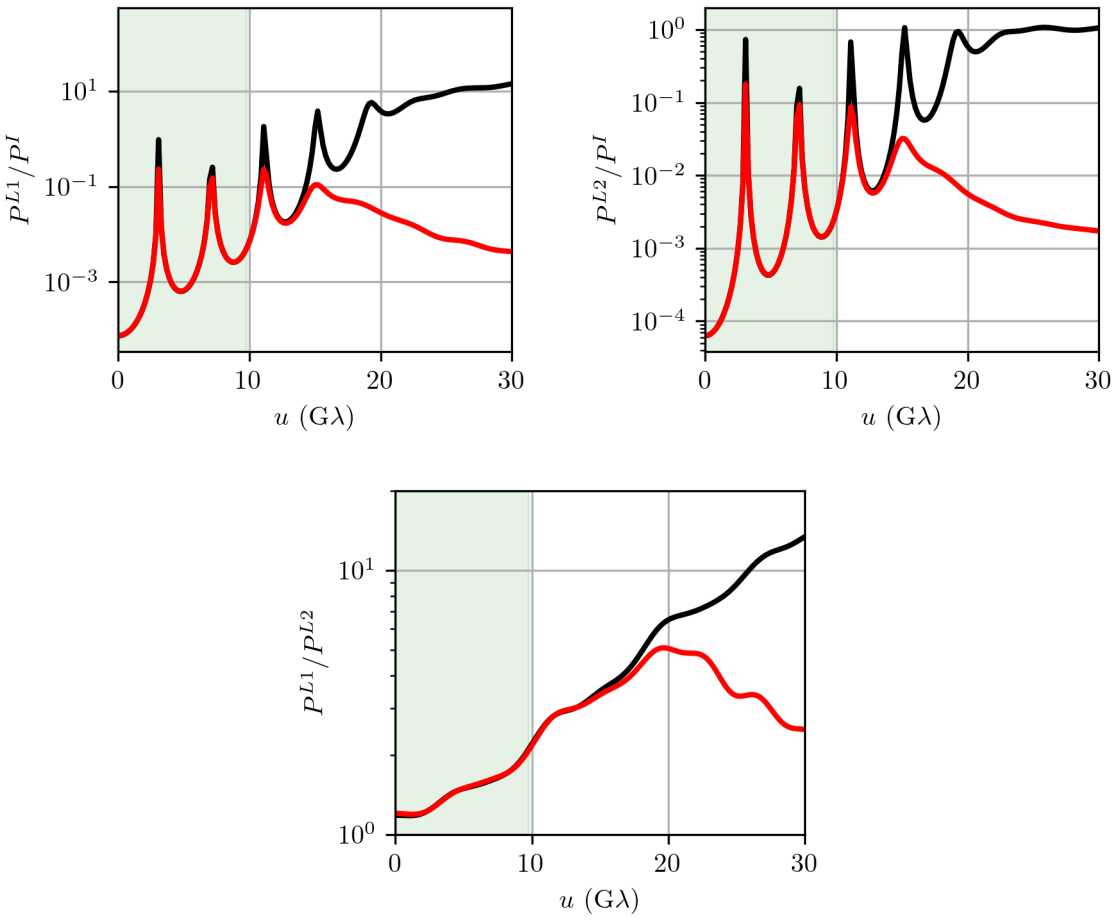

Figure 3.4: Power spectra ratio between the total intensity and the first polarization mode (top left), the total intensity and the second polarization mode (top right), and the two polarization modes (bottom) for the simple source structure defined in Section 3.3. The black line shows the intrinsic power spectra ratio, while the red line is the power spectra ratio observed after scattering. The green band represents the size of Earth-bound baselines at 230 GHz.

However, in stark contrast, the power spectra ratio of the two polarized modes, show in the right panel of Figure 3.4, match well out to $u \approx 17\,\mathrm{G}\lambda$. While beyond $u \approx 20\,\mathrm{G}\lambda$, refractive scattering drives large deviations from intrinsic power spectra ratio, this is well beyond the baselines accessible to EHT and ngEHT at 1.3 mm.

Similar experiments were performed for a variety of choices of the α, α_{L1}, and α_{L2}, with similar results.

While the above is schematic, involving only a very simple source structure, nevertheless a number of immediate conclusions can be drawn that we will see reflected in the more physically applicable demonstrations that follow:

- Observed power spectra are poor estimators in the presence of interstellar scattering for the intrinsic variable structures.
- For all polarization modes, diffractive scattering suppresses long-baseline observed power spectra.
- For polarization modes with large net flux (e.g., Stokes I), refractive scattering substantially contaminates the power spectra.
- Ratios of power spectra generally produced better estimates of the corresponding intrinsic quantities.
- Ratios of power spectra associated with polarization modes with zero net flux are substantially more accurate estimates, extending well beyond the spatial frequency range accessible from the ground at 1.3 mm.

Based on the above, we conclude that when the polarization modes are well chosen, the approximation in Equation 3.38 is well motivated.

3.4 validation with GRMHD simulations

In contrast to the simple, phenomenological models discussed in the previous section, GRMHD simulations provide a natural astrophysically-motivated set of complex source structures. While GRMHD simulations do not afford the freedom to arbitrarily modify the input fluctuation spectra, they do incorporate credible realizations of the anticipated turbulence and magnitude of the polarized flux. As a result, it is possible to reasonably assess the practical limitations imposed by thermal noise noise and limited number of

observations to be averaged. Here we repeat the kinds of tests performed in Section 3.3 for one such GRMHD simulation, taken from the set presented in Event Horizon Telescope Collaboration et al. (2022e).

3.4.1 GRMHD Simulated Intrinsic Image and Simulated Observation

We employ a SANE, $a = 0$, $i = 30°$, $R_{\rm high} = 40$ simulation from the set presented in Event Horizon Telescope Collaboration et al. (2022e), to which we direct the reader for information about the simulation particulars. For our purposes, it is important only that the simulation presents a physically self-consistent realization of the kind of turbulence, degree of net polarization ($\sim$3%), and typical polarization fractions ($\sim$20%) appropriate for Sgr A*.

An arbitrary snapshot drawn from the simulation is shown in Figure 3.5 with its four Stokes components, and in Figure 3.6 with the constructed polarization modes $\mathbf{S}_0$, $\mathbf{S}_1$ and $\mathbf{S}_2$, as stated in Section 3.2.4.

Note that because our goal here is not to predict the statistics of GRMHD simulation images, but rather to demonstrate the ability to faithfully retrieve statistical elements of the underlying intrinsic images in the presence of scattering, this single GRMHD simulation is sufficient for our purposes.

The simulated emission is assumed to arise from synchrotron emission due to a population of hot electrons. The simulation data contains the total intensity and polarization maps at 1.3 mm for accretion flow parameters relevant for Sgr A*, i.e., the four Stokes parameters, I, Q, U and V, for 3000 individual snapshots (Event Horizon Telescope Collaboration et al., 2022e, and references therein). From these intrinsic images, scattered images are produced using the Stochastic Optics package within `eht-imaging` in manner identical to that used in Section 3.3.

We follow a nearly identical procedure to generate simulated observations from the GRMHD simulations as that described in Section 3.3.2. This procedure differs in that the polarization maps are now identified with the three polarized Stokes maps (Q, U, V). Where these are scattered, we produce a new scattering screen realization for each image. For each frame, we construct the single-snapshot estimate of the spatial power spectra associated with I, Q, U, and V are constructed, i.e., $\left|V^I\right|^2$, $\left|V^Q\right|^2$, $\left|V^U\right|^2$, and $\left|V^V\right|^2$, respectively. This procedure is repeated for every image in the GRMHD simulation

to generate estimates for the ensemble- and turbulence-averaged estimates of the spatial power spectra.

3.4.2 Spatial Power Uncertainty Estimate

To assess if the observed and intrinsic spatial power spectra are distinguishable, we require an estimate of the anticipated uncertainty on the spatial power spectra. This arises from multiple potential origins. However, there are two irreducible contributors: thermal noise associated with the individual stations within the EHT and ngEHT, and the sampling uncertainty due to an insufficiently complete ensemble. Here we describe how we estimate each of these. Note that we make aggressive assumptions to *reduce* both sources of uncertainty, thereby enforcing a *stricter* limit on the required fidelity of the spatial power spectra ratios.

Thermal Noise Estimates

The thermal error at EHT stations arises from a number of potential sources, including the atmosphere, side lobes picking up the local environment, and the electronics within receiver. The combination is typically characterized by a system equivalent flux density, SEFD. In terms of these, the uncertainty on a visibility measured by stations A and B with a bandwidth ΔB and coherently averaged over a time τ,

$$\sigma_{AB} = \sqrt{\frac{\mathrm{SEFD}_A \mathrm{SEFD}_B}{2\tau\Delta B}}, \tag{3.51}$$

SEFDs for EHT stations are listed in Table 2 of (Event Horizon Telescope Collaboration et al., 2019f). These range from 74 Jy for ALMA to 19300 Jy for SPT. We adopt, for illustration, PV and APEX, for which the SEFDs are 1900 Jy and 4700 Jy, respectively, the intermediate SEFDs in the EHT. Were we to adopt the two stations with the highest SEFDs in the EHT, SMT and SPT, the estimated thermal noise could be a factor of 30 higher. The median thermal noise across the EHT is roughly an order of magnitude larger than the minimal value. Finally, we adopt a bandwidth of 4 GHz, corresponding to the combination of high- and low-band data from the EHT, and an integration time of 10 min, corresponding to a typical scan time, yielding $\sigma_{\rm th} \approx 0.4$ mJy. Upon averaging N independent observations, the effect thermal noise is reduced by a further factor of $N^{-1/2}$. Note that this is independent of the particular polarization mode under consideration.

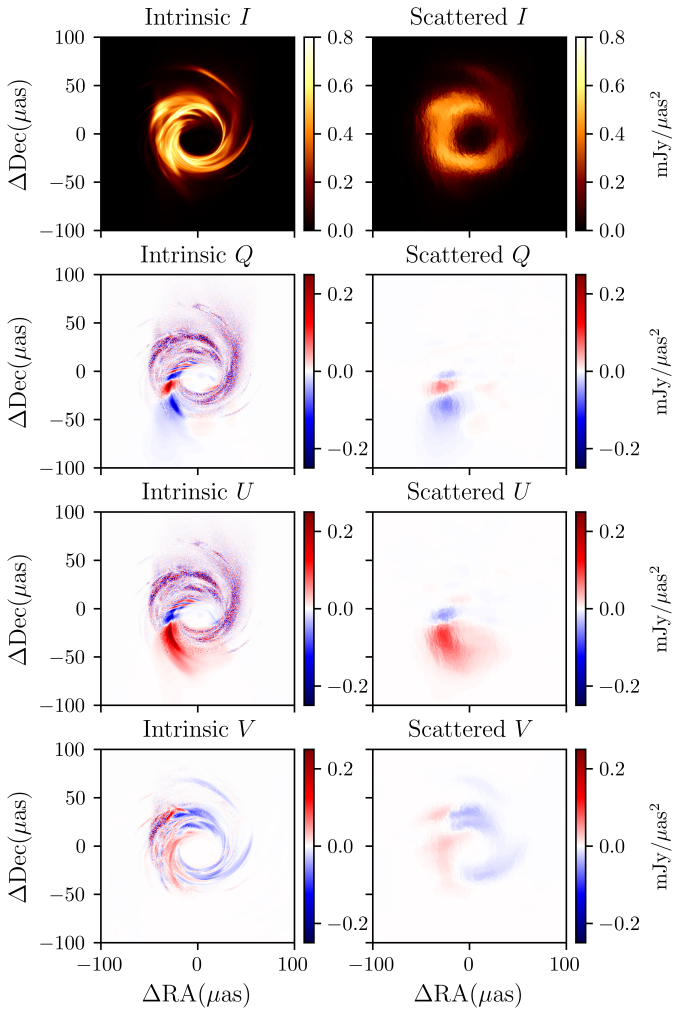

Figure 3.5: Arbitrary snapshot drawn from the GRMHD simulation used. The figure includes the Stokes I, Q, U and V components (left) and their corresponding scattered versions (right). Bottom row: the two constructed polarization modes, $S1$ and $S2$, are shown, both intrinsic and scattered.

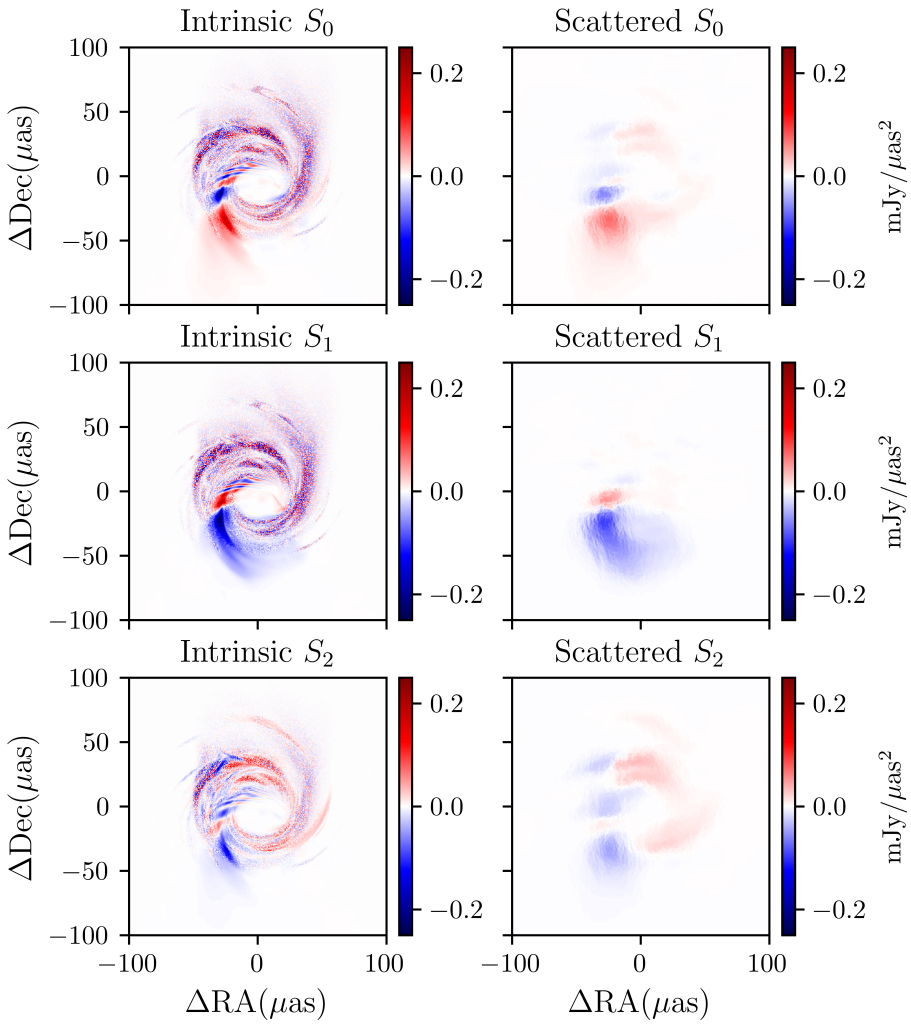

Figure 3.6: The same arbitrary snapshot drawn from the GRMHD simulation used in Figure 3.5. The figure includes the two constructed polarization modes, $S1$ and $S2$, both intrinsic and scattered.

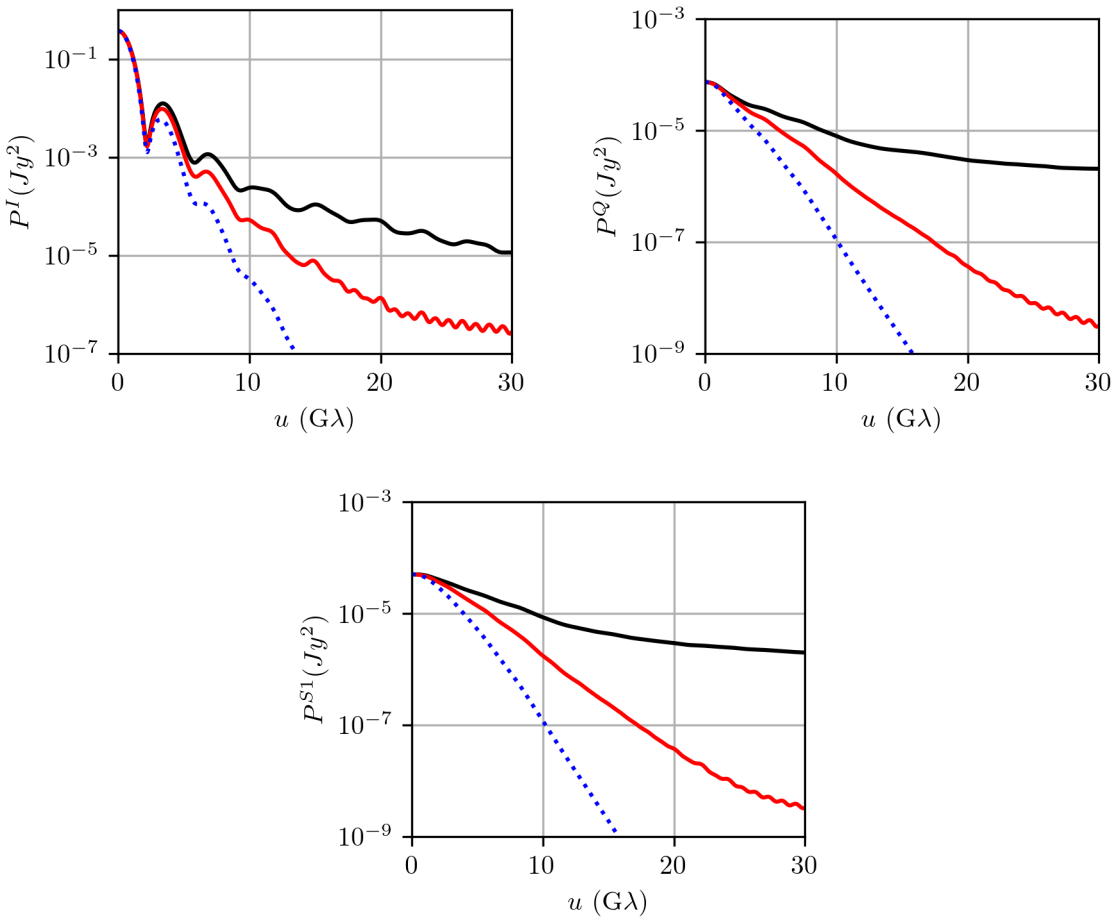

Figure 3.7: Power spectra for Stokes I (top left), Stokes Q (top right), and the optimal $S1$ (bottom) before (black) and after (red) application of the scattering screen. The dotted blue line represents the diffractively scattered power spectrum.

The thermal noise on the spatial power spectra after averaging N independent observations is obtained via standard error propagation,

$$\sigma_{\langle V_A^2 \rangle} = \frac{2\sigma_{\mathrm{th}}}{N^{1/2}} \left\langle |V_A|^2 \right\rangle^{1/2}. \tag{3.52}$$

The thermal noise on the ratio of spatial power spectra after averaging N observations is,

$$\sigma_{\langle V_A^2 \rangle / \langle V_B^2 \rangle} = \frac{2\sigma_{\mathrm{th}}}{N^{1/2}} \frac{\left\langle |V_A|^2 \right\rangle}{\left\langle |V_B|^2 \right\rangle} \left(\frac{1}{\left\langle |V_A|^2 \right\rangle} + \frac{1}{\left\langle |V_B|^2 \right\rangle} \right)^{1/2}. \tag{3.53}$$

Sampling Noise Estimates

The sampling noise describes the uncertainty associated with having a finite number of samples in the estimate of the ensemble and turbulence averages. When the number of samples, N, is large, the central limit theorem implies that this is related to the variance of the visibility amplitude, i.e.,

$$\Sigma_{V_A} = \left[\left\langle |V_A|^2 \right\rangle - \left\langle |V_A| \right\rangle^2 \right]^{1/2}. \tag{3.54}$$

Note that unlike the thermal noise, this differs between the various Stokes parameters, which may exhibit different degrees of variability. From $\Sigma_{\langle V_A \rangle}$, the uncertainties on the spatial power spectrum and spatial power spectra ratios can be immediately constructed via the standard error propagation,

$$\Sigma_{\langle V_A^2 \rangle} = \frac{2\Sigma_{\langle V_A \rangle}}{N^{1/2}} \left\langle |V_A|^2 \right\rangle^{1/2}, \tag{3.55}$$

and

$$\Sigma_{\langle V_A^2 \rangle / \langle V_B^2 \rangle} = \frac{2}{N^{1/2}} \frac{\left\langle |V_A|^2 \right\rangle}{\left\langle |V_B|^2 \right\rangle} \left(\frac{\Sigma^2_{\langle V_A \rangle}}{\left\langle |V_A|^2 \right\rangle} + \frac{\Sigma^2_{\langle V_B \rangle}}{\left\langle |V_B|^2 \right\rangle} \right)^{1/2}. \tag{3.56}$$

3.4.3 Power Spectra Estimation Results

The mean power spectra associated with Stokes I, Q, and $S1$ are shown in Figure 3.7. As with the toy model presented in Section 3.3, the nonzero total flux results in a peak at $u = 0\,\mathrm{G}\lambda$, and a deficit associated with the diffractive component of the scattering at long baselines. As with Figure 3.3, refractive scattering lessens the reduction, seen

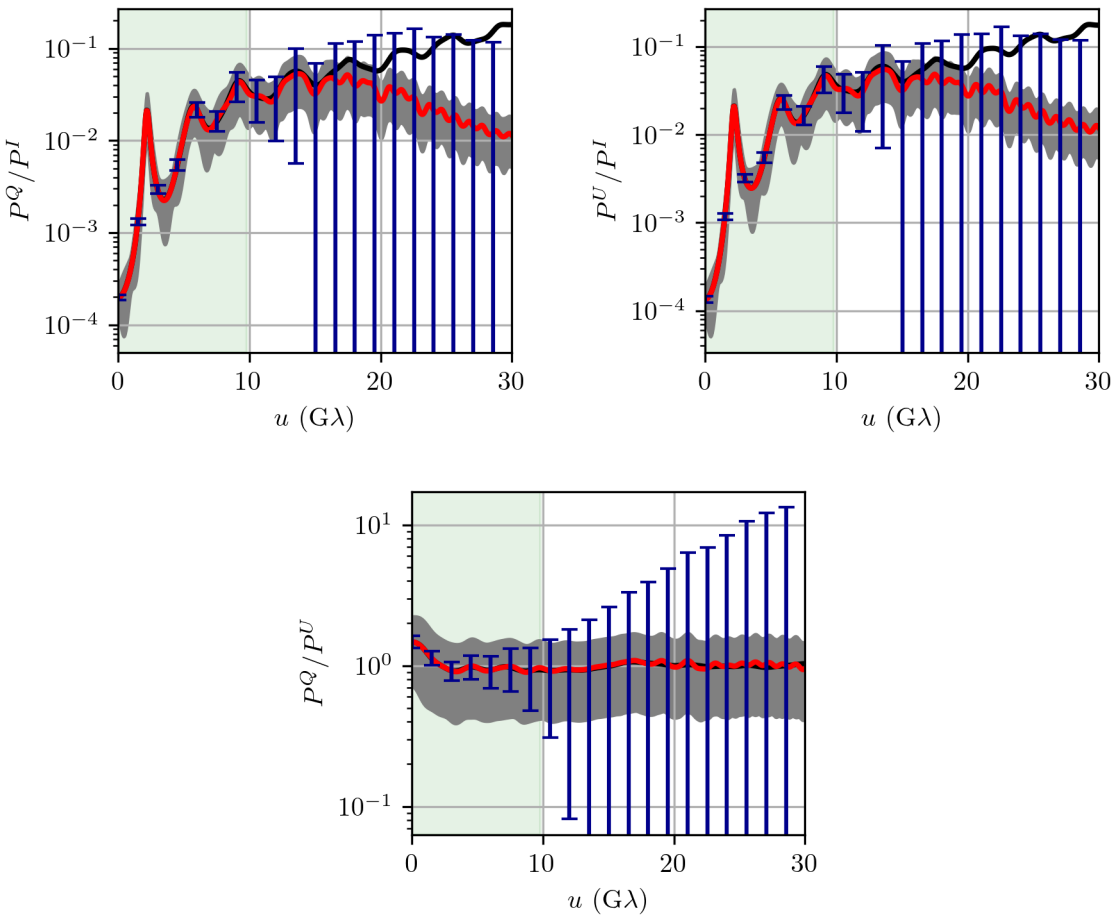

Figure 3.8: Ratios of the power spectra of different polarization modes. From left to right, the three panels show the power spectra ratio for P^Q/P^I, P^U/P^I and P^Q/P^U. The black and red line represents before and after the imposition of scattering. The blue error bars are the thermal noise associated with telescopes. We used PV and APEX, which have the intermediate sensitivities among all EHT telescopes, to generate the error bars. The gray error bands are the sampling noise associated with the intrinsic spatial variability of the intrinsic source, which we averaged down assuming 25 independent observations. The green band represents the size of Earth-bound baselines at 230 GHz.

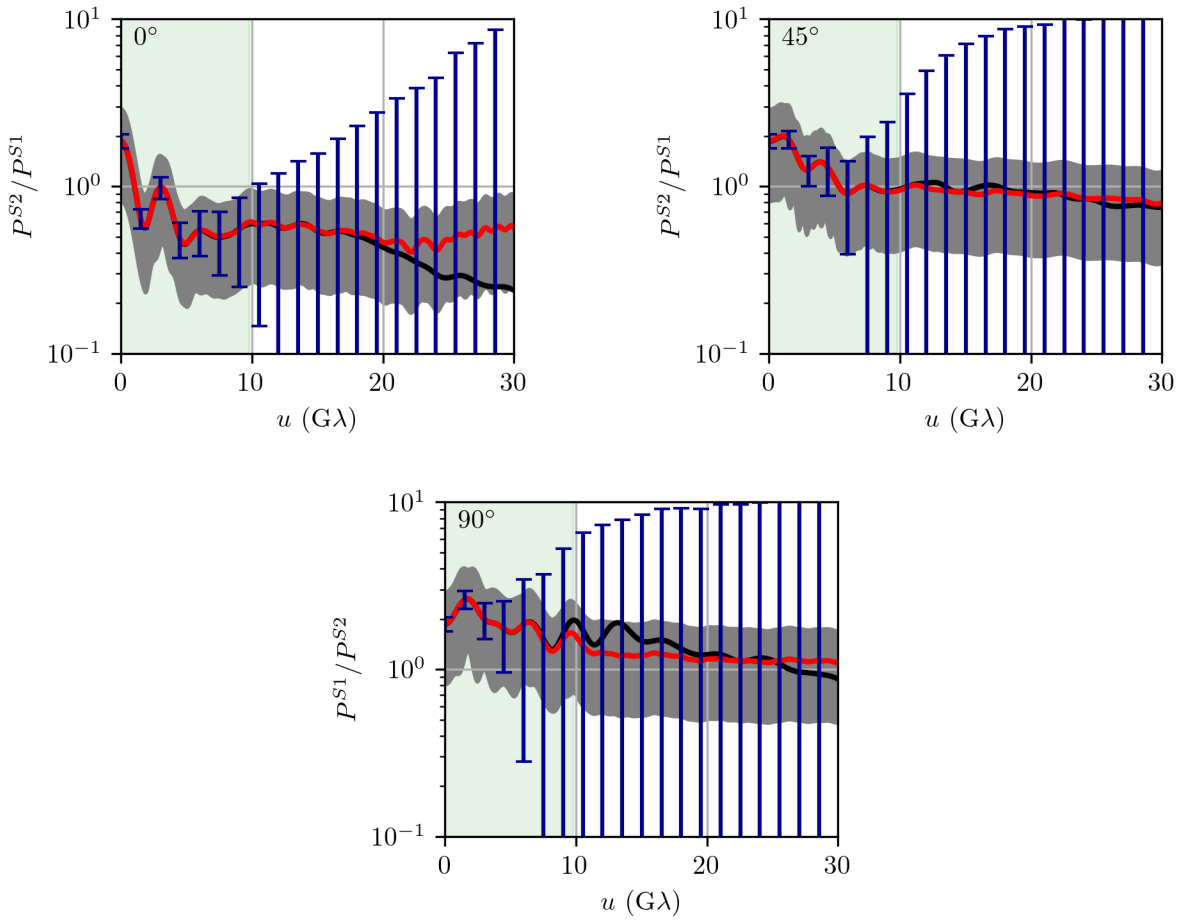

Figure 3.9: Intrinsic (black) and observed (red) P^{S2}/p^{S1} along rays at different orientations relative to the u axis. From left to right: 0° (u axis), 45°, and 90° (v axis). The sampling noise and thermal errors associated with $N = 25$ observations are indicated by the gray band and blue error bars, respectively.

most prominently in P^I due to the comparatively large net value. In all cases, scattering significantly suppresses the power spectra relative to their intrinsic values, as anticipated.

The mean P^Q/P^I and P^{S2}/P^{S1} power spectra ratios are shown in Figure 3.8, and are directly comparable to those in Figure 3.4. In addition, the sampling and thermal error scales for $N = 25$ independent observations of the source and scattering screen are indicated, providing a natural assessment of the accuracy of the approximation in Equation 3.38. Apart from differences in the underlying source structure, e.g., the clearly evident oscillations associated with the lensed emission ring, the gross properties noted in Section 3.3 remain. For example, the suppression at short baselines by the non-zero mean total flux in the P^Q/P^I ratio (similar to P^U/P^I), and the lack of such a suppression in the Stokes basis defined by $\mathbf{S}_1$ and $\mathbf{S}_2$. Even at the longest ground-based baseline lengths – 10 Gλ at 230 GHz – the impact of the scattering screen is effectively mitigated.

While Figure 3.8 shows only the ray through the $(u, v)-$plane along the u-axis, this improvement is generic. Figure 3.9 presents P^{S2}/P^{S1} for radial rays at different orientations. While the magnitude of the discrepancies between the observed and intrinsic power spectra ratios and the location where they begin to differ varies, in all cases, at all baselines relevant for EHT and ngEHT, these discrepancies are small in comparison to relevant uncertainties.

In addition to vastly increasing the number and density of baselines available, the ngEHT envisions receivers with increased bandwidth and improved detector efficiency that will improve sensitivity across the array, reducing the thermal noise contributions to the visibility uncertainties (Raymond et al., 2021). For nominal SEFDs associated with the reference ngEHT array in Raymond et al. (2021) and a bandwidth of 16 GHz, we show P^{S2}/P^{S1} at the observing frequencies under discussion for the ngEHT in Figure 3.10. As shown in the middle panel of Figure 3.10, for the ngEHT, thermal noise ceases to be the chief impediment to measuring the intrinsic power spectra ratios below ~ 15 Gλ, covering all Earth-sized baselines. The right panel of Figure 3.10 shows P^{S2}/P^{S1} at 345 GHz with ngEHT telescope sensitivities and bandwidths; again all ground-base baselines are dominated by the sampling uncertainty associated with source variability. Out to ~ 50 Gλ, nearly twice the 30 Gλ region shown in Figure 3.10, the observed mean power spectra ratio provides an excellent estimate of the intrinsic ratio. Within ~ 100 Gλ observed and intrinsic power spectra ratio differ by less than the sampling uncertainty. These imply that future high-frequency polarimetric observations by EHT, ngEHT, and space-based mm-VLBI experiments will all be able to accurately statistically probe the turbulent structures in horizon-scale targets on scales from 7 μas (ground) to 2 μas (space). Whereas at lower observation frequencies, the impact of scattering is enhanced. In the left panel of Figure 3.10, which is at 86 GHz, although scattering deviates the power spectrum ratio from

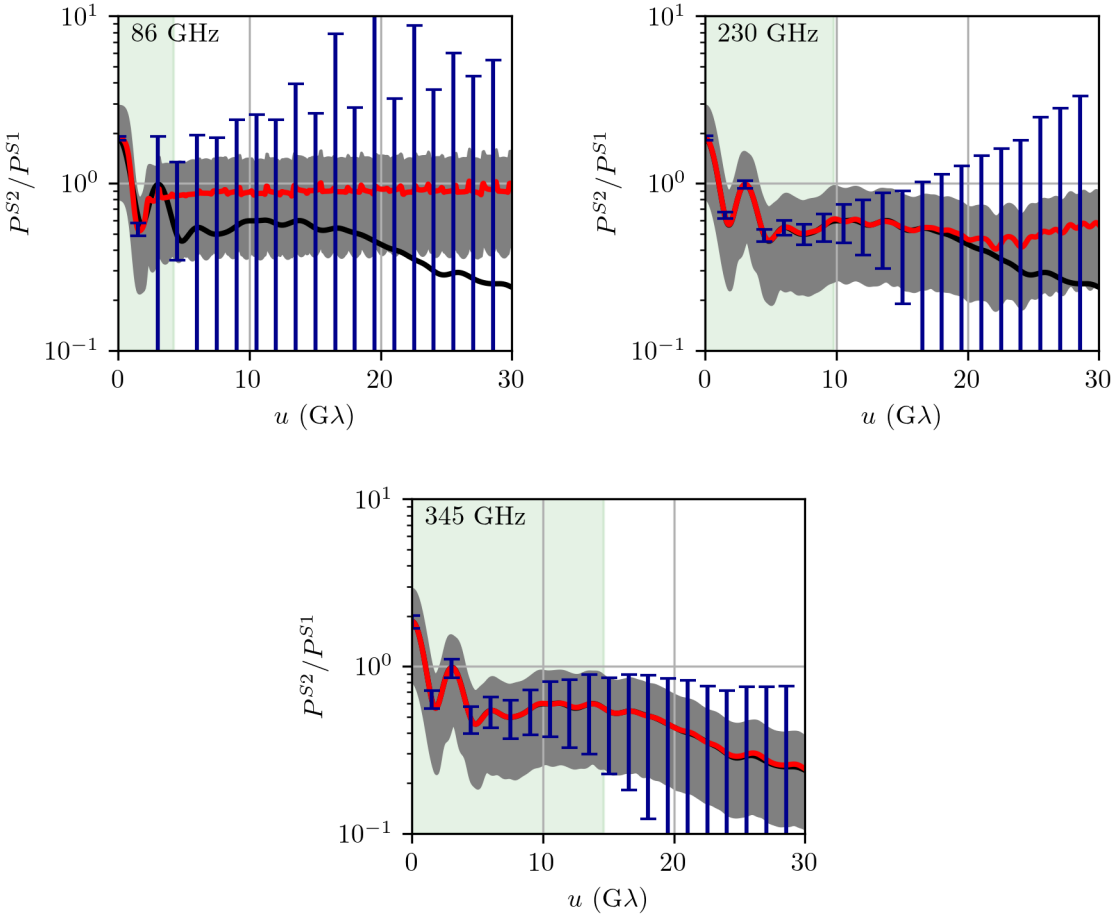

Figure 3.10: Mean intrinsic (black) and observed (red) ratio of the power spectra associated with polarization modes defined by the Stokes vectors $\mathbf{S}_1$ and $\mathbf{S}_2$ at 86 GHz (left), 230 GHz (middle) and 345 GHz (right). The sampling noise and thermal errors associated with $N = 25$ observations and based on ngEHT telescope sensitivities are indicated by the gray band and blue error bars, respectively. The green band represents the size of Earth-bound baselines at 86 GHz, 230 GHz and 345 GHz, from left to right.

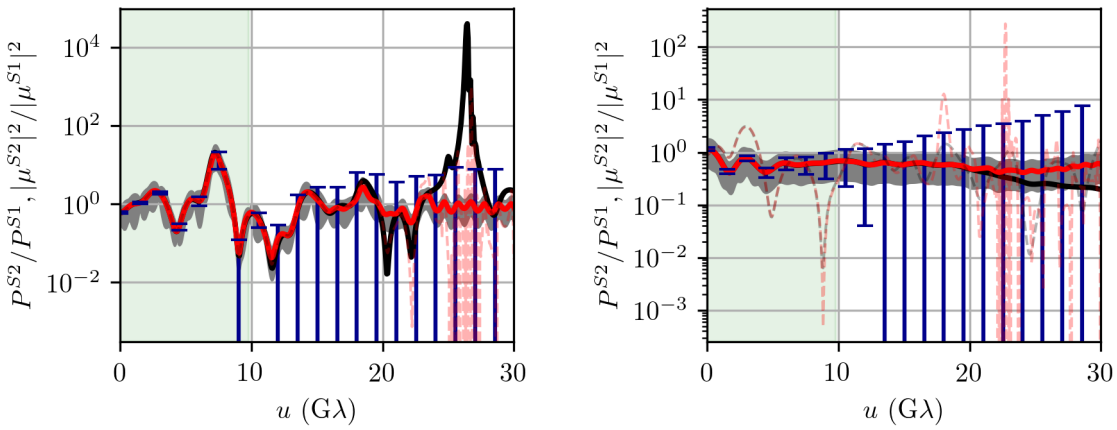

Figure 3.11: Ratios of the power spectra (solid lines) and means (dashed lines) for the two constructed polarization modes, $\mathbf{S}_1$ and $\mathbf{S}_2$. Left: a single, static intrinsic image, represented by a single GRMHD snapshot, viewed through an evolving scattering screen. Right: an evolving intrinsic image and scattering screen. In both panels, the sampling noise and thermal errors associated with N = 25 observations and based on ngEHT telescope sensitivities are indicated by the gray band and blue error bars, respectively. The green band represents the size of Earth-bound baselines at 230 GHz.

the intrinsic at as early as 3 Gλ, which is the Earth-based VLBI baseline limit at this frequency, they are within the allowed sampling uncertainty until 20 Gλ. This implies the possibility to apply this scattering mitigation scheme to data from GMVA and other telescopes with lower observation frequencies.

The ability explicitly distinguish between intrinsic source variability and extrinsic evolution in the scattering screen using power spectra and mean ratios is demonstrated in Figure 3.11. Like P^{S2}/P^{S1}, the ratio of the means, $|\mu^{S2}|^2/|\mu^{S1}|^2$, are insensitive to the scattering for baselines relevant for current and future Earth-bound VLBI arrays. When the source is static, here taken to be a single GRMHD snapshot, the two sets of ratios are identical out to baselines well in excess to those accessible on the ground, ultimately limited by diffractive scattering. In contrast, for variable sources, the two ratios differ at high significance. Therefore, the comparison of these two ratios, i.e., P^{S2}/P^{S1} and $|\mu^{S2}|^2/|\mu^{S1}|^2$, presents a way in which to find direct evidence for intrinsic source evolution.

Which component of the uncertainty dominates depends on baseline length. At suf-

ficiently large u the strong suppression due to diffractive scattering reduces the signal precipitously. The lower intrinsic S/N of the polarized data result in characteristically larger thermal uncertainties on the power spectra ratio. At short baselines, the sampling error dominates. These two regimes conceptually differ in the manner that measurements can be improved. The thermal noise can be reduced by improvements to station sensitivity (e.g., increased bandwidth, dish size, phase referencing, etc.). In contrast, the sampling noise is a consequence of the intrinsic variability alone, and can only be improved by repeated observation. Because additional observation epochs also reduce the thermal noise at the same rate, where the sampling noise dominates, it will do so regardless of the number of observations.

The location of the transition from sampling dominated to thermally dominated noise depends on the nature of the variability and the sensitivity of the individual stations (see Figure 3.15). For the simulation considered here and the median thermal noise, this transition occurs just beyond $10\,\mathrm{G}\lambda$. However, for the baseline with the maximum thermal noise, the uncertainty at all baselines is dominated by the thermal component, implying that sensitivity of existing EHT stations is likely to be the limiting factor in the accuracy with which the power spectra ratios can be measured.

3.4.4 Physical Interpretation of the Power Spectra Ratio Curves

To interpret the physical meaning of the curve for the power spectrum ratio, we look at the intrinsic power spectrum ratio of a long and converged GRMHD simulation, as described in Qiu et al. (2023). This simulation, characterized by its lengthy duration of 100000 M with the best detrending available, features a MAD simulation with $R_{high} = 20$. It explores a range of black hole spins from -0.9 to $+0.9$ in 0.2 inclement and inclination angles between 10° and 170°, adjusted in 20-degree steps.

The extensive duration of the GRMHD simulation is pivotal for accurately interpreting the power spectrum ratio. Shorter, unconverged simulations may yield power spectrum ratio curves that fluctuate based on the realization of the simulation, obscuring the influence of underlying physical parameters. However, the computational intensity of GRMHD simulations constrains the number of simulations available for analysis, thereby limiting our capacity to extract definitive physical interpretations from the power spectrum ratio curves.

Nevertheless, we calculate the power spectrum and their ratios for different polarization modes of this specific GRMHD simulation, analyzing the impact of different inclination angles and different spins on the profile of the power spectra ratio. We first look at the

simulations with the same spin values, viewed at different inclination angles. The power spectra ratio shows a weak correlation to the inclination angles at short baseline length with high positive spins. Figure 3.12 shows the power spectrum ratio for the two linear polarization modes, Q and U for different spins: negative spins, zero spin and positive spins. For the positive spin case, the power spectrum ratio for face-on (inclination $90°$) is always the highest, while the power spectrum ratios are almost identical for different negative spins. The weak dependence on inclination angles is more prominent for the power spectrum ratio for the two constructed polarization modes $S1$ and $S2$, where edge-on (inclination $0°$) is always the highest and face-on (inclination $90°$) is always the lowest, as shown in Figure 3.13. This trend is also present for negative spins, which is absent for the ratio between Stokes Q and U.

The second case is when the GRMHD simulations are viewed from the same inclination angle, we then inspect the power spectrum ratios for different spins. Shown in Figure 3.14 for the power spectra ratio for Stokes Q and U, for edge-on (inclination $0°$), the power spectrum ratio curves for negative spins cluster together, as do those for positive spins; however, this distinction fades when transitioning to face-on views (inclination $90°$). This grouping trend is faint and primarily observable at shorter baselines ($< 5\mathrm{G}\lambda$).

In summary, we may be able to extract information from the intrinsic power spectrum ratio curves. The values of the power spectrum ratio weakly depends on:

1. whether the black hole is prograde or retrograde,
2. the accretion disk is face-on or edge-on.

However, as we have explained above, the correlation is weak and needs testing with a larger number of GRMHD simulations with different physics conditions. For example, since we are analyzing the accretion turbulence structure, simulations with wider range of plasma prescriptions (R_{high}) would be very helpful. This limitation highlights the need for a broader set of simulations to robustly interpret these spectral features. The weak correlations between spin and inclination angle deduced from the power spectrum ratios, while indicative of some physical features of the underlying simulation, suggest that additional simulation parameters may be necessary to enhance the discriminative power of our scattering mitigation scheme.

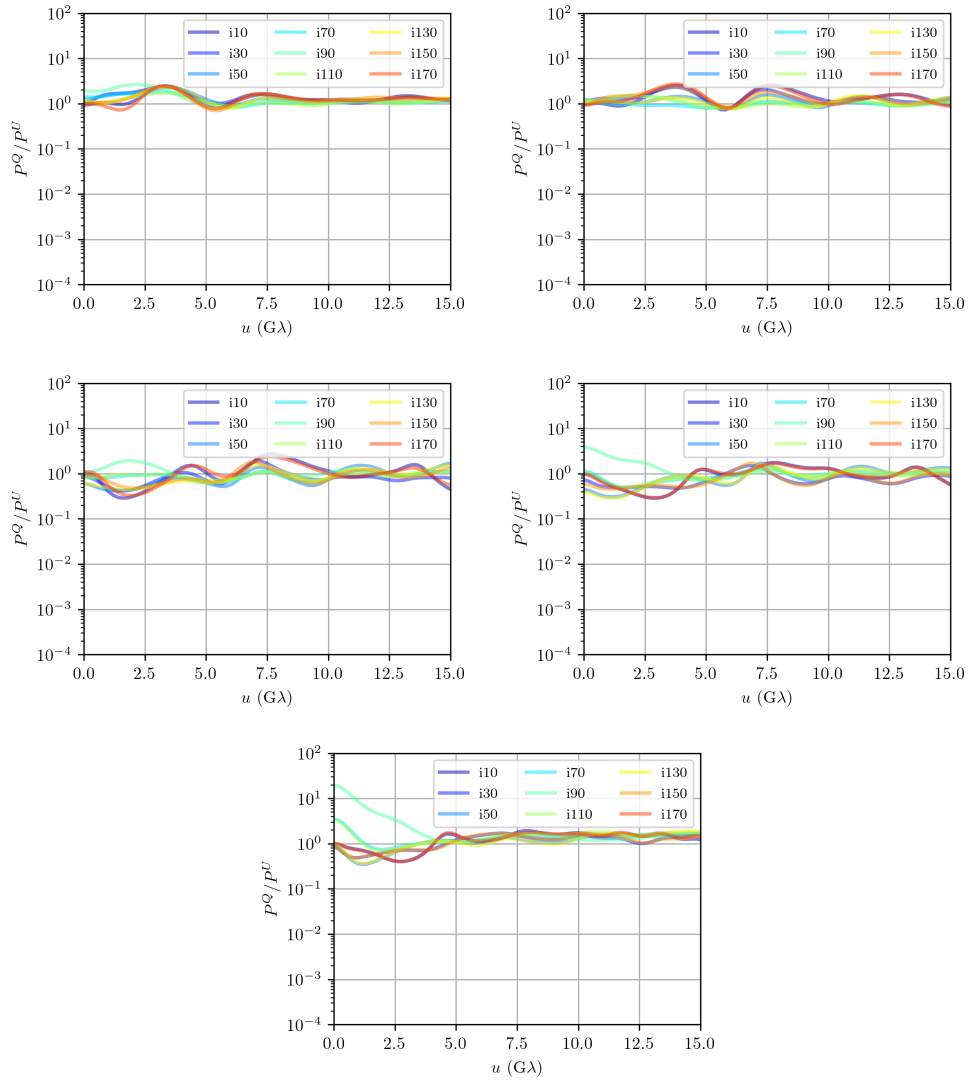

Figure 3.12: The power spectrum ratio between the Stokes Q and U. From top to down, left to right are for GRMHD simulations with spin -0.9, -0.5, 0, 0.5 and 0.9. Different colors in each panel represents one inclination angle, ranging from 10° to 170°, with an inclement of 20°.

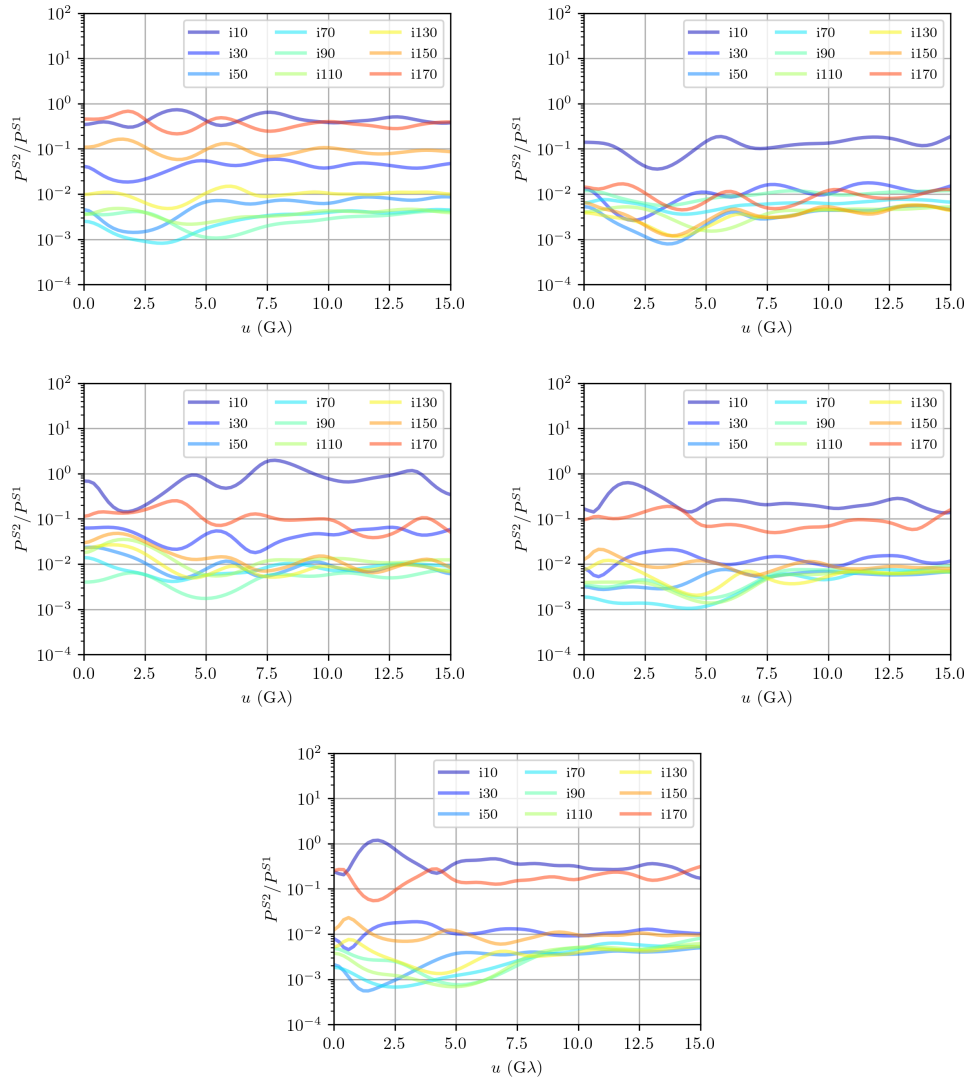

Figure 3.13: The power spectrum ratio between the Stokes $S2$ and $S1$. From top to down, left to right are for GRMHD simulations with spin -0.9, -0.5, 0, 0.5 and 0.9. Different colors in each panel represents one inclination angle, ranging from 10° to 170°, with an inclement of 20°.

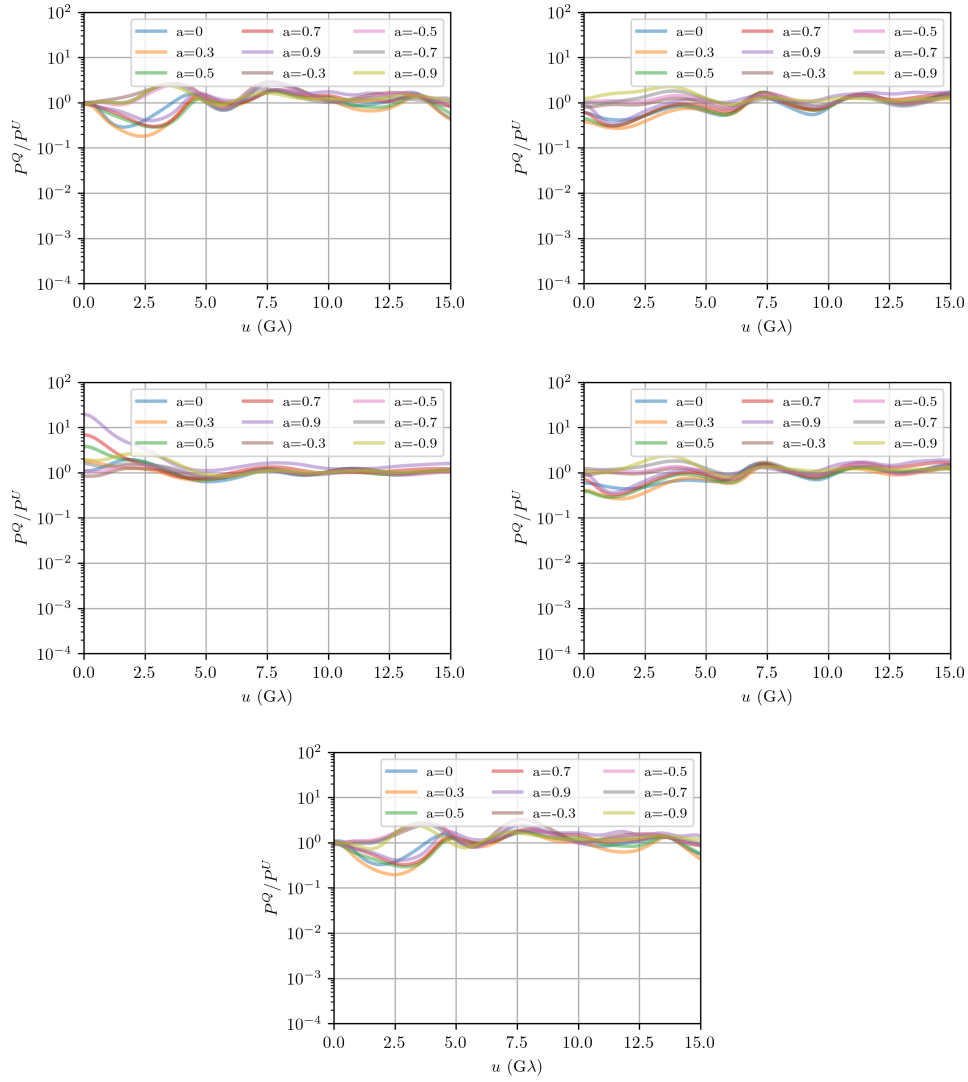

Figure 3.14: The power spectrum ratio between the Stokes Q and U. From top to down, left to right are for GRMHD simulations with inclination angle of 10°, 50°, 90°, 130° and 170°. Different colors in each panel represents different spins, ranging from -0.9 to 0.9.

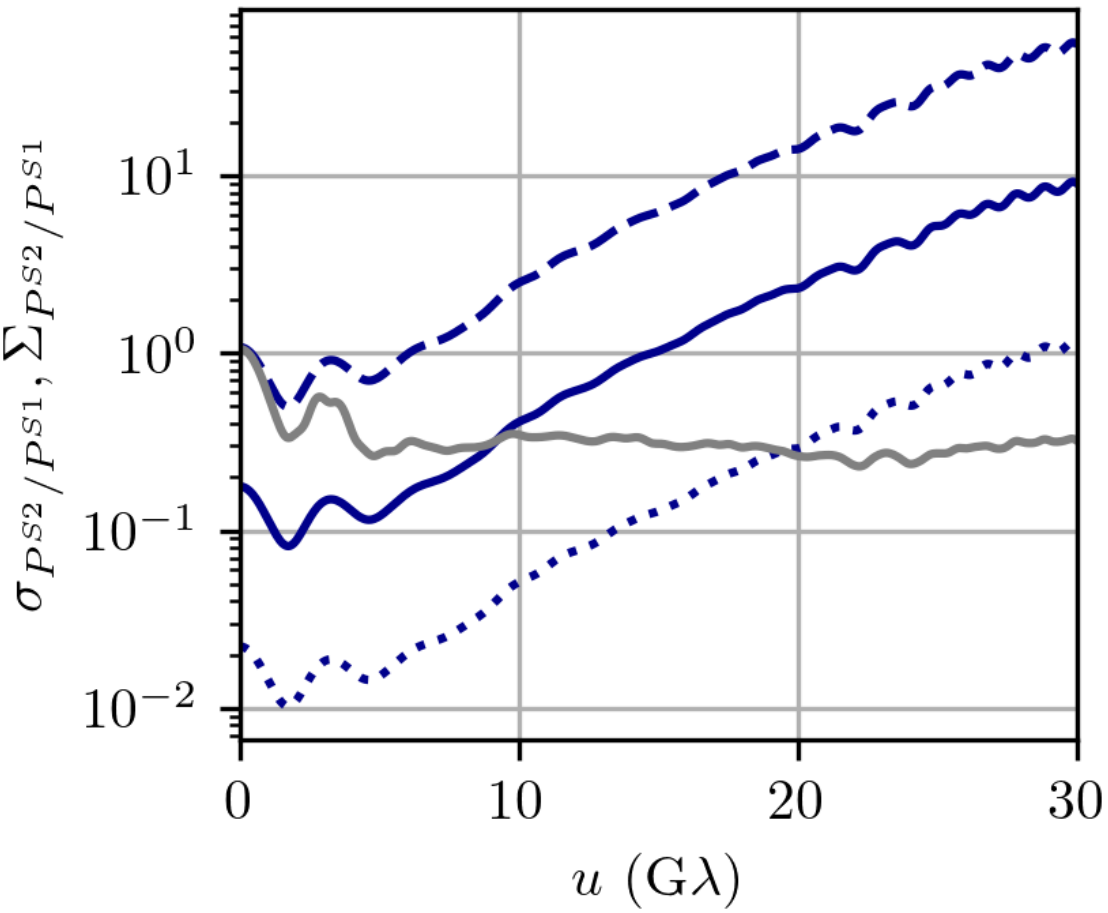

Figure 3.15: Comparison of the sampling and thermal noise estimates for P^{S2}/P^{S1} at 230 GHz. The thermal noise for the minimum, median, and maximum noise estimates are shown by the dotted, solid, and dashed blue lines. The sampling noise is indicated by the gray line.

3.5 Conclusions

Interstellar scattering associated with turbulence in the ISM is non-birefringent for physically reasonable magnetic field strengths. As a consequence, the effect of scattering on horizon-resolving polarization maps of Sgr A* is expected to be independent of the polarization mode being observed. This presents an opportunity to statistically separate the small-scale structures induced by refractive scattering and those intrinsic to the source, presumably due to turbulence within the near-horizon emission region.

We characterize the statistical properties of the structural variability by their power spectra, P^S, defined to be the mean squared visibility associated with Stokes parameter S. This definition is convenient because the impact of scattering is a linear operator that may be expressed as a tensor convolution acting on the P^S. As far as S/N permits, this convolution may be inverted via a perturbative expansion; for existing and proposed Earth-sized mm-VLBI arrays, like the EHT and ngEHT, only the first term in the expansion is required. This effectively reduces to applying constraints to the ratio of P^S, and is otherwise insensitive to the details of the scattering screen.

It is possible to select the polarization modes to minimize the impact of refractive scattering and simplify the interpretation of the P^S. We do this by constructing a particular basis of Stokes vectors, $\mathbf{S}_1$ and $\mathbf{S}_2$, that are orthogonal to the source-integrated mean Stokes vector. These correspond to the fluctuations in the projected orientation of the magnetic fields on the sky and along the line of sight, respectively. Thus, the ratio P^{S2}/P^{S1} is a direct measure of the degree of isotropy in the MHD turbulence across spatial scale.

Using both a toy model, in which there is substantial control over the properties of the turbulent structures, and a GRMHD simulation, which contains a realistic representation of MHD turbulence, we have demonstrated the ability to reconstruct various intrinsic power spectra ratios, including P^{S2}/P^{S1}. At all baselines accessible to ground-based mm-VLBI experiments, the difference between the reconstructed and intrinsic P^{S2}/P^{S1} is small in comparison to the uncertainties due to finite sample size and measurement errors. This remains true for other power spectra ratios between polarized components (e.g., P^Q/P^U) on baseline lengths of interest, and at higher observation frequencies.

The improved sensitivity expected in future mm-VLBI experiments can significantly increase the accuracy with which P^{S2}/P^{S1} may be measured. More importantly, arrays like that envisioned by the ngEHT provide a much more dense sampling of the $(u, v)-$plane, and therefore the ability to measure more completely the two-dimensional power spectra ratios. The thermal uncertainties may be further reduced by aggregating nearby measurements in the $(u, v)-$plane and/or exploiting assumptions regarding azimuthal symmetry; a complete

discussion of these will appear elsewhere.

At higher observation frequencies, e.g., 345 GHz, the reduced impact of scattering results in nearly exact mitigation out to baseline lengths of $\sim 50\,\mathrm{G}\lambda$ and within the 25-epoch sampling variance for baseline lengths up to $\sim 100\,\mathrm{G}\lambda$. Thus it is possible to effectively mitigate interstellar scattering on baselines relevant for space-based mm-VLBI concepts that place stations in low and medium Earth orbits (2,000 km and <35,000 km, respectively), and accurately probing the magnetic field power spectrum on scales as small as $2\,\mu$as and thus a quarter of the Schwarzschild radius in Sgr A*.

Finally, however, the interpretation of the power spectrum ratio curves would require access to large number of converged GRMHD simulations. A primitive test with limited number of simulations show a weak correlation between the profile of the curve and the inclination angle, as well as the spins. A better understanding of the power spectrum ratios would be crucial in understanding the underlying physics of the turbulence structure in the vicinity of Sgr A*, especially with the upcoming observations with better equipment and higher sensitivity.

Chapter 4

Summaries of Conclusions

We demonstrate the value of polarization to probe physics near the vicinity of black hole and in the AGN jet. The EHT, a global VLBI collaboration with intercontinental baselines and wide bandwidths, has achieved unprecedented high resolution for the observation of black holes and AGNs. This dissertation has articulated how polarization can be used to mitigate scattering and extract turbulence information from the accretion flow near Sgr A*, and to constraint the jet properties of Cen A.

In Chapter 2, the detailed study of Cen A using the EHT 2017 data has yielded new insights into the structure and dynamics of AGN jets. The high-resolution total intensity imaging has uncovered the detailed emission regions in the Cen A jet. We find significant differences compared with past publication in Janssen et al. (2021), partly due to the sparse $(u, v)-$coverage presented in the dataset. We identify consistent structures of Cen A jet and counterjet, and quantify their brightness. The brightness ratio, infers the inclination angle and velocity of the jet, consistent with past publications (Hardcastle et al., 2003; Tingay et al., 1998). Further more, the polarimetric study of Cen A produces the first ever linear polarization map of Cen A down to 200 gravitational radii of its launching region. The linear polarization imaging shows ordered magnetic field structures within the jet. The analysis of the polarization fraction and the EVPA in different regions of the jet gives an estimate on the jet properties. We estimate the magnetic field is around 60 G and the electron density is around $3 \times 10^4 \mathrm{cm}^3$ at 660 R_g for Cen A, by adopting a phenomenological model inspired by Blandford & Znajek (1977). We also estimate the jet velocity to be under 0.2 c, agreeing with past publications in Tingay et al. (1998); Hardcastle et al. (2003).

Moreover, the method used to generate Cen A images is cutting-edge. When performing the fully self-consistent image model selection, Bayesian imaging has proved to

be able to robustly generate total intensity and linear polarization structures with very challenging datasets. We identify several difficulties with the dataset. These include poor $(u, v)-$coverage, presence of large-scale structure, and station-specific observing problems (e.g., pointing issues at the LMT). Nevertheless, Bayesian imaging produces a measure of the uncertainty in the reconstructions, and we present the range of possible images of Cen A, despite the data issues. High-qualities images are found to the EHT data, and the image posteriors provide a satisfactory representation of simulated datasets. The imaging of Cen A showcases the capability of Bayesian imaging to study celestial targets, even in the face of challenging data sets.

In Chapter 3, the development and implementation of a novel scattering mitigation scheme for Sgr A* have enabled a direct assessment of turbulence within the black hole accretion flow in the Galactic center, free from small structures introduced by interstellar scattering. This scheme has allowed us to penetrate the veil of interstellar scattering, without detailed modeling of the scattering screen itself. Consequently, we are able to directly retrieve information about the power spectrum of the turbulence in the accretion based on numerical experiments with GRMHD simulations, up to the resolution limits set by the Earth-bound baselines. These successes provide an opportunity for future observations of Sgr A*; by applying this methodology, we will be able to advance our understanding of how magnetic fields and instabilities influence the accretion procedure.

The findings here set the stage for future explorations. More specifically, future observations of Cen A would be able to provide better telescope coverage, filling the cavities in the $(u, v)-$space, which would drastically improve the data quality for Cen A. A simultaneous multi-frequency observation of Cen A would also be very helpful in filling out the $(u, v)-$space. These changes are imminent within the coming decade, as part of plan for the ngEHT. On the other hand, for mitigating scattering and retrieving turbulence information, an accumulative amount of data would shrink the size of the error bars drastically. Currently, we only have a few days of observations of Sgr A* from the EHT, with which we are unable to produce meaningful results. Multi-frequency observation, in the case of scattering, plays an even more important role, where scattering is wavelength-dependent. If observing at higher frequencies, the most probable of which is at 345 GHz, the scattering-free turbulence information we will be able to assess goes beyond the Earth-bound baselines.

Employing Bayesian methods for imaging Cen A has also accumulated experience that can be applied to the imaging of other AGNs. The robustness of Bayesian imaging techniques has been demonstrated through their capability to detect weak polarization signals with a challenging dataset. As the EHT and the ngEHT shall make observations of other AGNs in the future, Bayesian methods will facilitate similar polarization analyses. This

will enable more detailed analysis across a broader collection of AGNs, thereby enhancing our overall capability to probe the physics of these astronomical objects.

On the other hand, understanding the physical meanings behind the power spectrum ratios shall be the next step for probing the turbulence structure in the accretion disk, while we wait for future observations of Sgr A*. Due to the current limitations of GRMHD simulations, we are unable to draw definite conclusions on the correlation between physical quantities (e.g., spins, inclination angle, and other plasma properties in the accretion disk) and the shape of the power spectra ratio curves. However, more long and converged simulations will make the physical interpretation possible, hence provides better physical understand of the magnetic turbulence in the accretion disk.

This work, therefore, for contemporary and future astrophysical research, offers a robust framework for the continued exploration of some of the most mysterious and dynamic systems in our universe.

References

Abbott, R., Abbott, T. D., Abraham, S., et al. 2020, Phys. Rev. Lett., 125, 101102, doi: 10.1103/PhysRevLett.125.101102

Agol, E. 1997, PhD thesis, University of California, Santa Barbara

Antonucci, R. 1993, ARA&A, 31, 473, doi: 10.1146/annurev.aa.31.090193.002353

Armstrong, J. W., Rickett, B. J., & Spangler, S. R. 1995, ApJ, 443, 209, doi: 10.1086/175515

Asada, K., Inoue, M., Kameno, S., & Nagai, H. 2008, ApJ, 675, 79, doi: 10.1086/524000

Balbus, S. A., & Hawley, J. F. 1991, ApJ, 376, 214, doi: 10.1086/170270

—. 1998, Reviews of Modern Physics, 70, 1, doi: 10.1103/RevModPhys.70.1

Bare, C., Clark, B. G., Kellermann, K. I., Cohen, M. H., & Jauncey, D. L. 1967, Science, 157, 189, doi: 10.1126/science.157.3785.189

Blackburn, L., Chan, C.-k., Crew, G. B., et al. 2019, ApJ, 882, 23, doi: 10.3847/1538-4357/ab328d

Blandford, R. D., & Begelman, M. C. 1999, MNRAS, 303, L1, doi: 10.1046/j.1365-8711.1999.02358.x

Blandford, R. D., & Königl, A. 1979, ApJ, 232, 34, doi: 10.1086/157262

Blandford, R. D., & Payne, D. G. 1982, MNRAS, 199, 883, doi: 10.1093/mnras/199.4.883

Blandford, R. D., & Znajek, R. L. 1977, MNRAS, 179, 433, doi: 10.1093/mnras/179.3.433

Blumenthal, G. R., & Gould, R. J. 1970, Reviews of Modern Physics, 42, 237, doi: 10.1103/RevModPhys.42.237

Boehle, A., Ghez, A. M., Schödel, R., et al. 2016, ApJ, 830, 17, doi: 10.3847/0004-637X/830/1/17

Borkar, A., Adhikari, T. P., Różańska, A., et al. 2021, MNRAS, 500, 3536, doi: 10.1093/mnras/staa3515

Bower, G. C., Deller, A., Demorest, P., et al. 2014, ApJ, 780, L2, doi: 10.1088/2041-8205/780/1/L2

Brentjens, M. A., & de Bruyn, A. G. 2005, A&A, 441, 1217, doi: 10.1051/0004-6361:20052990

Bridle, A. H., & Perley, R. A. 1984, ARA&A, 22, 319, doi: 10.1146/annurev.aa.22.090184.001535

Broderick, A. E., & Blandford, R. D. 2004, in American Astronomical Society Meeting Abstracts, Vol. 205, American Astronomical Society Meeting Abstracts, 74.02

Broderick, A. E., Fish, V. L., Doeleman, S. S., & Loeb, A. 2011, ApJ, 735, 110, doi: 10.1088/0004-637X/735/2/110

Broderick, A. E., & Loeb, A. 2009a, ApJ, 697, 1164, doi: 10.1088/0004-637X/697/2/1164

—. 2009b, ApJ, 703, L104, doi: 10.1088/0004-637X/703/2/L104

Broderick, A. E., Pesce, D. W., Tiede, P., Pu, H.-Y., & Gold, R. 2020a, ApJ, 898, 9, doi: 10.3847/1538-4357/ab9c1f

Broderick, A. E., Gold, R., Karami, M., et al. 2020b, ApJ, 897, 139, doi: 10.3847/1538-4357/ab91a4

Broten, N. W., Legg, T. H., Locke, J. L., et al. 1967, Science, 156, 1592, doi: 10.1126/science.156.3782.1592

Brown, G. W., Carr, T. D., & Block, W. F. 1968, Astrophys. Lett., 1, 89

Burn, B. J. 1966, MNRAS, 133, 67, doi: 10.1093/mnras/133.1.67

Burns, J. O., Feigelson, E. D., & Schreier, E. J. 1983, ApJ, 273, 128, doi: 10.1086/161353

Burrows, A., & Vartanyan, D. 2021, Nature, 589, 29, doi: 10.1038/s41586-020-03059-w

Cappellari, M., Neumayer, N., Reunanen, J., et al. 2009, MNRAS, 394, 660, doi: 10.1111/j.1365-2966.2008.14377.x

Carr, B., Kohri, K., Sendouda, Y., & Yokoyama, J. 2021, Reports on Progress in Physics, 84, 116902, doi: 10.1088/1361-6633/ac1e31

Carr, B. J., Clesse, S., García-Bellido, J., Hawkins, M. R. S., & Kühnel, F. 2024, Phys. Rep., 1054, 1, doi: 10.1016/j.physrep.2023.11.005

Chael, A., kwan Chan, C., klbouman, et al. 2022, achael/eht-imaging: v1.2.4, v1.2.4, Zenodo, doi: 10.5281/zenodo.6519440

Chael, A. A., Johnson, M. D., Bouman, K. L., et al. 2018, ApJ, 857, 23, doi: 10.3847/1538-4357/aab6a8

Cho, I., Zhao, G.-Y., Kawashima, T., et al. 2021, arXiv e-prints, arXiv:2112.04929. https://arxiv.org/abs/2112.04929

Clarke, D. A., Burns, J. O., & Norman, M. L. 1992, ApJ, 395, 444, doi: 10.1086/171663

Cordes, J. M., & Lazio, T. J. W. 2002, arXiv e-prints, astro. https://arxiv.org/abs/astro-ph/0207156

Deller, A. T., Brisken, W. F., Phillips, C. J., et al. 2011, PASP, 123, 275, doi: 10.1086/658907

Doeleman, S. S., Weintroub, J., Rogers, A. E. E., et al. 2008, Nature, 455, 78, doi: 10.1038/nature07245

Doeleman, S. S., Barrett, J., Blackburn, L., et al. 2023, Galaxies, 11, 107, doi: 10.3390/galaxies11050107

Draine, B. T., & Lazarian, A. 1998, ApJ, 508, 157, doi: 10.1086/306387

Edge, D. O., Shakeshaft, J. R., McAdam, W. B., Baldwin, J. E., & Archer, S. 1959, MmRAS, 68, 37

Einstein, A. 1916, Annalen der Physik, 354, 769, doi: 10.1002/andp.19163540702

Enßlin, T. A., & Vogt, C. 2003, A&A, 401, 835, doi: 10.1051/0004-6361:20030172

Espada, D., Matsushita, S., Miura, R. E., et al. 2017, ApJ, 843, 136, doi: 10.3847/1538-4357/aa78a9

Event Horizon Telescope Collaboration, Akiyama, K., Alberdi, A., et al. 2019a, ApJ, 875, L1, (m87 Paper I), doi: 10.3847/2041-8213/ab0ec7

—. 2019b, ApJ, 875, L6, (m87 Paper VI), doi: 10.3847/2041-8213/ab1141

—. 2019c, ApJ, 875, L2, (m87 Paper II), doi: 10.3847/2041-8213/ab0c96

—. 2019d, ApJ, 875, L1, doi: 10.3847/2041-8213/ab0ec7

—. 2019e, ApJ, 875, L2, doi: 10.3847/2041-8213/ab0c96

—. 2019f, ApJ, 875, L3, doi: 10.3847/2041-8213/ab0c57

—. 2019g, ApJ, 875, L4, doi: 10.3847/2041-8213/ab0e85

—. 2019h, ApJ, 875, L5, doi: 10.3847/2041-8213/ab0f43

—. 2019i, ApJ, 875, L6, doi: 10.3847/2041-8213/ab1141

—. 2019j, ApJ, 875, L3, (m87 Paper III), doi: 10.3847/2041-8213/ab0c57

—. 2019k, ApJ, 875, L4, (m87 Paper IV), doi: 10.3847/2041-8213/ab0e85

—. 2019l, ApJ, 875, L5, (m87 Paper V), doi: 10.3847/2041-8213/ab0f43

—. 2021a, ApJ, 910, L12, (m87 Paper VII), doi: 10.3847/2041-8213/abe71d

—. 2021b, ApJ, 910, L13, (m87 Paper VIII), doi: 10.3847/2041-8213/abe4de

—. 2022a, ApJ, 930, L12, doi: 10.3847/2041-8213/ac6674

—. 2022b, ApJ, 930, L14, doi: 10.3847/2041-8213/ac6429

—. 2022c, ApJ, 930, L15, doi: 10.3847/2041-8213/ac6736

—. 2022d, ApJ, 930, L13, doi: 10.3847/2041-8213/ac6675

—. 2022e, ApJ, 930, L16, doi: 10.3847/2041-8213/ac6672

—. 2022f, ApJ, 930, L17, doi: 10.3847/2041-8213/ac6756

—. 2024a, ApJ, 964, L25, doi: 10.3847/2041-8213/ad2df0

—. 2024b, ApJ, 964, L26, doi: 10.3847/2041-8213/ad2df1

Fabian, A. C. 2012, ARA&A, 50, 455, doi: 10.1146/annurev-astro-081811-125521

Fanaroff, B. L., & Riley, J. M. 1974, MNRAS, 167, 31P, doi: 10.1093/mnras/167.1.31P

Feain, I. J., Ekers, R. D., Murphy, T., et al. 2009, ApJ, 707, 114, doi: 10.1088/0004-637X/707/1/114

Feain, I. J., Cornwell, T. J., Ekers, R. D., et al. 2011, ApJ, 740, 17, doi: 10.1088/0004-637X/740/1/17

Ferrarese, L., & Merritt, D. 2000, ApJ, 539, L9, doi: 10.1086/312838

Fish, V. L., Johnson, M. D., Lu, R.-S., et al. 2014, ApJ, 795, 134, doi: 10.1088/0004-637X/795/2/134

Frail, D. A., Diamond, P. J., Cordes, J. M., & van Langevelde, H. J. 1994, ApJ, 427, L43, doi: 10.1086/187360

Fuentes, A., Gomez, J., Martí, J. M., et al. 2022

Gabuzda, D. C., Murray, É., & Cronin, P. 2004, MNRAS, 351, L89, doi: 10.1111/j.1365-2966.2004.08037.x

Gardner, F. F., & Whiteoak, J. B. 1966, ARA&A, 4, 245, doi: 10.1146/annurev.aa.04.090166.001333

Georgiev, B., Pesce, D. W., Broderick, A. E., et al. 2022, ApJ, 930, L20, doi: 10.3847/2041-8213/ac65eb

Ghez, A. M., Salim, S., Weinberg, N. N., et al. 2008, ApJ, 689, 1044, doi: 10.1086/592738

Gillessen, S., Eisenhauer, F., Trippe, S., et al. 2009, The Astrophysical Journal, 692, 1075. http://stacks.iop.org/0004-637X/692/i=2/a=1075

Goddi, C., Martí-Vidal, I., Messias, H., et al. 2021, ApJ, 910, L14, doi: 10.3847/2041-8213/abee6a

Gold, R., McKinney, J. C., Johnson, M. D., & Doeleman, S. S. 2017, Astrophys. J., 837, 180, doi: 10.3847/1538-4357/aa6193

Goldreich, P., & Kylafis, N. D. 1981, ApJ, 243, L75, doi: 10.1086/183446

Goldreich, P., & Sridhar, S. 1995, ApJ, 438, 763, doi: 10.1086/175121

Gravity Collaboration, Abuter, R., Amorim, A., et al. 2018, VizieR Online Data Catalog, J/A+A/618/L10

Hardcastle, M. J., Worrall, D. M., Kraft, R. P., et al. 2003, ApJ, 593, 169, doi: 10.1086/376519

Harris, G. L. H., Rejkuba, M., & Harris, W. E. 2010, PASA, 27, 457, doi: 10.1071/AS09061

Haslam, C. G. T., Salter, C. J., Stoffel, H., & Wilson, W. E. 1982, A&AS, 47, 1

Homan, D. C., & Lister, M. L. 2006, AJ, 131, 1262, doi: 10.1086/500256

Hovatta, T., O'Sullivan, S., Martí-Vidal, I., Savolainen, T., & Tchekhovskoy, A. 2019, A&A, 623, A111, doi: 10.1051/0004-6361/201832587

Israel, W. 1967, Physical Review, 164, 1776, doi: 10.1103/PhysRev.164.1776

Issaoun, S., Johnson, M. D., Blackburn, L., et al. 2021, arXiv e-prints, arXiv:2104.07610. https://arxiv.org/abs/2104.07610

Issaoun, S., Wielgus, M., Jorstad, S., et al. 2022, ApJ, 934, 145, doi: 10.3847/1538-4357/ac7a40

Janssen, M., Goddi, C., van Bemmel, I. M., et al. 2019, A&A, 626, A75, doi: 10.1051/0004-6361/201935181

Janssen, M., Falcke, H., Kadler, M., et al. 2021, Nature Astronomy, 5, 1017, doi: 10.1038/s41550-021-01417-w

Johnson, M. D. 2016, ApJ, 833, 74, doi: 10.3847/1538-4357/833/1/74

Johnson, M. D., & Gwinn, C. R. 2015, ApJ, 805, 180, doi: 10.1088/0004-637X/805/2/180

Johnson, M. D., & Narayan, R. 2016, ApJ, 826, 170, doi: 10.3847/0004-637X/826/2/170

Johnson, M. D., Fish, V. L., Doeleman, S. S., et al. 2015a, Science, 350, 1242, doi: 10.1126/science.aac7087

—. 2015b, Science, 350, 1242, doi: 10.1126/science.aac7087

Johnson, M. D., et al. 2015, Science, 350, 1242, doi: 10.1126/science.aac7087

Johnson, M. D., Narayan, R., Psaltis, D., et al. 2018, ApJ, 865, 104, doi: 10.3847/1538-4357/aadcff

Jones, R. C. 1941, Journal of the Optical Society of America (1917-1983), 31, 488, doi: 10.1364/JOSA.31.000488

Jones, T. W., & O'Dell, S. L. 1977, ApJ, 214, 522, doi: 10.1086/155278

Jorstad, S., Wielgus, M., Lico, R., et al. 2023, ApJ, 943, 170, doi: 10.3847/1538-4357/acaea8

Kerr, R. P. 1963, Phys. Rev. Lett., 11, 237, doi: 10.1103/PhysRevLett.11.237

Kim, J.-Y., Krichbaum, T. P., Broderick, A. E., et al. 2020, A&A, 640, A69, doi: 10.1051/0004-6361/202037493

Kormendy, J., & Richstone, D. 1995, ARA&A, 33, 581, doi: 10.1146/annurev.aa.33.090195.003053

Kraft, R. P., Forman, W. R., Jones, C., et al. 2002, ApJ, 569, 54, doi: 10.1086/339062

Krawczynski, H., Muleri, F., Dovčiak, M., et al. 2022, Science, 378, 650, doi: 10.1126/science.add5399

Lazio, T. J. W., & Cordes, J. M. 1998a, ApJS, 118, 201, doi: 10.1086/313129

—. 1998b, ApJ, 505, 715, doi: 10.1086/306174

Lo, K. Y., Shen, Z.-Q., Zhao, J.-H., & Ho, P. T. P. 1998, ApJ, 508, L61, doi: 10.1086/311726

Lu, R.-S., Krichbaum, T. P., Roy, A. L., et al. 2018, ApJ, 859, 60, doi: 10.3847/1538-4357/aabe2e

Lynden-Bell, D. 1969, Nature, 223, 690, doi: 10.1038/223690a0

Lyutikov, M., Pariev, V. I., & Gabuzda, D. C. 2005, MNRAS, 360, 869, doi: 10.1111/j.1365-2966.2005.08954.x

Lyutikov, M., Temim, T., Komissarov, S., et al. 2019, MNRAS, 489, 2403, doi: 10.1093/mnras/stz2023

Macquart, J. P., & Melrose, D. B. 2000, ApJ, 545, 798, doi: 10.1086/317852

Matveenko, L. I., Kardashev, N. S., & Sholomitskii, G. B. 1965, Radiophysics and Quantum Electronics, 8, 461, doi: 10.1007/BF01038318

McNamara, B. R., & Nulsen, P. E. J. 2012, New Journal of Physics, 14, 055023, doi: 10.1088/1367-2630/14/5/055023

Miller, M. C., & Colbert, E. J. M. 2004, International Journal of Modern Physics D, 13, 1, doi: 10.1142/S0218271804004426

Mingo, B., Croston, J. H., Hardcastle, M. J., et al. 2019, MNRAS, 488, 2701, doi: 10.1093/mnras/stz1901

Misner, C. W., Thorne, K. S., & Wheeler, J. A. 1973, Gravitation

Mo, H., van den Bosch, F. C., & White, S. 2010, Galaxy Formation and Evolution

Moran, J. M. 1998, in Astronomical Society of the Pacific Conference Series, Vol. 144, IAU Colloq. 164: Radio Emission from Galactic and Extragalactic Compact Sources, ed. J. A. Zensus, G. B. Taylor, & J. M. Wrobel, 1

Moran, J. M., Crowther, P. P., Burke, B. F., et al. 1967, Science, 157, 676, doi: 10.1126/science.157.3789.676

Müller, C., Kadler, M., Ojha, R., et al. 2011, A&A, 530, L11, doi: 10.1051/0004-6361/201116605

—. 2014, A&A, 569, A115, doi: 10.1051/0004-6361/201423948

Narayan, R. 1992, Philosophical Transactions of the Royal Society of London Series A, 341, 151, doi: 10.1098/rsta.1992.0090

Narayan, R., & Yi, I. 1994, ApJ, 428, L13, doi: 10.1086/187381

Ni, C., Broderick, A. E., & Gold, R. 2022, ApJ, 940, 149, doi: 10.3847/1538-4357/ac9b47

O'Sullivan, S. P., Feain, I. J., McClure-Griffiths, N. M., et al. 2013, ApJ, 764, 162, doi: 10.1088/0004-637X/764/2/162

Palumbo, D. C. M., Wong, G. N., & Prather, B. S. 2020, ApJ, 894, 156, doi: 10.3847/1538-4357/ab86ac

Park, J., Hada, K., Kino, M., et al. 2019, ApJ, 871, 257, doi: 10.3847/1538-4357/aaf9a9

Pen, U.-L., & Levin, Y. 2014, MNRAS, 442, 3338, doi: 10.1093/mnras/stu1020

Piran, T., & Stark, R. F. 1986, in Dynamical Spacetimes and Numerical Relativity, ed. J. M. Centrella, 40

Psaltis, D., Johnson, M., Narayan, R., et al. 2018, arXiv e-prints, arXiv:1805.01242. https://arxiv.org/abs/1805.01242

Qiu, R., Ricarte, A., Narayan, R., et al. 2023, MNRAS, 520, 4867, doi: 10.1093/mnras/stad466

Raymond, A. W., Palumbo, D., Paine, S. N., et al. 2021, ApJS, 253, 5, doi: 10.3847/1538-3881/abc3c3

Rees, M. J. 1984, ARA&A, 22, 471, doi: 10.1146/annurev.aa.22.090184.002351

Remazeilles, M., Dickinson, C., Banday, A. J., Bigot-Sazy, M. A., & Ghosh, T. 2015, MNRAS, 451, 4311, doi: 10.1093/mnras/stv1274

Rickett, B. J. 1990, ARA&A, 28, 561, doi: 10.1146/annurev.aa.28.090190.003021

Rybicki, G. B., & Lightman, A. P. 1986, Radiative Processes in Astrophysics

Schwarzschild, K. 1916, Abh. Konigl. Preuss. Akad. Wissenschaften Jahre 1906,92, Berlin,1907, 1916, 189

Seyfert, C. K. 1943, ApJ, 97, 28, doi: 10.1086/144488

Shakura, N. I., & Sunyaev, R. A. 1973, A&A, 24, 337

Silk, J., & Rees, M. J. 1998, A&A, 331, L1, doi: 10.48550/arXiv.astro-ph/9801013

Syed, S., Bouchard-Côté, A., Deligiannidis, G., & Doucet, A. 2021, Journal of the Royal Statistical Society Series B: Statistical Methodology, 84, 321, doi: 10.1111/rssb.12464

Thompson, A. R., Moran, J. M., & Swenson, George W., J. 2001, Interferometry and Synthesis in Radio Astronomy, 2nd Edition

Tingay, S. J., Jauncey, D. L., Reynolds, J. E., et al. 1998, AJ, 115, 960, doi: 10.1086/300257

Urry, C. M. 2003, in American Astronomical Society Meeting Abstracts, Vol. 202, American Astronomical Society Meeting Abstracts #202, 22.01

Wardle, J. F. C., & Kronberg, P. P. 1974, ApJ, 194, 249, doi: 10.1086/153240

Wielgus, M., Palumbo, D., & Hamilton, L. 2020, LCG metric, https://github.com/wielgusm/mwtools/blob/master/LCG_metric.py, GitHub

Wielgus, M., Akiyama, K., Blackburn, L., et al. 2020, ApJ, 901, 67, doi: 10.3847/1538-4357/abac0d

Yuan, F., & Narayan, R. 2014, ARA&A, 52, 529, doi: 10.1146/annurev-astro-082812-141003

Yuan, F., Quataert, E., & Narayan, R. 2003, ApJ, 598, 301, doi: 10.1086/378716

Zavala, R. T., & Taylor, G. B. 2002, ApJ, 566, L9, doi: 10.1086/339441

—. 2003, ApJ, 589, 126, doi: 10.1086/374619

APPENDICES

Appendix A

Cen A

A.1 Raster Survey for the Themis models

The limited $(u, v)-$coverage for Cen A restricts the capability to examine structures in areas without any detection. As a result, achieving "super resolution" necessitates model fitting and parameter adjustments for all image reconstruction techniques. For THEMIS, to ensure the model's precision and to avoid potential model misspecification, it is crucial to determine the number of control points and the raster's geometry. As mentioned in Section 2.4.1, we first optimize the potential models against the EHT data, and then perform THEMIS fitting to all the models that have similar good performances after optimizing.

To address the optimization, we undertake a data-driven raster examination, using Limited-memory Broyden-Fletcher-Goldfarb-Shanno (L-BFGS) optimizing algorithm, which is an iterative method for solving unconstrained nonlinear optimization problems, and it is a quasi-Newton method. It holds a plethora of advantages when optimizing problems like Cen A, the most prominent of which is that it is suitable for problems with a large number of variables thanks to its memory-efficiency. Applying L-BFGS algorithm to a collection of different raster models, we then calculate and compare the Bayesian Information Criteria (BIC) from Equation 2.3.

After optimization, a multitude of morphologies are found, which are shown in Figure A.2. In general, the limb brightening feature of the jet is visible, but there are raster models that fail to capture it. This further indicates complexity of the likelihood space of Cen A. The BIC values for each model is calculated and plotted in Figure A.1, where the BICs show a V-shape, with high BICs when the total number of parameters are either

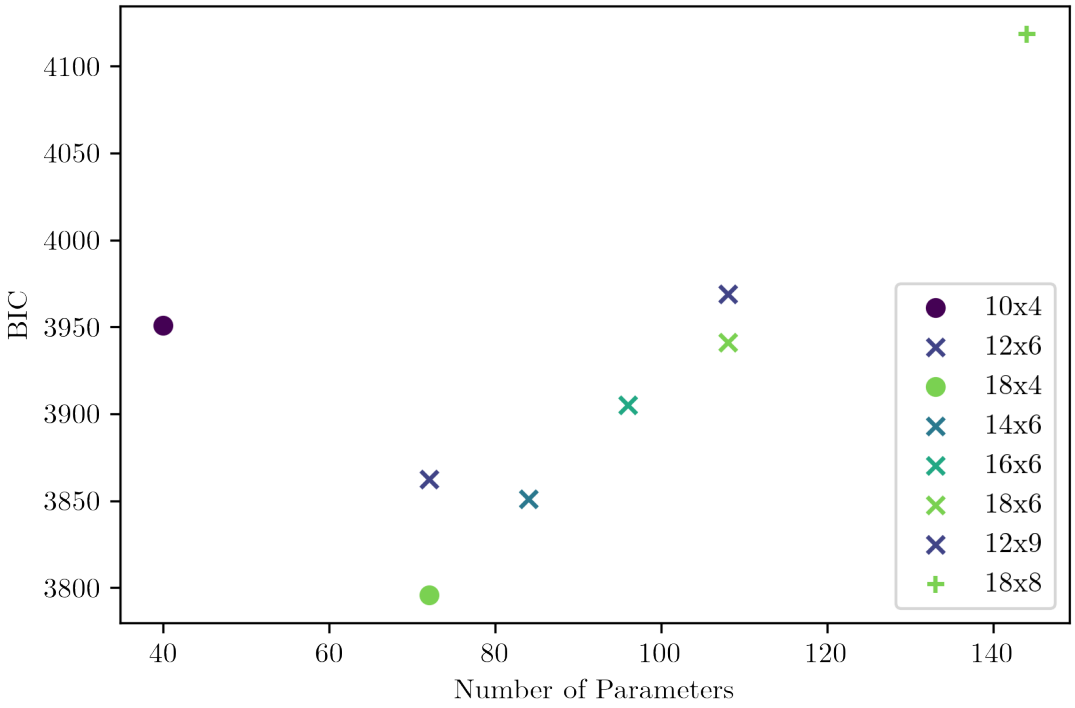

Figure A.1: The BIC values for different raster models after optimization against the total number of parameters. Dots/crosses/plus signs represent the rasters whose width has 4/6/8 pixels. Colors (from purple to green) represent the rasters whose length has from 10 to 18 pixels.

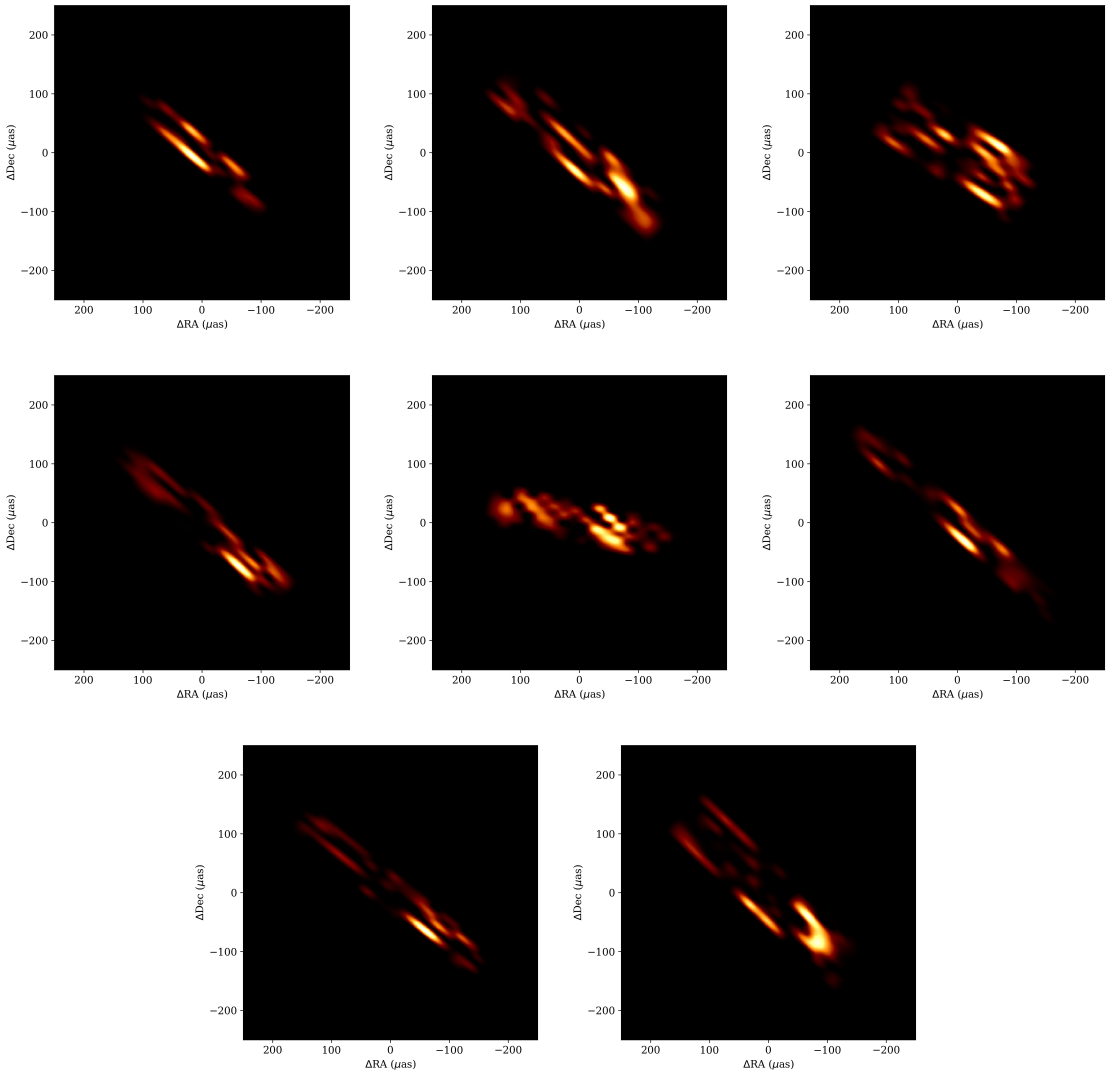

Figure A.2: The results from optimizing for different raster models to the high band data. From left to right, top to bottom are rasters of size 10 by 4, 12 by 6, 12 by 9, 14 by 6, 16 by 6, 18 by 4 18 by 6 and 18 by 8.

too small or too large. This is expected, as the model is not enough to cover the large structure when the number of parameter is too small, and it is punished when the number of parameter is too large. However, during optimizing, the MCMC walker can be trapped within the local maxima without enough time to find the global maxima in the likelihood space. This is problematic at the bottom of the "valley", where the BIC values are actually very close to each other. Therefore, To more closely examine and break the degeneracy of these models, we carry out full THEMIS runs and directly compare the Bayesian evidence, which we have discussed in Section 2.4.1 and in Section 2.4.3.

Appendix B

Scattering Mitigation

B.1 Deflection Angle vs Phase Change Caused for Different Polarization Modes

The scattering screen can be envisioned as a screen of width $L_{\parallel}$ comprised of many electron bubbles, which have typical size of $L_{\perp}$. When a photon travels travels through the scattering screen, each bubble causes a slight deflection to the photon's trajectory. After averaging the photon deflection angle over the width of the scattering screen, we should be able to derive the root-mean-squared deflection angle as a function of the width.

Therefore, after integrating through the line-of-sight direction of the screen and the typical size of the bubbles. The argument is also valid for the phase change caused by the scattering screen, as the deflection angle and the phase change are linearly correlated. Next, we are going to consider two different scenarios, where the auto-correlation function of the electron density and the magnetic field takes different forms.

B.1.1 Difference in the Deflection Angles for Different Polarization Modes

We have shown in the Section 3.2.2 that the difference in the deflection angles and the phase changes for different polarization modes can be written as an integral over functions of the magnetic field and the electron density field, as

$$\delta\theta = |\theta_+ - \theta_-| = \int dz \nabla_{\mathbf{r}} (XY) \,, \tag{B.1}$$

$$\delta\phi = \frac{\omega}{c}\int dzXY. \tag{B.2}$$

In this appendix, we will explore the properties of $\delta\theta$ and $\delta\phi$, given different fluctuations of the electron density fields and the magnetic fields.

We assume that X and Y, the fluctuation electron density field and the magnetic field, are some independent Gaussian random fields. For the electron density field, it has mean value X_0, while for magnetic field the mean value is zero. Decomposing X and Y into Fourier modes with cylindrical coordinate system, we have

$$X\left(\mathbf{r},z\right) = X_0 + \int d\mathbf{q}dma_{\mathbf{q},m}e^{[i(\mathbf{q}\cdot\mathbf{r}+mz)]}, \tag{B.3}$$

$$Y\left(\mathbf{r},z\right) = \int d\mathbf{q}dmb_{\mathbf{q},m}e^{[i(\mathbf{q}\cdot\mathbf{r}+mz)]}, \tag{B.4}$$

where $\mathbf{q}$ and $\mathbf{r}$ are the Fourier conjugate in the cylindrical plane, and m and z are conjugate in the axial direction.

The power spectra for the two Gaussian random fields are defined as:

$$\langle a_{q_1,m_1}a^*_{q_2,m_2}\rangle = P\left(q_1,m_1\right)\delta\left(q_1-q_2\right)\delta\left(m_1-m_2\right) \tag{B.5}$$

$$\langle b_{\mathbf{q}_1,m_1}b^*_{\mathbf{q}_2,m_2}\rangle = Q\left(\mathbf{q}_1,m_1\right)\delta\left(\mathbf{q}_1-\mathbf{q}_2\right)\delta\left(m_1-m_2\right). \tag{B.6}$$

The independence of the two fields require the Fourier coefficients $a_{\mathbf{q},m}$ and $b_{\mathbf{q},m}$ to satisfy $\langle a_{\mathbf{q}_1,m_1}b^*_{\mathbf{q}_2,m_2}\rangle = 0$.

For simplicity, from here on in this appendix, we will use prime to denote the derivative in the radial direction, e.g. $Y' = \partial Y/\partial r$.

Inserting the fields X and Y expanded in the Fourier domain back to Equation B.1, and taking the ensemble average, we have

$$\begin{aligned}\langle\delta\theta\rangle &= \int dz\langle X'Y + \left(X-X_0\right)Y' + X_0Y'\rangle \\ &= i\int dz\int d\mathbf{q}_{1,2}dm_{1,2}(\mathbf{q}_1-\mathbf{q}_2) \\ &\times\langle a_{\mathbf{q}_1,m_1}b^*_{\mathbf{q}_2,m_2}\rangle e^{i[(\mathbf{q}_1-\mathbf{q}_2)\cdot\mathbf{r}+(m_1-m_2)z]}.\end{aligned} \tag{B.7}$$

A quick check can be done that because $a_{\mathbf{q},m}$ and $b_{\mathbf{q},m}$ to satisfy $\langle a_{\mathbf{q}_1,m_1}b^*_{\mathbf{q}_2,m_2}\rangle = 0$, the average of $\delta\theta$ is zero.

Similarly, we can insert Equation B.3 and Equation B.4 into $\langle \delta\theta^2 \rangle$, which takes the form

$$\langle \delta\theta^2 \rangle = \int dz_1 dz_2 \langle \left(X_1' Y_1 + X_1 Y_1'\right) \left(X_2' Y_2 + X_2 Y_2'\right) \rangle, \tag{B.8}$$

where the subscripts 1 and 2 of X and Y denote z_1 and z_2 dependence of X and Y, and the subscripts 1, 2, 3 and 4 of $\mathbf{q}$ and m denote different realizations of the Gaussian random fields.

The integrand above can be divided into nine different terms, as

$$\langle \delta\theta^2 \rangle = \int dz_1 dz_2 \langle \left(X_1' Y_1 + \left(X_1 - X_0\right) Y_1' + X_0 Y_1'\right) \times \left(X_2' Y_2 + \left(X_2 - X_0\right) Y_2' + X_0 Y_2'\right) \rangle. \tag{B.9}$$

Each nine components of the integral can be done independently using the identities Equation B.5 and Equation B.6.

The first term is:

$$\langle X_1' Y_1 Y_2^* X_2'^* \rangle = \int d\mathbf{q}_1 dm_1 d\mathbf{q}_2 dm_2 P\left(\mathbf{q}_1, m_1\right) \times Q\left(\mathbf{q}_2, m_2\right) \mathbf{q}_1^2 e^{i(m_1+m_2)(z_1-z_2)}. \tag{B.10}$$

The second term is:

$$\langle X_1' Y_1 Y_2'^* \left(X_2 - X_0\right)^* \rangle = \int d\mathbf{q}_1 dm_1 d\mathbf{q}_2 dm_2 P\left(\mathbf{q}_1, m_1\right) Q\left(\mathbf{q}_2, m_2\right) \times \mathbf{q}_1 \cdot \mathbf{q}_2 e^{i(m_1+m_2)(z_1-z_2)}. \tag{B.11}$$

The third term is:

$$\langle \left(X_1 - X_0\right) Y_1' Y_2^* X_2'^* \rangle = \int d\mathbf{q}_1 dm_1 d\mathbf{q}_2 dm_2 P\left(\mathbf{q}_1, m_1\right) Q\left(\mathbf{q}_2, m_2\right) \times \mathbf{q}_1 \cdot \mathbf{q}_2 e^{i(m_1+m_2)(z_1-z_2)}. \tag{B.12}$$

The fourth term is:

$$\langle \left(X_1 - X_0\right) Y_1' Y_2'^* \left(X_2 - X_0\right)^* \rangle = \int d\mathbf{q}_1 dm_1 d\mathbf{q}_2 dm_2 P\left(\mathbf{q}_1, m_1\right) Q\left(\mathbf{q}_2, m_2\right) \times \mathbf{q}_2^2 e^{i(m_1+m_2)(z_1-z_2)}. \tag{B.13}$$

The fifth term is:

$$\langle X_0 Y_1' Y_2'^* X_0^* \rangle = X_0^2 \int d\mathbf{q} dm Q\left(\mathbf{q}, m\right) \mathbf{q}^2 e^{im(z_1-z_2)}. \tag{B.14}$$

The other four terms are zero, because $\langle a_{\mathbf{q}_1, m_1} b^*_{\mathbf{q}_2, m_2} \rangle = 0$.

Grouping nine terms together, we have

$$\begin{aligned}\langle \delta\theta^2 \rangle = \int dz_1 dz_2 \Bigg(\int d\mathbf{q}_1 dm_1 d\mathbf{q}_2 dm_2 \\ P\left(\mathbf{q}_1, m_1\right) Q\left(\mathbf{q}_2, m_2\right) \left(\mathbf{q}_1 + \mathbf{q}_2\right)^2 e^{i(m_1+m_2)(z_1-z_2)} \\ + X_0^2 \int d\mathbf{q} dm Q\left(\mathbf{q}, m\right) \mathbf{q}^2 e^{im(z_1-z_2)} \Bigg).\end{aligned} \tag{B.15}$$

We can define the auto-correlation function of fields X and Y to help simplifying Equation B.15:

$$C\left(\mathbf{r}, z\right) = \int d\mathbf{q} dm P\left(\mathbf{q}, m\right) e^{i(\mathbf{q}\cdot\mathbf{r}+mz)} \tag{B.16}$$

$$D\left(\mathbf{r}, z\right) = \int d\mathbf{q} dm Q\left(\mathbf{q}, m\right) e^{i(\mathbf{q}\cdot\mathbf{r}+mz)}. \tag{B.17}$$

At the line of sight, Equation B.15 can be evaluated with the auto-correlation functions $C\left(\mathbf{r}=0, z\right)$ and $D\left(\mathbf{r}=0, z\right)$:

$$\langle \delta\theta^2 \rangle = -\int dz_1 dz_2 \Big[C\left(\mathbf{r}, z_1 - z_2\right) D\left(\mathbf{r}, z_1 - z_2\right) + X_0^2 D\left(\mathbf{r}, z_1 - z_2\right) \Big]'' \Big|_{\mathbf{r}=0}. \tag{B.18}$$

Because the derivative is with respect of the perpendicular direction, and the integral is along the line-of-sight direction, derivative and integral can be switched:

$$\langle \delta\theta^2 \rangle = -\frac{\partial^2}{\partial r^2} \int dz_1 dz_2 \Big[C\left(\mathbf{r}, z_1 - z_2\right) D\left(\mathbf{r}, z_1 - z_2\right) + X_0^2 D\left(\mathbf{r}, z_1 - z_2\right) \Big] \Big|_{\mathbf{r}=0}. \tag{B.19}$$

B.1.2 Difference in Phase Changes for Different Polarization Modes

Similar to that Equation B.1 can be expanded in the Fourier space and expressed in the compact form of the auto-correlation functions, same can be done to Equation B.2.

First, the ensemble average of $\delta\phi$ is zero as expected:

$$\begin{aligned}\langle \delta\phi \rangle &= \frac{\omega}{c} \int dz d\mathbf{q}_1 dm_1 d\mathbf{q}_2 dm_2 e^{i[(\mathbf{q}_1-\mathbf{q}_2)\mathbf{r}+(m_1-m_2)z]} \\ &\times \left(\langle a_{\mathbf{q}_1,m_1} b_{\mathbf{q}_2,m_2} \rangle + X_0 \langle b_{\mathbf{q}_2,m_2} \rangle \right) \\ &= 0,\end{aligned} \tag{B.20}$$

given that $\langle a_{\mathbf{q}_1,m_1} b^*_{\mathbf{q}_2,m_2}\rangle = 0$.

Second, the variance is:

$$\begin{aligned}\langle \delta\phi^2\rangle = \left(\frac{\omega}{c}\right)^2 \int dz_1 dz_2 \Big[&\langle (X_1 - X_0)\, Y_1\, (X_2 - X_0)\, Y_2\rangle \\ &+ \langle (X_1 - X_0)\, Y_1 X_0 Y_2\rangle \\ &+ \langle X_0 Y_1\, (X_2 - X_0)\, Y_2\rangle \\ &+ \langle X_0 Y_1 X_0 Y_2\rangle \Big].\end{aligned} \tag{B.21}$$

Similar to Equation B.9, the integrand of $\langle \delta\phi^2\rangle$ can be broken into small components, whose detailed calculations are similar to the ones of $\langle \delta\theta^2\rangle$. In the end, we have

$$\begin{aligned}\langle \delta\phi^2\rangle = \left(\frac{\omega}{c}\right)^2 \int dz_1 dz_2 \Big[&\int d\mathbf{q}_1 dm_1 d\mathbf{q}_2 dm_2 \\ &P(\mathbf{q}_1, m_1)\, Q(\mathbf{q}_2, m_2)\, e^{i(m_1+m_2)(z_1-z_2)} \\ &+ X_0^2 \int d\mathbf{q}_2 dm_2 Q(\mathbf{q}, m)\, e^{im(z_1-z_2)} \Big].\end{aligned} \tag{B.22}$$

The equation above can be evaluated in the same way as we evaluate the variance of $\delta\theta$, with the help of the auto-correlation functions:

$$\langle \delta\phi^2\rangle = \left(\frac{\omega}{c}\right)^2 \int dz_1 dz_2 \Big[C(\mathbf{r}, z_1 - z_2)\, D(\mathbf{r}, z_1 - z_2) + X_0^2 D(\mathbf{r}, z_1 - z_2) \Big]_{\mathbf{r}=0}. \tag{B.23}$$

Compared to Equation B.19, the variance of $\delta\theta$ is proportional to the second order derivative of the variance of $\delta\phi$:

$$\begin{aligned}\langle \delta\theta^2\rangle &= \left(\frac{c}{\omega}\right)^2 \frac{\partial^2}{\partial r^2} \langle \delta\phi^2\rangle \\ &\approx \frac{\lambda^2}{L^2} \langle \delta\phi^2\rangle,\end{aligned} \tag{B.24}$$

where L is the typical correlation length within the plasma.

B.1.3 Explicit Examples and Quantitative Estimates

Quantitatively assessing the magnitude of the phase differences between the two polarization modes requires an explicit model for the density and magnetic field fluctuations

within the scattering screen. Because Equation B.19 and Equation B.23 depend only on the correlation functions of these underlying physical quantities, specifying the statistical properties of the density and magnetic field through their correlation functions is sufficient. Because these are not known a priori, we explore a handful of examples, beginning with a Gaussian correlation functions with a natural intrinsic scale, and culminating in the Kolmogorov models that are traditionally employed.

Gaussian Auto-correlation Functions

We first consider the simple case that the auto-correlation functions of the electron density, X, and the magnetic field, Y, are Gaussian. These have a clear scale, beyond which the correlation is exponentially suppressed. Both the Gaussian distributions have the standard deviation of $L_\perp$, which is the typical size of fluctuations in the electron density and magnetic field strength. Within each bubble, both the electron density and magnetic field fluctuations are highly correlated, while for different bubbles they are not. The auto-correlation functions are:

$$C\left(\mathbf{r}, z\right) = \sigma_X^2 e^{-\left(r^2+z^2\right)/2L_\perp^2}, \tag{B.25}$$

$$D\left(\mathbf{r}, z\right) = \sigma_Y^2 e^{-\left(r^2+z^2\right)/2L_\perp^2}, \tag{B.26}$$

where the corresponding variances σ_X and σ_Y are of order of one.

To estimate Equation B.23, we first make a change of variable:

$$\tilde{z_1} = z_1 - z_2 \tag{B.27}$$

$$\tilde{z_2} = z_1 + z_2, \tag{B.28}$$

in terms of which the variance in the phase fluctuations may be written with new upper and lower bounds:

$$\langle \delta\phi^2 \rangle = 2\left(\frac{\omega}{c}\right)^2 \int_0^{L_\parallel} d\tilde{z_1} \int_{\tilde{z_1}}^{2L_\parallel - \tilde{z_1}} d\tilde{z_2} \left(C\left(\tilde{z_1}\right) D\left(\tilde{z_1}\right) + X_0^2 D\left(\tilde{z_1}\right)\right) \tag{B.29}$$

Inserting the Gaussian correlation functions above, this becomes,

$$\begin{aligned} \langle \delta\phi^2 \rangle = 4\left(\frac{\omega}{c}\right)^2 \Bigg\{ & \sigma_X^2 \sigma_Y^2 \frac{L_\perp^2}{2} \Bigg[\left(\left(-1 + e^{-L_\parallel^2/L_\perp^2}\right) \right. \\ & \left. + \frac{L_\parallel}{L_\perp} \sqrt{\pi} \mathrm{erf}\left(\frac{L_\parallel}{L_\perp}\right) \right] + X_0^2 \sigma_Y^2 L_\perp^2 \Bigg[\left(\left(-1 + e^{-L_\parallel^2/2L_\perp^2}\right) \right. \\ & \left. + \frac{L_\parallel}{L_\perp} \sqrt{\frac{\pi}{2}} \mathrm{erf}\left(\frac{L_\parallel}{\sqrt{2} L_\perp}\right) \right) \Bigg] \Bigg\} \end{aligned} \tag{B.30}$$

The scattering screen is comprised of many electron bubbles along the line-of-sight, $L_\parallel/L_\perp \gg 1$. In this limit both erf $\left(L_\parallel/L_\perp\right)$ is approximately unity and exp $\left(-L_\parallel^2/L_\perp^2\right)$ is approximately zero. With these simplifications, the variance of $\delta\phi$ becomes,

$$\langle\delta\phi^2\rangle = 2\left(\frac{\omega}{c}\right)^2\sqrt{\pi}L_\parallel L_\perp\sigma_Y^2\left(\sigma_X^2+\sqrt{2}X_0^2\right) \tag{B.31}$$

Similarly, the variance of the deflection angle, Equation B.19, can be calculated given Equation B.25 and Equation B.26 in the limit that $L_\parallel/L_\perp \gg 1$. This is facilitated by the fact that application of the second-order derivative within the screen is straightforward within the integrals. The result is,

$$\begin{aligned}\langle\delta\theta^2\rangle &= \int dz_1 dz_2\left[\frac{2}{L_\perp^2}C\left(\mathbf{r}=0,z_1-z_2\right)D\left(\mathbf{r}=0,z_1-z_2\right)\right.\\ &\left.+\frac{1}{L_\perp^2}X_0^2 D\left(\mathbf{r}=0,z_1-z_2\right)\right]\\ &= \sqrt{2\pi}\frac{L_\parallel}{L_\perp}\sigma_Y^2\left(\sqrt{2}\sigma_X^2+X_0^2\right).\end{aligned} \tag{B.32}$$

These two characterizations of the degree of birefringence are related by

$$\langle\delta\phi^2\rangle = 4\pi^2\frac{L_\perp^2}{\lambda^2}\langle\delta\theta^2\rangle\left(\frac{\sqrt{2}\sigma_X^2+X_0^2}{2\sigma_X^2+\sqrt{2}X_0^2}\right). \tag{B.33}$$

where the terms in parentheses are generally of order unity. This relationship between $\langle\delta\phi^2\rangle$ and $\langle\delta\theta^2\rangle$ matches the general expectation from Equation B.24.

Broken Power-law Auto-correlation Functions

The second case we considered is when the auto-correlation functions take the form of a broken power law, which incorporates fluctuations on multiple scales. Above a minimum scale, $L_\perp$, the distribution of density and magnetic field fluctuations is self similar, characterized by a power-law index α,

$$C\left(\mathbf{r},z\right) = \frac{\sigma_X^2}{1+\left[(z^2+r^2)^{1/2}/L_\perp\right]^\alpha} \tag{B.34}$$

$$D\left(\mathbf{r}, z\right) = \frac{\sigma_Y^2}{1 + \left[\left(z^2 + r^2\right)^{1/2} / L_\perp\right]^\alpha}. \tag{B.35}$$

As a concrete example, we present the computation for $\alpha = 2$ prior to moving on to a Kolmogorov description; the result is qualitatively similar for any $\alpha > 1$. The variance in the phase perturbations are,

$$\begin{aligned}\langle \delta\phi^2 \rangle = 2\left(\frac{\omega}{c}\right)^2 \Bigg\{ & \sigma_X^2 \sigma_Y^2 \frac{1}{2} L_\parallel L_\perp \arctan\left(\frac{L_\parallel}{L_\perp}\right) \\ & + X_0^2 \sigma_Y^2 \left[\frac{1}{2} L_\perp^2 \ln\left(\frac{L_\perp^2}{L_\perp^2 + L_\parallel^2}\right)\right. \\ & \left. + L_\parallel L_\perp \arctan\left(\frac{L_\parallel}{L_\perp}\right)\right]\Bigg\}.\end{aligned} \tag{B.36}$$

Again we will assume $L_\parallel / L_\perp \gg 1$, and thus $\arctan L_\parallel / L_\perp \approx \pi/2$ and the logarithmic term is small relative to the linear terms. In this limit, the phase fluctuation variance simplifies to

$$\langle \delta\phi^2 \rangle = \left(\frac{\omega}{c}\right)^2 \frac{\pi}{2} L_\parallel L_\perp \sigma_Y^2 \left(\sigma_X^2 + 2X_0^2\right), \tag{B.37}$$

which, up to factors of order unity, matches the expression found for Gaussian auto-correlation functions.

The same argument holds true also for Equation B.19. After taking the second of derivative with r and evaluating at $r = 0$, integrating of Equation B.19 gives,

$$\langle \delta\theta^2 \rangle = \pi \frac{L_\parallel}{L_\perp} \sigma_Y^2 \left(\frac{3}{2}\sigma_X^2 + X_0^2\right). \tag{B.38}$$

This differs only by factors of order unity from the Gaussian-correlation-function case, with

$$\langle \delta\phi^2 \rangle = 4\pi^2 \frac{L_\perp^2}{\lambda^2} \langle \delta\theta^2 \rangle \left(\frac{\sigma_X^2 + 2X_0^2}{3\sigma_X^2 + 2X_0^2}\right). \tag{B.39}$$

Again, this expression matches the expectation from Equation B.24 up to factors that are generally of order unity.

This is a little different compared with that in the Gaussian case (Equation B.33), but as long as σ_X^2, σ_Y^2 and X_0^2 are of order one, Equation B.39 also holds true for the broken power law case.

Kolmogorov Turbulence-implied Auto-correlation Functions

The autocorrelation function and the structure function describing the same field are closely correlated. A more physically inspired autocorrelation function needs to be derived from a physical model of the turbulence. Past literature has suggested the power spectrum of the electron density fluctuation (e.g. see Armstrong et al. (1995); Rickett (1990)) as

$$P(q) \approx C_N^2 q^{-\beta}, \tag{B.40}$$

when the scale is between the inner and outer scale, where the factor C_N^2 is the structural coefficient, and β is the spectral power index, which in the Kolmogorov case, $\beta = 11/3$.

The corresponding structure function, D_ϕ, which is the integral form of the power spectrum, is related to Equation 3.27

$$D_\phi(\mathbf{x}) = \begin{cases} \left(\dfrac{|\mathbf{x}|}{x_0}\right)^2 & |\mathbf{x}| \ll r_{\text{in}} \\ \dfrac{2}{\alpha}\left(\dfrac{r_{\text{in}}}{x_0}\right)^{2-\alpha}\left(\dfrac{|\mathbf{x}|}{x_0}\right)^{\alpha} & |\mathbf{x}| \gg r_{\text{in}} \end{cases} \tag{B.41}$$

where x_0 is the normalization scale and $\alpha = \beta - 2$ for the Kolmogorov turbulence.

Meanwhile, the autocorrelation function for any field $\phi(x)$ is

$$D_\phi(x) = 2\left(\langle \phi(x)^2 \rangle - C(x)\right). \tag{B.42}$$

Given the variance of the field $\phi(x)$, σ_ϕ^2, and the average value of the field, we can write down $\langle \phi(x)^2 \rangle$:

$$\langle \phi(x)^2 \rangle = \sigma_\phi^2 + \langle \phi(x) \rangle^2. \tag{B.43}$$

For the fluctuating fields of electron density and magnetic strength, the electron density field $X(\mathbf{x})$ has the mean value X_0 and variance σ_X^2, and the magnetic field $Y(\mathbf{x})$ has zero mean value and variance σ_Y^2. Therefore, when $|\mathbf{x}| \gg \mathbf{r}_{\text{in}}$, the autocorrelation functions of the electron density and magnetic strength with Kolmogorov signature are

$$C(\mathbf{x}) = \sigma_X^2 + X_0^2 - \frac{1}{2}\left(\frac{|\mathbf{x}|}{x_0}\right)^{\alpha} \tag{B.44}$$

$$D(\mathbf{x}) = \sigma_Y^2 - \frac{1}{2}\left(\frac{|\mathbf{x}|}{x_0}\right)^{\alpha}, \tag{B.45}$$

In Section B.1.3, we showed that $\langle \delta\phi^2 \rangle$ and $\langle \delta\theta^2 \rangle$ are linearly related by a factor of $L_\perp^2$, which we physically interpreted $L_\perp$ as the typical size of the electron bubble that the scattering screen is comprised of, if the autocorrelation functions describing the electron density and the magnetic field satisfy the form of a broken power-law. The special case we demonstrated where the power index of the broken power-law being -2, if expanded, falls in the regime where $|\mathbf{x}| \ll \mathbf{r}_{\text{in}}$.

Similarly, for Equation B.44 and Equation B.45, they are the first order expansion of Equation B.34 and Equation B.35 in the regime where $|\mathbf{x}| \gg \mathbf{r}_{\text{in}}$:

$$C(\mathbf{x}) = \frac{\sigma_X^2 + X_0^2}{1 + (|\mathbf{x}|/L_\perp)^\alpha}, \tag{B.46}$$

$$D(\mathbf{x}) = \frac{\sigma_Y^2}{1 + (|\mathbf{x}|/L_\perp)^\alpha}, \tag{B.47}$$

where $L_\perp = 2^{1/\alpha} x_0$ can be interpreted as the typical transverse size of the electron bubble.

Similarly, inserting Equation B.46 and Equation B.47 into Equation B.23 and Equation B.19 gives, respectively,

$$\begin{aligned}
\langle \delta\phi^2 \rangle = \frac{12}{5} \left(\frac{\omega}{c}\right)^2 \left(\sigma_X^2 + X_0^2\right) \sigma_Y^2 \Bigg[& \frac{\left(\frac{L_\perp}{L_\parallel}\right)^{5/3} + 1}{\left(\frac{L_\parallel}{L_\perp}\right)^{5/3} + 1} \\
& + \frac{L_\perp}{L_\parallel} \ln\left(1 + \left(\frac{L_\parallel}{L_\perp}\right)^{1/3}\right)\left(2 - \frac{L_\perp}{L_\parallel}\right) \Bigg] \\
& + 12 \left(\frac{\omega}{c}\right)^2 X_0^2 \sigma_Y^2 \Bigg[L_\parallel L_\perp \ln\left(1 + \left(\frac{L_\parallel}{L_\perp}\right)^{1/3}\right) \\
& - L_\perp^2 \left[\left(\frac{L_\parallel}{L_\perp}\right)^{1/3} + \ln\left(1 + \left(\frac{L_\parallel}{L_\perp}\right)^{1/3}\right) \right] \Bigg],
\end{aligned} \tag{B.48}$$

$$\langle \delta\theta^2 \rangle = -4\left(\sigma_X^2 + X_0^2\right)\sigma_Y^2 \Bigg[1 - \left(\frac{1}{\left(\frac{L_\parallel}{L_\perp}\right)^{5/3} + 1} \right)^2 + \frac{24}{5}\frac{L_\parallel}{L_\perp} \ln\left(1 + \left(\frac{L_\parallel}{L_\perp}\right)^{1/3} \right) - \frac{1}{5}\left(\frac{L_\parallel}{L_\perp}\right)^{5/3} L_\perp \times \frac{8L_\parallel \left(\frac{L_\parallel}{L_\perp}\right)^{2/3} + 13L_\perp}{L_\parallel \left(\frac{L_\parallel}{L_\perp}\right)^{2/3} + L_\perp} \Bigg] - 4X_0^2\sigma_Y^2 \Bigg[1 - \frac{1}{\left(\frac{L_\parallel}{L_\perp}\right)^{5/3} + 1} - \frac{\left(\frac{L_\parallel}{L_\perp}\right)^{2/3}}{\left(\frac{L_\parallel}{L_\perp}\right)^{2/3} + \left(\frac{L_\perp}{L_\parallel}\right)} + 3\frac{L_\parallel}{L_\perp} \ln\left(1 + \left(\frac{L_\parallel}{L_\perp}\right)^{1/3} \right) \Bigg] \tag{B.49}$$

Taking leading order in $L_\parallel$ gives

$$\langle \delta\phi^2 \rangle \approx \frac{4}{5}\left(\frac{\omega}{c}\right)^2 L_\parallel L_\perp \ln\left(\frac{L_\parallel}{L_\perp}\right)\left(2\sigma_X^2 + 7X_0^2\right)\sigma_Y^2. \tag{B.50}$$

$$\langle \delta\theta^2 \rangle \approx \frac{4}{5}\frac{L_\parallel}{L_\perp} \ln\left(\frac{L_\parallel}{L_\perp}\right)\left(8\sigma_X^2 + 13X_0^2\right)\sigma_Y^2. \tag{B.51}$$

The functional forms of $\langle \delta\theta^2 \rangle$ and $\langle \delta\phi^2 \rangle$ satisfy the same linear relation as before:

$$\langle \delta\phi^2 \rangle = 4\pi^2 \frac{L_\perp^2}{\lambda^2} \langle \delta\theta^2 \rangle \left(\frac{8\sigma_X^2 + 13X_0^2}{2\sigma_X^2 + 7X_0^2} \right). \tag{B.52}$$

B.2 General Inversion of Refractive Scattering

Equation 3.26 describes a linear relationship between the power spectra associated with the brightness fluctuations before and after scattering. However, it is written in such a fashion that the observed power spectrum is a function of the properties of the scattering screen and the intrinsic power spectrum. What is desired is an expression for $P_{\rm int}^S(\mathbf{b})$ in

terms of the scattering screen and $P^S_{\rm obs}(\mathbf{b})$, i.e., to invert Equation 3.26. This is generally possible since $|K(\mathbf{u})| > 0$ and $D_\phi(\mathbf{u}) < \infty$ for all $\mathbf{u}$. In practice, it requires some care since despite being a linear relationship, it is non-local due to the presence of the convolution.

Here we develop a general inversion scheme, first using a local representation of the relationship between modified correlation functions, and second making use of a perturbative expansion that exploits the limit in which the refractive scattering kernel, $\mathbf{K}(\mathbf{u})$, is small. Equation 3.38 makes use of the first order approximation in this perturbative solution.

B.2.1 Alternate Convolution Representation

To further understand the role which $\mathbf{K}(\mathbf{u})$ plays in the process of scattering, it is straightforward to express Equation 3.26 in the convolution representation. In the convolution picture, we are able to acquire the solutions to the observed power spectrum $P^S_{\rm obs}(\mathbf{b})$ as required. And we can further assess the impact of the scattering kernel function $\mathbf{K}(\mathbf{u})$ on different baselines.

In the convolution representation, We define the spatial correlation functions

$$C^S_{\rm obs}(\mathbf{x}) = \int d^2\mathbf{b}\, e^{-i\mathbf{b}\cdot\mathbf{x}/r_F^2} P^S_{\rm obs}(\mathbf{b}), \tag{B.53}$$

and

$$D^S_{\rm int}(\mathbf{x}) = \int d^2\mathbf{b}\, e^{-i\mathbf{b}\cdot\mathbf{x}/r_F^2} e^{-D_\phi[\mathbf{b}/(1+M)]} P^S_{\rm int}(\mathbf{b}). \tag{B.54}$$

These are associated with the observed and diffractively suppressed spatial power spectra. In terms of these, Equation 3.26 may be written as

$$\begin{aligned} C^S_{\rm obs}(\mathbf{x}) &= D^S_{\rm int}(\mathbf{x}) - \frac{r_F^4}{4\pi^2(1+M)^6} \frac{\partial^2 D_\phi}{\partial\mathbf{x}\partial\mathbf{x}} : \frac{\partial^2 D^S_{\rm int}}{\partial\mathbf{x}\partial\mathbf{x}} \\ &= \left(1 - \mathbf{H} : \frac{\partial^2}{\partial\mathbf{x}\partial\mathbf{x}}\right) D^S_{\rm int}(\mathbf{x}), \end{aligned} \tag{B.55}$$

where

$$\mathbf{H} \equiv \int d^2\mathbf{u} e^{-i\mathbf{u}\cdot\mathbf{x}/r_F^2} \mathbf{K}(\mathbf{u}) = \frac{r_F^4}{4\pi^2(1+M)^6} \frac{\partial^2 D_\phi}{\partial\mathbf{x}\partial\mathbf{x}}, \tag{B.56}$$

defines a set of general coefficients across all Stokes parameters.

B.2.2 General Solution

Because $\mathbf{H}$ is manifestly Hermitian, Equation B.55 can be inverted by solving for the eigenfunctions of $(1 - \mathbf{H} : \nabla\nabla)$, which are guaranteed to be orthogonal. That is, solve for

$$\left(1 - \mathbf{H} : \frac{\partial^2}{\partial \mathbf{x} \partial \mathbf{x}}\right) f_j = \lambda_j f_j \tag{B.57}$$

from which we may obtain

$$D^S_{\rm int}(\mathbf{x}) = \sum_j \lambda_j^{-1} f_j(\mathbf{x}) \int d^2\mathbf{y}\, f_j(\mathbf{y}) C^S_{\rm obs}(\mathbf{y}). \tag{B.58}$$

From this we may obtain the desired spatial power spectrum via

$$\begin{aligned} P^S_{\rm int}(\mathbf{b}) &= e^{D_\phi[\mathbf{b}/(1+M)]} \int d^2\mathbf{x}\, e^{2\pi i \mathbf{b}\cdot\mathbf{x}} D^S_{\rm int}(\mathbf{x}) \\ &= e^{D_\phi[\mathbf{b}/(1+M)]} \sum_j \lambda_j^{-1} \tilde{f}_j(\mathbf{b}) \int d^2\mathbf{y}\, f_j(\mathbf{y}) C^S_{\rm obs}(\mathbf{y}) \\ &= e^{D_\phi[\mathbf{b}/(1+M)]} \sum_j \lambda_j^{-1} \tilde{f}_j(\mathbf{b}) \int d^2\mathbf{u}\, \tilde{f}_j(-\mathbf{u}) P^S_{\rm obs}(\mathbf{u}), \end{aligned} \tag{B.59}$$

where $\tilde{f}_j(\mathbf{u})$ is the Fourier transform of the eigenfunctions. Thus, it is not necessary to generate the correlation functions at any point.

The success of this approach depends on number of eigenmodes that must be included to approximate $D^S_{\rm int}(\mathbf{x})$ with sufficient fidelity.

B.2.3 Perturbative Solution

Since the dependence on the eigenmodes, it may present difficulties finding general solutions without modelling the details of the scattering screen. Therefore, more practically, a perturbative solution is preferred here.

If $\mathbf{H}$ is small, we may adopt a perturbative approach to inverting Equation B.55. In this approximate we expand

$$D^S_{\rm int}(\mathbf{x}) = D^S_{{\rm int},0}(\mathbf{x}) + \epsilon D^S_{{\rm int},1}(\mathbf{x}) + \epsilon^2 D^S_{{\rm int},2}(\mathbf{x}) + \ldots \tag{B.60}$$

where ϵ is an order-counting parameter that keeps track of how many factors of $\mathbf{H}$ are included. Then, we solve Equation B.55 at each order in ϵ assuming that $\mathbf{H}$ is first order:

$$\begin{aligned} D^S_{\text{int},0}(\mathbf{x}) &= C^S_{\text{obs}}(\mathbf{x}) \\ D^S_{\text{int},1}(\mathbf{x}) &= \mathbf{H} : \frac{\partial^2 D^S_{\text{int},0}(\mathbf{x})}{\partial \mathbf{x} \partial \mathbf{x}} = \mathbf{H} : \frac{\partial^2 C^S_{\text{obs}}(\mathbf{x})}{\partial \mathbf{x} \partial \mathbf{x}} \\ D^S_{\text{int},2}(\mathbf{x}) &= \mathbf{H} : \frac{\partial^2 D^S_{\text{int},1}(\mathbf{x})}{\partial \mathbf{x} \partial \mathbf{x}} \\ &= \mathbf{H} : \frac{\partial^2}{\partial \mathbf{x} \partial \mathbf{x}} \mathbf{H} : \frac{\partial^2}{\partial \mathbf{x} \partial \mathbf{x}} C^S_{\text{obs}}(\mathbf{x}) \\ &\vdots \end{aligned} \tag{B.61}$$

Each of these may be recast in terms of integrals over $P^S_{\text{obs}}(\mathbf{u})$ immediately, and upon resuming we find

$$\begin{aligned} P^S_{\text{int}}(\mathbf{b}) = & e^{D_\phi[\mathbf{b}/(1+M)]} \Bigg\{ P^S_{\text{obs}}(\mathbf{b}) \\ & - \int d^2\mathbf{y}\, \mathbf{K}(\mathbf{y}+\mathbf{b}) : \left[\mathbf{y} P^S_{\text{obs}}(\mathbf{y}) \mathbf{y}^T\right] \\ & + \iint d^2\mathbf{y} d^2\mathbf{z}\, \mathbf{K}(\mathbf{y}+\mathbf{b}) \\ & : \left[\mathbf{y}\mathbf{K}(\mathbf{z}+\mathbf{y}) : \left(\mathbf{z} P^S_{\text{obs}}(\mathbf{z}) \mathbf{z}^T\right) \mathbf{y}^T\right] \\ & + \dots \Bigg\}. \end{aligned} \tag{B.62}$$

Note that this may be evaluated recursively, with

$$\begin{aligned} g_0(\mathbf{b}) &= P^S_{\text{obs}}(\mathbf{b}) \\ g_1(\mathbf{b}) &= g_0(\mathbf{b}) - \int d^2\mathbf{y}\, \mathbf{K}(\mathbf{y}+\mathbf{b}) : \left[\mathbf{y} g_0(\mathbf{y}) \mathbf{y}^T\right] \\ g_2(\mathbf{b}) &= g_1(\mathbf{b}) - \int d^2\mathbf{y}\, \mathbf{K}(\mathbf{y}+\mathbf{b}) : \left[\mathbf{y} g_1(\mathbf{y}) \mathbf{y}^T\right] \end{aligned} \tag{B.63}$$

in terms of which $P^S_{\text{int}}(\mathbf{b}) = e^{D_\phi[\mathbf{b}/(1+M)]} g_\infty(\mathbf{b})$.

The number of orders that must be kept depend on the size of $\mathbf{H}$, or equivalently $\mathbf{K}$, relative to the identity term. This method has the distinct advantage of being immediately computation-ready once $Q(\mathbf{u})$ is specified, without the need to solve the eigenmode problem.